Università degli Studi di Napoli "Federico II"
Dipartimento di Ingegneria Chimica

Molecular Models for Entangled Polymer Rheology

Herwin Jerome Unidad

PhD in Chemical Engineering (XXV cycle)
(2010-2013)

March 2013

Abstract

Molecular models for capturing the behavior of various entangled polymer systems were developed based on the physical framework of the tube model by Doi and Edwards and stochastic slip-link simulations built on similar ingredients. Using such models, we confronted three problems involving entangled polymers in this work.

First, we investigated the effects of entanglements on the elastic behavior of polymer networks using slip-link simulations. In particular, we simulated randomly-crosslinked networks using the Primitive Chain Network model of Masubuchi and co-workers. We observed that the obtained stress-strain behavior for these networks from simulations compared reasonably with the replica theory of Edwards and Vilgis, which is consistent with experiments. This contrasts with previous findings in end-linked networks where application of the model was less successful. We explored possible mechanisms to eliminate the discrepancies on predictions for the latter. However, none of these mechanisms seem physically reasonable in the context of the present model. We also confronted the issue of thermodynamic inconsistency of the model by considering an alternative sliding equation based on the chemical potential. This new sliding equation gave a slightly different stress-strain response for randomly-crosslinked networks but the difference was minimal in contrast with the huge discrepancy observed in end-linked systems.

Second, we modeled data on parallel superposition flows of monodisperse and nearly monodisperse solutions from the experiments of Wang and co-workers using a simple tube-based constitutive equation with convective constraint release (CCR). By doing a linear expansion on this equation, we obtained analytic expressions for superposition spectra as a function of shear rate and the CCR parameter β. We then compared predictions based on these expressions with the experimental data. Model agreement was quite satisfactory and was independent of the choice of β. Predictions on the shifting of the crossover frequency of these spectra as a function of the shear rate were also consistent with the empirical trend reported by Wang and

co-workers which they rationalized using the concept of CCR. However, as our predictions did not vary with the inclusion or non-inclusion of CCR in the model, we claim that the observed shifting by Wang and co-workers is due simply to orientation and flow and not CCR.

Finally, we modified simple tube-based constitutive equations to account for flow-induced monomer friction reduction (MFR). We then used these constitutive equations to model data on the elongational rheology of monodisperse polystyrene melts and solutions from filament stretching rheometry. MFR has been proposed previously as a mechanism which could explain the qualitatively different behavior of melts and solutions revealed by recent experiments. These systems are expected to behave similarly from the perspective of classical tube models with chain stretch. We show that inclusion of MFR in combination with CCR and chain stretch in simple tube models allows for a semi-quantitative fitting of the available data sets on both polystyrene melts and solutions. We also applied the modified equations in the analysis of shear flows and stress relaxation after cessation of flow of PS melts to further understand the MFR mechanism. We find that the MFR effect is triggered only when the stretching of the system is sufficient to align the Kuhn segments. Further tests of this model by applying it to bidisperse polystyrene melts would give further credence to this approach.

Acknowledgements

This work would not have been possible without the help and assistance of many people.

First and foremost, my supervisor Giovanni Ianniruberto, for giving me the chance to work on these topics and enter the world of molecular rheology and entangled polymers. Thank you for the ample supervision, the assistance in all things scientific and bureaucratic and for helping me understand what "physics" truly meant in modeling.

Prof. Giuseppe Marrucci, for the scientific direction and the ideas, especially at the initial part of the work.

Prof. Pier Luca Maffettone, for being part of my scientific committee.

Dr. Daniel Read, for being the external reviewer of this thesis, for thoroughly reading this work and for the helpful comments.

Prof. Yuichi Masubuchi, for the assistance in my initial attempts to develop a version of the NAPLES code, for help with the simulations on randomly-crosslinked networks and for hosting me during my research visit in Kyoto.

Prof. Hiroshi Watanabe, Yumi Matsumiya, Tadashi Uneyama and the students in their group for their hospitality during my research stay in Japan.

Dr. Sathish Sukumaran and Prof. Jun-Ichi Takimoto, for the assistance and financial support during my short stay at Yonezawa and for valued discussions on my work on entangled networks.

Dr. Xin Li, Dr. Pouyan Boukany and Dr. Frank Snijkers for sharing some of their data which are used in this work.

My colleagues and professors from DYNACOP, for helping broaden and improve my understanding of entangled polymer dynamics and for useful discussions which have greatly benefitted my work. In particular, many thanks to Laurence Hawke, Maxim Shivokhin and Qian Huang for incredibly useful and stimulating discussions.

My colleagues here in Naples, for help, especially during the initial period of my stay here. Thanks to Fabio Nicodemi and Ilaria di Rienzo for the

lunches, the company and the friendship. Thanks to Naveed Ahmad for the coffee breaks and discussions. Thanks as well to colleagues Gaetano d'Avino and Rossana Pasquino for help when I was still starting life in Naples.

Some of my friends, for taking time to read parts of this manuscript and proofreading this work. In particular, comments from Johanna Mae Indias, Cheska Siongco and David So have been useful. I also thank Nathaniel Hermosa for some helpful discussions on the importance of framing in research writing.

Teddy and Gina Perez, for giving me a second family and home in Rome during my stay here in Italy.

My parents, Rommel and Helen Unidad, and my family for letting me go and take a leap on this defining opportunity to live and study in Europe. I thank my sister, Hannah Jessica, for serving as inspiration to aspire for more and to be better at what I am doing.

Finally, this work would not have been possible without the financial support from the European Union through the Marie Curie Initial Training Network DYNACOP (grant no. 214627).

Herwin Jerome Unidad
Naples, Italy
February 2013

Contents

List of Figures

List of Tables

Chapter 1

Introduction

1.1 General Introduction and Objectives

The success and advantages of a *molecular approach* is exemplified by the problem of entangled polymer rheology, one of the most important benchmark problems for both rheology and soft matter physics. While interesting from a scientific perspective, the problem is simultaneously of industrial significance – the rheological behavior of polymers is an important consideration in processing such as extrusion, blow molding and fiber spinning where molten polymers are subjected to large deformations at fast rates.

The supposed origin of the rich mechanical and rheological behavior exhibited by polymers are the *entanglements* which arise when chains are long enough to overlap. Here, *topological interactions* between the chains due to their uncrossability start to become relevant in their dynamics. The most successful approach to this many-body problem is the so-called *tube model* by Doi and Edwards [1]. This framework makes use of the concept of the *tube* proposed by Edwards [2], the notion of *reptation* or snake-like motion of the chain coined by de Gennes [3] and was developed in a constitutive framework in a series of papers by Doi and Edwards [4, 5, 6, 7]. The basic Doi-Edwards theory has been refined and improved upon by Marrucci, McLeish and others for fast flows and nonlinear chain architectures [8, 9] resulting in what is generally accepted as the *standard model* for entangled polymer dynamics.

The resulting *standard model* has been shown to be quite successful in a wide variety of situations although it is still being continually challenged by new experimental data, as in the cases considered in this work. These data must necessarily come from experiments on model polymer systems with low polydispersity, such as those made by anionic polymerization un-

der high vacuum [10]. The behavior of such materials with well-defined structure can then be compared to models which predict ideal behavior. Likewise, new experimental methods are being continually improved. For example, new methods for generating extensional flows [11, 12] have been developed allowing data generation for a wider range of rates and deformations. This is also being supplemented by other techniques that can be used to probe microscopic chain dynamics such as dielectric spectroscopy [13, 14] and neutron scattering techniques [15].

Further, computer simulations are emerging as important tools in understanding these systems. At the present, well-developed techniques on doing molecular dynamics (MD) simulations of polymer systems like the Kremer-Grest bead-spring model [16], coupled with new modes of analysis using the concepts of *primitive path* [17] or *mean path* [18], can provide further insights on these entangled systems [19]. In addition, more coarse-grained stochastic or mesoscopic simulations capable of resolving long-time behavior are being developed such as the Twentanglement method [20] or slip-link simulations [21, 22, 23, 24, 25, 26, 27]. Indeed, the latter family of models have been emerging as more detailed alternatives to tube models [28].

This interplay of the experimental fields of polymer synthesis, rheometry and other probes of tube motion with advances in theory, modeling and computer simulations has enabled significant advances in the field of both fundamental and applied nature. Indeed, some work has been done in developing models that enable the *molecular engineering* of these complex materials for industrial application [29] or in simulating actual industrial processes down to the molecular scale [30]. That being said, some challenges persist in the field in various directions – some pertaining to challenges on establishing a more fundamental basis for the tube model [31] while others pertain to new unobserved phenomena that cannot be explained in terms of the pre-established framework [32, 33, 34]. Further, some findings are even at odds with the current framework [35, 36, 37] prompting some to re-consider the entire tube perspective altogether [38].

This work attempts to shed light on some of the remaining open problems in the field particularly those concerning large deformation or nonlinear flows and within the framework of either tube-based constitutive equations or slip-link simulations. The latter will be used to confront problems on entangled networks while the former will be applied to entangled liquids (melts and concentrated solutions) of polymers with linear architectures. The physics of branched polymers while both interesting and challenging remains beyond the scope of this work. In at least one occasion, it will be shown that the physics in the *standard model* is insufficient to model the data requiring the

need for further examination of the system and the introduction of some new physics.

1.2 Outline

This thesis is organized as follows:

The remainder of this chapter is devoted to a brief review of the current understanding of entangled polymer rheology. The aim is not to provide a thorough explanation of the subject as this can be found elsewhere [1, 39, 40] but, rather, to provide some grounding on the present work.

Chapter 2 is on the development of slip-link simulations of entangled rubbers. The model explored here is the *primtive chain network model* developed by Masubuchi and co-workers [22] for entangled polymers and applied to a variety of systems. The work here builds on previous efforts to apply the model to entangled rubbers [41, 42] and aims in resolving the observed discrepancy between model predictions and an established constitutive model. In this work, the problem is explored further by considering other rubber systems to obtain more insights on why the previous discrepancy exists. This work was done in collaboration with Prof. Yuichi Masubuchi (Kyoto University) during a research visit in Japan and has been presented in the following conferences and meetings:

- HJ Unidad, G Iannirubertо, Y Masubuchi. Primitive Chain Network Simulations of Entangled Rubbers. *XVIth International Congress on Rheology*. Lisbon, Portugal. August 2012
- HJ Unidad, G Iannirubertо, G Marrucci. Slip-link Simulations of Entangled Polymers: Progress and Challenges. *CECAM-DYNACOP Workshop on Entangled Polymers: Dynamics and Architectures*. Anacapri, Italy. July 2011
- HJ Unidad, G Iannirubertо, G Marrucci. Slip-link Simulations of Entangled Polymers. *5th European Polymer Federation Summer School*. Gargnano, Italy. May 2011 [Poster]

Chapter 3 is on the analysis of parallel mechanical superposition experiments on entangled melts and solutions using tube theory. The work here builds on the superposition experiments done by Wang and co-workers [43, 44] on monodisperse (or nearly monodisperse) polymer solutions. The objective is to confront the data from these experiments using tube-based

constitutive equations to see if the data agrees with these models and is quantitatively consistent with the idea of *convective constraint release*(CCR) [45, 46]. This work is the subject of the following manuscript

- HJ Unidad, G Ianniruberto. The role of convective constraint release in parallel superposition flows of entangled polymer solutions. [submitted]

Chapter 4 is on the development of constitutive models for the nonlinear rheology of entangled melts and solutions. Central to this section is the idea of monomeric friction reduction in flow proposed recently [47] to explain the observed difference in the elongational behavior of entangled melts and solutions [32, 33] – systems which according to classical theory should behave similarly. Here, this idea is developed further by including it in simple tube-based constitutive equations. These can then be compared with the available experimental data on entangled polymer solutions and melts (start-up and steady-state elongational flow, stress relaxation after cessation of elongational flow and nonlinear shear flow) to see if the findings are consistent with this proposed theory. The work has been presented in the following conference

- HJ Unidad, G Ianniruberto. Analysis of Uniaxial Elongational Flows of Entangled Linear PS Melts. *DYNACOP Final Conference*. Leeds, United Kingdom. December 2012

and is the subject of the following manuscript

- HJ Unidad, G Ianniruberto. Simple constitutive equations for entangled polymers with flow-induced monomeric friction reduction. [in preparation]

Finally, some concluding remarks and future outlook on the work are given in Chapter 5.

1.3 Entangled Polymer Rheology

This section provides a general overview of the basic concepts and principles in the molecular rheology of entangled polymers. Readers who have familiarity on the material are invited to skip this section.

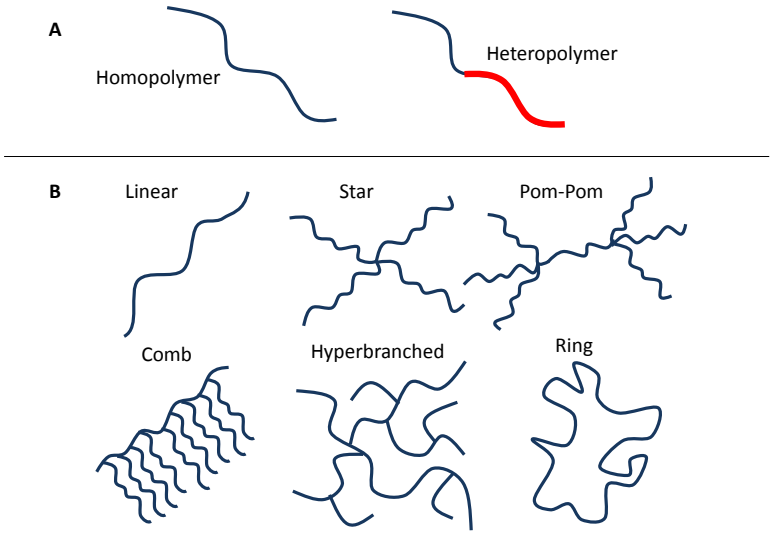

Figure 1.1: Different chain architectures according to (a) chemistry and (b) topology

1.3.1 General Description of Polymers

Polymers are large molecules that consist of many repeating units that are covalently linked. The repeating units could be of different chemical composition, resulting in a *heteropolymer* or of the same chemical composition, giving rise to a *homopolymer*. Likewise, the chain architecture or topology could be simply linear or branched, which can be further categorized depending on the number and arrangement of branching points (as shown in fig.1.1). The architecture can even be cyclic, the so-called *ring polymers* which have interesting dynamics as they have no free ends [48, 49]. While the presence of different monomer chemistries and branching points give rise to interesting dynamics and rheology, the focus of this work will be linear homopolymers.

In rheological modeling, the goal is to develop constitutive equations that relate the stress within a material with its deformation history. For molecular rheology, the aim is to derive such relations from the underlying microscopic physics of the material, in this case, the polymer. To accomplish this, a physical description of polymer conformation/structure is necessary rather than an actual chemical description. In such a description of polymer conformation one can represent a polymer chain by a series of i beads

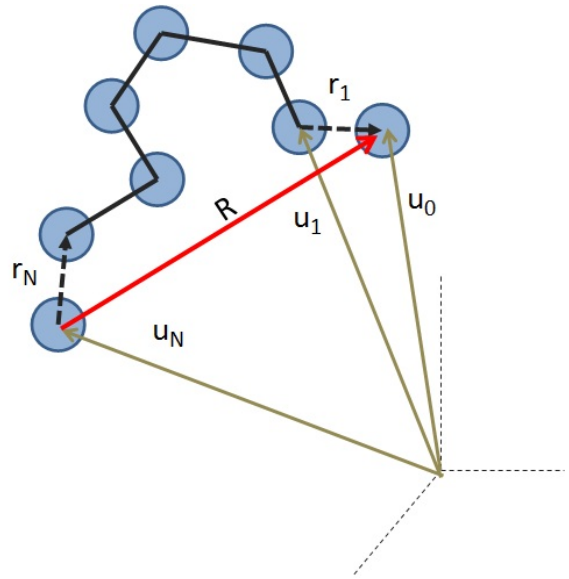

Figure 1.2: Physical representation of polymer chains: beads and bonds

separated by $i-1$ bonds with positions denoted by the vectors $\mathbf{u}_i$ as shown in fig. 1.2. This can be justified by the fact that rheology deals more with large-scale and long-time chain behavior. Hence, microscopic details matter only as far as the basic units of length and time are concerned. Indeed, it is a similar philosophy that allows the approach of mapping real polymeric systems of various chemistries into generic bead-spring models such as the Kremer-Grest model [16] to run simulations.

An alternative representation would be to use the vectors corresponding to the bonds between each bead rather than each bead position. Each bond i can then be represented by the vector $\mathbf{r}_i = \mathbf{u}_i - \mathbf{u}_{i-1}$. To specify polymer conformation, one should then identify either of the following sets:

$$\{\mathbf{u}_i\} = (\mathbf{u}_0, \mathbf{u}_1, \mathbf{u}_2, \ldots, \mathbf{u}_N) \tag{1.1}$$

$$\{\mathbf{r}_i\} = (\mathbf{r}_1, \mathbf{r}_2, \ldots, \mathbf{r}_N) \tag{1.2}$$

where N here is the number of beads or the *degree of polymerization*, essentially a measurement of chain length.

An important vector to define is the end-to-end vector $\mathbf{R}$, which is the sum of all N bond vectors in a chain,

$$\mathbf{R} = \sum_{i=1}^{N} \mathbf{r}_i \tag{1.3}$$

and the mean squared end-to-end distance $\langle \mathbf{R}^2 \rangle$, a measure of the chain size.

$$\langle \mathbf{R}^2 \rangle = \left\langle \left(\sum_{i=1}^{N} \mathbf{r}_i \right) \left(\sum_{j=1}^{N} \mathbf{r}_j \right) \right\rangle = \sum_{i=1}^{N} \sum_{j=1}^{N} \langle \mathbf{r}_i \cdot \mathbf{r}_j \rangle \tag{1.4}$$

These quantities describing chain (and subchain) conformation can then be used in a microscopic definition of the stress.

1.3.2 Microscopic Definition of Stress

The macroscopic stress tensor $\boldsymbol{\sigma}$ is defined as follows

$$\mathbf{F}_T = A\mathbf{n} \cdot \boldsymbol{\sigma} \tag{1.5}$$

where $\mathbf{F}_T$ is the total force acting on the area A and $\mathbf{n}$ is the unit vector normal to the area.

In terms of the microscopic structure of the material, Doi and Edwards derive and report the Kirkwood expression for the stress [1]:

$$\boldsymbol{\sigma}_{\alpha\beta} = -\frac{1}{V} \sum_{j=1}^{N_s} \langle \mathbf{F}_{j,\alpha} \mathbf{u}_{j,\beta} \rangle \tag{1.6}$$

$\mathbf{F}_j$ here is the elastic force acting on each material element j located at position $\mathbf{u}_j$ and α and β are indices for the principal directions.

For polymers, where each element can be represented by an *elastic segment* or a spring with two beads exerting a force $\mathbf{F}_j$ on each other as in fig. 1.3, equation (1.6) becomes

$$\boldsymbol{\sigma}_{\alpha\beta} = -\frac{1}{V} \sum_{j=1}^{N_s} ((\mathbf{F}_{j,\alpha})\mathbf{u}_{j1,\beta} + (-\mathbf{F}_{j,\alpha})\mathbf{u}_{j2,\beta}) = \frac{1}{V} \sum_{j=1}^{N_s} (\mathbf{F}_{j,\alpha})\mathbf{r}_{j,\beta} \tag{1.7}$$

which was simplified by using the bond vector for the segment, $\mathbf{u}_{i2,\beta} - \mathbf{u}_{i1,\beta} = \mathbf{r}_{i,\beta}$.

If one defines the number of elastic segments per volume $\nu = N_s/V$ and the system is large, one can replace the sum in (1.7) by an ensemble average as shown below.

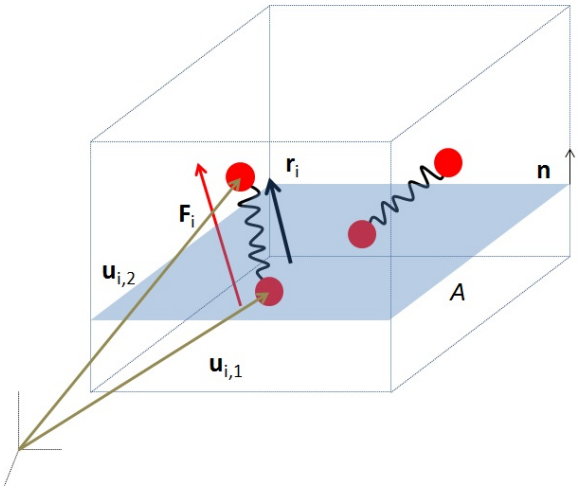

Figure 1.3: Microscopic definition of the stress

$$\boldsymbol{\sigma}_{\alpha\beta} = \nu\langle \mathbf{F}_\alpha \mathbf{r}_\beta \rangle \tag{1.8}$$

For Gaussian chains where the elastic force in a subchain is proportional to the subchain vector, i.e. $\mathbf{F} \sim \mathbf{r}$, the following proportionality holds

$$\boldsymbol{\sigma} \sim \langle \mathbf{rr} \rangle \tag{1.9}$$

where $\langle \mathbf{rr} \rangle$ is called the *conformation tensor*. It then follows that one can intepret the stress on a polymeric material as distortions of polymer conformation.

1.3.3 Deformation and Flow

Other than a representation of the stress within a material, one also requires a representation of the deformation experienced by the material for rheological models. For this, one can consider the strain tensor $\mathbf{E}$,

$$\mathbf{E}(t, t')_{\alpha\beta} = \frac{\partial \mathbf{u}'_\alpha}{\partial \mathbf{u}_\beta} \tag{1.10}$$

where the running indices α, β represent the principal directions 1 to 3. This tensor represents the displacement of a material element initally located at $\mathbf{u}$ at time t to $\mathbf{u}'$ at a later time t'. The inverse of this tensor, $\mathbf{E}^{-1}$ is called the *deformation gradient tensor*.

One can also consider the rate at which the deformation is applied by considering the *velocity gradient tensor*

$$\nabla \mathbf{v}_{\alpha\beta} = \frac{\partial \mathbf{v}_\alpha}{\partial \mathbf{u}_\beta} \tag{1.11}$$

whose transpose defined as $\boldsymbol{\kappa} = (\nabla \mathbf{v})^T$ is also used in literature.

$\boldsymbol{\kappa}$ is an important representation of the flow fields imposed on a material. For simple or *rheometric flows* such as those considered in this study, these representations are well-known. For shear flows where the *deformation plane* is the one spanned by the directions 1 and 2, $\boldsymbol{\kappa}$ is defined as

$$\boldsymbol{\kappa} = \begin{pmatrix} 0 & \dot{\gamma} & 0 \\ 0 & 0 & 0 \\ 0 & 0 & 0 \end{pmatrix} \tag{1.12}$$

where $\dot{\gamma}$ is the *shear rate*.

For uniaxial elongational flows with the elongation in the 1 direction, $\boldsymbol{\kappa}$ is

$$\boldsymbol{\kappa} = \begin{pmatrix} \dot{\epsilon} & 0 & 0 \\ 0 & -\dot{\epsilon}/2 & 0 \\ 0 & 0 & -\dot{\epsilon}/2 \end{pmatrix} \tag{1.13}$$

where $\dot{\epsilon}$ is the *elongation rate*. For other rheometric flows such as planar elongation, biaxial elongation or mixed flows (containing both shear and elongation), the reader is referred to the following [39, 50].

These tensors, as well as others such as the Finger tensor, etc. are often used in writing constitutive equations [39, 50] for viscoelastic materials such as polymers.

1.3.4 Viscoelasticity

Polymer materials exhibit complex response to either stress or strain in between those of classic solids or liquids, often referred to as *viscoelasticity*. Classic solids at low strains obey *Hooke's law* which in simple shear could be written as follows

$$\sigma = G\gamma \tag{1.14}$$

where γ is the applied shear strain on the material and σ is the resulting stress with the proportionality constant G being the *elastic modulus*.

On the other hand, classic liquids will obey *Newton's law*[1]

$$\sigma = \eta\dot{\gamma} \tag{1.15}$$

where $\dot{\gamma}$ is the applied shear rate and the proportionality constant η is called the *viscosity* of the material.

Note the fundamental difference between the two types of response. The solid response (also called the *elastic* response) is strain-dependent but rate-independent. It is also energy-conserving and allows full recovery of the energy applied through deformation upon release. In contrast, the liquid response (also called the *viscous* response) is rate-dependent but not strain-dependent. It is also fully dissipative and all energy transfered to the liquid through deformation will be fully dissipated. Since polymeric response would often be in between these extremes, it depends on both the magnitude of the applied strain and the rate at which it is applied.

Step-Strain Experiment

To emphasize the difference between classic solids and liquids as well as viscoelastic ones, one can do a simple *step-strain experiment* as shown in fig. 1.4.

The figure emphasizes the *time-dependence* of viscoelastic reponse. For small values of γ, i.e. in the regime of *linear viscoelasticity*, one can follow this time-dependent response by monitoring the elastic modulus $G(t)$ which is defined simply from (1.14) as $\sigma(t)/\gamma$ and whose plot has the same profile as 1.4. Classic solids have a finite value for the modulus while Newtonian liquids will have a 0 modulus.

For viscoelastic solids, the modulus starts at a certain level and then decays to reach an asymptotic value (which in fig. 1.4 is σ_E/γ). The same decay behavior is observed for viscoelastic liquids except the asymptotic value is 0, which corresponds to total energy dissipation (only partial viscous dissipation occurs for solids). As with most physical decay processes, this can be fit by an exponential function and characterized by a relaxation time τ written as follows.

$$G(t) = G_0 e^{-t/\tau} \tag{1.16}$$

[1]For this reason, classic liquids which obey Newton's law are called *Newtonian fluids* while fluids which exhibit behavior more complex than this, e.g. polymer liquids, are called *Non-Newtonian fluids*.

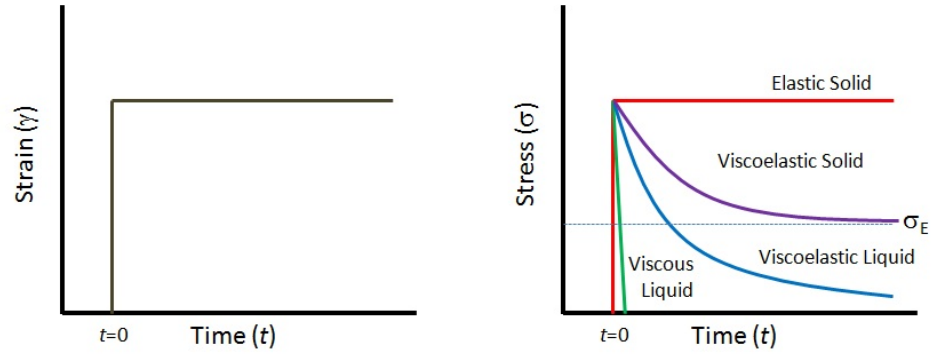

Figure 1.4: Stress response of different materials in a step-strain experiment

Note that (1.16) applies only to liquids and must be modified by an additive constant on the right-hand side (corresponding to the asymptotic value of G) to apply to solids.

Oscillatory Shear Experiment

One can also perform an *oscillatory shear experiment* (also known as a *frequency sweep* test) in lieu of stress relaxation. One does this by applying a time-dependent periodic strain $\gamma(t)$,

$$\gamma(t) = \gamma_0 \sin(\omega t + \delta) \tag{1.17}$$

where w is the frequency of the strain field. It follows that the strain rate is also periodic and is 90° out of phase of the strain and is thus as follows

$$\dot{\gamma}(t) = \gamma_0 \omega \cos(\omega t + \delta) \tag{1.18}$$

where δ is an arbitrary phase constant.

In general, assuming that the deformation starts at $\delta = 0$ for time $t = 0$, the material response which depends on the frequency ω can be represented by the modulus $G^*(\omega)$ defined as σ/γ. $G^*(\omega)$ can be expressed as a *Fourier series* of the powers of the two waveforms which span the entire material response.

$$G^*(\omega) = G_{\alpha,1} \sin(\omega t) + G_{\beta,1} \cos(\omega t) + G_{\alpha,2} \sin^2(\omega t) + G_{\beta,2} \cos^2(\omega t) + \cdots \tag{1.19}$$

where only the first and second-order terms are shown. If the amplitude γ_0 of the deformation is small, i.e. one remains in the *linear regime*, terms containing the 2nd and higher powers of A have minimal contribution and can be neglected. Equation (1.19) then only has two remaining terms.

$$G^*(\omega) = G'(\omega)\sin(\omega t) + G''(\omega)\cos(\omega t) \tag{1.20}$$

where the coefficients $G_{\alpha,1}$ and $G_{\beta,1}$ have been replaced by the more conventional symbols G' and G'', respectively. G', referred to as the *storage modulus*, shows the elastic or solid-like response of the material. On the other hand G'', called the *loss modulus*, shows the viscous or liquid-like response of the material.

The expression (1.20) deserves a few comments. First, the expansion clearly offers an alternative way of representing the entire linear viscoelastic response of a material. One can either specify the time-dependent modulus $G(t)$ or, equivalently, give the pair $G'(\omega)$ and $G''(\omega)$, the storage and loss moduli. One can switch between the two representations by performing a *Fourier transform* as follows.

$$G^*(\omega) = i\omega \int_0^\infty e^{-i\omega t} G(t) dt \tag{1.21}$$

where G^* is the *complex modulus* defined as $G^* = G' + iG''$.

It then follows from (1.21) that G' and G'' can be defined in terms of $G(t)$.

$$G'(\omega) = \omega \int_0^\infty \sin(\omega t) G(t) dt \tag{1.22}$$

$$G''(\omega) = \omega \int_0^\infty \cos(\omega t) G(t) dt \tag{1.23}$$

Second, G' and G'' are both frequency-dependent hence experiments to measure both must span a range of frequencies in order to probe the entire LVE response of the material. In general, higher frequencies probe the elastic response more, implying that $G' > G''$. Meanwhile, the viscous response is more dominant for lower frequencies hence $G'' > G'$. It also follows that both curves intersect at a certain critical frequency (ω_c) which corresponds to the *terminal relaxation time* τ_0 for the material - the timescale where the response switches from being elastic-dominated to viscous-dominated.

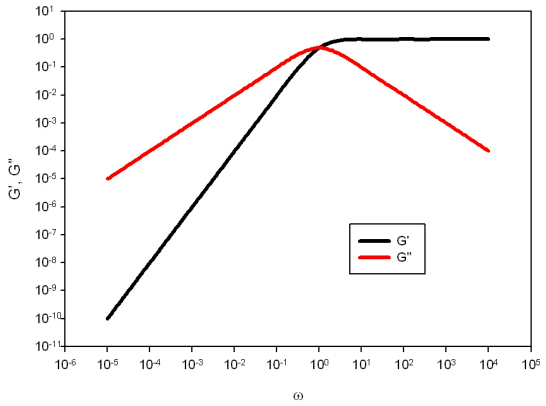

Figure 1.5: Plot of the expression for G' and G" for a Maxwell mode with $\tau = 1$ and $G_0 = 1$

General Linear Viscoelastic Model

For a viscoelastic fluid whose relaxation modulus can be fit exactly by the form (1.16), i.e. for materials with only one characteristic time τ, equations (1.22) and (1.23) provides expressions for G' and G''.

$$G'(\omega) = G_0 \frac{\omega^2\tau^2}{1+\omega^2\tau^2}, G''(\omega) = G_0 \frac{\omega\tau}{1+\omega^2\tau^2} \tag{1.24}$$

Both these equations, whose plots are shown in fig. 1.5 and equation (1.16) define the so-called *Maxwell model*. In fig. 1.5, the curve for G' shows a plateau at higher frequencies corresponding to G_0, here set to 1. On the other hand, G' has a peak about a frequency corresponding to $1/\tau$, here also set to 1. This peak is also where the *first crossover point* occurs, i.e. where the dominant term in the relaxation changes from elastic to viscous as one moves from higher frequencies to lower frequencies. The Maxwell model is applicable for materials with one characteristic time τ and one modulus G_0, represented by a spring (elastic component) and dashpot (viscous or dissipative component) system in series, shown in fig. 1.6.

However, polymers, even monodisperse ones, exhibit a variety of relaxation processes and correspondingly different relaxation times. A simple and generic model then that can be used to fit their linear viscoelastic response would be to consider an extended Maxwell model with a set of relaxation times and fractional moduli $\{\tau_k, g_k\}$, each operating in parallel,

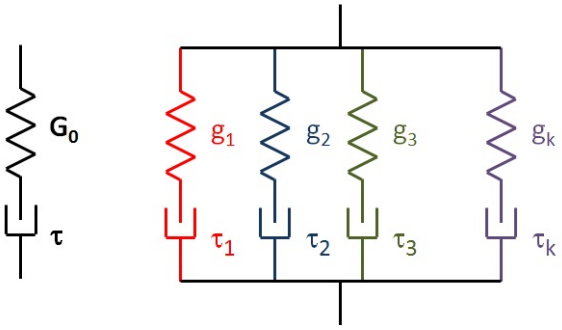

Figure 1.6: Schematic diagram of single and multiple Maxwell modes for describing linear viscoelasiticity

also shown schematically also in fig. 1.6. Each pair can be well-described by the Maxwell model and can be referred to as one *relaxation mode* or one Maxwell mode.

Hence, the relaxation modulus $G(t)$ can be defined as

$$G(t) = \sum_k g_k \exp\left(-\frac{t}{\tau_k}\right) \tag{1.25}$$

and the dynamic moduli $G'(\omega)$ and $G''(\omega)$ can be expressed as follows

$$G'(\omega) = \sum_k g_k \frac{\tau_k^2\omega^2}{1+\tau_k^2\omega^2}, G''(\omega) = \sum_k g_k \frac{\tau_k\omega}{1+\tau_k^2\omega^2} \tag{1.26}$$

An example of such a fitting is shown in fig. 1.7 for LVE data for a real polymer melt [51]. The colored lines show the multimode fit for G' and G'' while the curve corresponding to each mode are shown in the various thin black lines.

This fitting of the linear viscoelastic spectrum by the *relaxation spectrum* is the first step in the constitutive modeling of these materials. Then, what one needs to predict the nonlinear response of the material is a *constitutive model* relating the linear viscoelasticity to nonlinear viscoelasticity.

Boltzmann Superposition Principle

Lastly, an important concept in viscoelasticity is the notion of *deformation history* since viscoelastic materials, which have time-dependent modulus, have memory of the previous deformations experienced. This memory de-

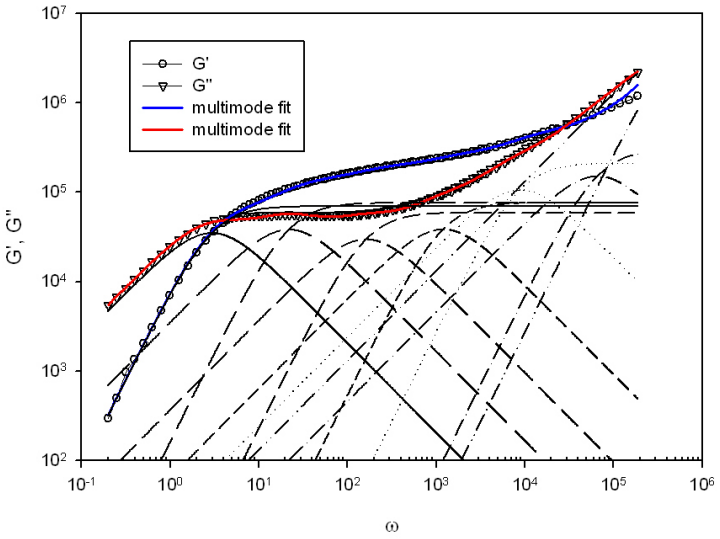

Figure 1.7: Fitting the dynamic moduli for a monodisperse PS melt using multiple Maxwell modes

cays when time of the order of the characteristic time τ of the material has elapsed.

For materials which experience successive applications of deformation, the *Boltzmann superposition principle* provides an expression for the resulting stress,valid in the limit of small or linear deformations. Consider an incremental strain $\delta\gamma_i$. The change in the stress would then be

$$\delta\sigma_i = G\delta\gamma_i = G\dot{\gamma}\delta t_i \tag{1.27}$$

where the strain $\delta\gamma_i$ can also be written in terms of the strain rate $\dot{\gamma}_i$.

The Boltzmann superposition principle states that the resulting stress from the combination of such small deformations is simply the linear combination of the stresses from each deformation. Hence, the total stress is simply (1.27) summed over all i deformations.

$$\sigma = \sum_i \delta\sigma_i = \sum_i G\delta\gamma_i = \sum_i G\dot{\gamma}\delta t_i \tag{1.28}$$

One can then rewrite the sum in (1.28) as an integral over the entire deformation history of the material.

$$\sigma = \int_{-\infty}^{t} G(t-t')\dot{\gamma}(t')dt' \tag{1.29}$$

This can also be expressed in terms of the *memory function* $M(t) = -dG(t)/dt$ and strain profile in time rather than the strain rate.

$$\sigma = -\int_{-\infty}^{t} M(t-t')\gamma(t')dt' \tag{1.30}$$

where the minus sign in the definition of $M(t)$ is added to keep the function positive and is carried over in the integral.

Equations (1.29) and (1.30) form the basic outline of constitutive equations which relate stress with the deformation history. A molecular approach for arriving at such a specific model is outlined in the following section.

1.3.5 Tube Model: Doi-Edwards Theory

Basic Concepts

The starting point for any molecular model for polymer viscoelasticity would be some notion of polymer dynamics – i.e. how polymers move. In the case of liquids (solutions or melts) of polymers with short chains, a foundational framework would be the Rouse model [52, 53] which describes the chain as a series of beads connected by elastic springs. Each bead would move subject to both Brownian motion and the constraint that it is connected to other beads by means of the springs imparting elastic forces. This model predicts a scaling of the characteristic time of Rouse motion τ_R, also called the *Rouse time*, as $\tau_R \sim M^2$ and a scaling of the zero-shear viscosity η_0 with the molecular weight M of the chain as $\eta_0 \sim M$.

However, it was shown by experiments on flexible polymers spanning a broad range of M [54, 55] that longer chains (in both melt and solutions) do not exhibit such scaling. Instead, they exhibit a much stronger dependence of η_0 with M so long as $M > M_c$ where M_c is called the critical molecular weight. The observed scaling law is $\eta_0 \sim M^{3.4}$ [55]. This change in scaling behavior is attributed to the increasing overlap of the chains that give rise to *topological interactions* due to chain uncrossability – so-called *entanglements* which slow down chain motion significantly.

Inherently, this problem of polymer dynamics is complex as it is cooperative and many-body in nature, unlike in the Rouse regime where the motion of each chain can be considered in isolation. An important stride in simplifying the system would be to consider a *mean-field* approach to reduce

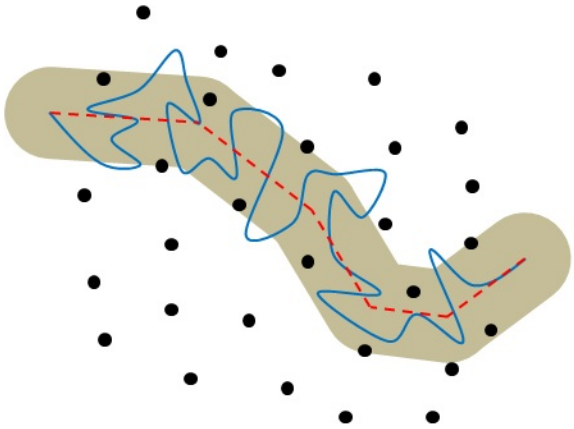

Figure 1.8: The Tube Model: The presence of constraints (black dots) on a test chain (blue curve) confine it to a tube-like region (gray area) that can be represented by the primitive path (red dashed line).

the many-chain problem to problem of a single chain in an effective field. One can then consider a chain, called the *test chain*, and identify how these topological interactions affect or restrict its motion. Considering the case of a chain in a polymer network, Edwards proposed that chain motion is restricted to a tube-like region [2] due to the presence of constraints provided by the neighboring chains as shown in fig. 1.8. This tube is characterized by a *primitive path* which defines the tube axis and has the same topology as the tube.

At equilibrium, the primitive path is a random of walk of step length a, called the tube diameter, and with the same end-to-end vector $\mathbf{R}$ as the test chain. Hence, the following relationship is obtained

$$Nb^2 = Za^2 \tag{1.31}$$

where Z is the number of entanglement segments. If there are N_e monomers in an entanglement strand and $N_e = N/Z$, it follows that

$$N_e b^2 = a^2 \tag{1.32}$$

and this is an alternative definition of the tube diamater. Equivalently, one can define M_e, the *entanglement molecular weight* which also relates to Z.

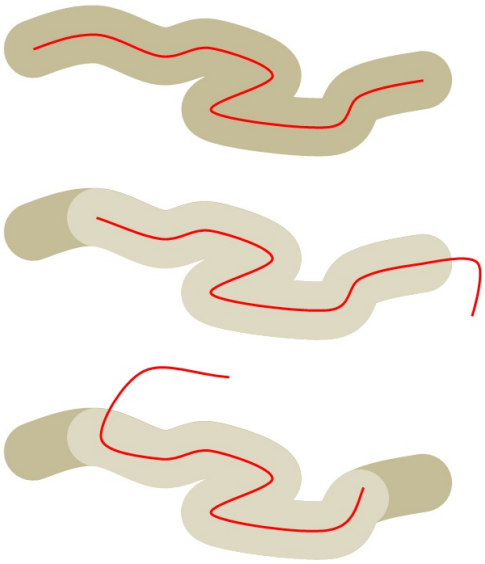

Figure 1.9: Reptation: The presence of the tube-like constraint prevents lateral chain motion and the only allowed motion of the chain is along the tube axis. Over time, the chain explores new areas through this motion reducing the fraction of the original tube constraint still active.

$$Z = \frac{M}{M_e} = \frac{N}{N_e} \tag{1.33}$$

Note that the term tube diameter can be a bit misleading since it pertains to a length scale along the tube axis and not lateral to it unlike a real "diameter" At equilibrium, the ratio between them is assumed to be of order 1.

By extending the tube concept to melts, de Gennes identified that polymer motion would be highly restricted laterally from the tube axis and that the only permissible motion would be the slow snake-like motion of the chain along the tube-axis. This motion is called reptation [3] and is illustrated in fig. 1.9. This assertion was certainly a step in the right direction though its predicted scaling for the zero-shear viscosity is $\eta_0 \sim M^3$, quantitatively different from what has been observed in experiments [54, 55]. It does, however, provide a molecular picture for understanding how stress relaxation in entangled systems occur. This has been presented by Doi and Edwards [1] by considering the diffusion of the chain in the tube. The relaxation function predicted is

$$G(t) = G_0 \sum_{p,odd} \frac{8}{p^2\pi^2} \exp\left(-\frac{p^2 t}{\tau_D}\right) \tag{1.34}$$

where τ_D is the *reptation time* and G_0 is the so-called *plateau modulus*. In terms of the other molecular parameters, τ_D is defined as

$$\tau_D = \frac{\zeta_0 N^3 b^2}{\pi^2 k_B T}\left(\frac{a^2}{b^2}\right) \sim 3Z\tau_R \tag{1.35}$$

where ζ_0 is the monomeric friction and τ_R is the Rouse time. Note that since τ_D is always larger than τ_R by a factor of about $3Z$, relaxation by reptation is a longer process than Rouse relaxation. However, it is the one that governs terminal relaxation and, ultimately, the viscosity. These two time constants also factor in the behavior of the systems in the nonlinear regime.

A final comment should be made about the plateau modulus G_0 which is a concept generalized from the modulus of a polymer network. In the Doi-Edwards model, this is defined as

$$G_0 = \frac{4}{5}\frac{\rho RT}{M_e} \tag{1.36}$$

where M_e is the molecular weight of an entanglement strand defined previously. For tube models for linear viscoelasticity, one has to specify two molecular parameters independent of the molecular weight – one is the basic length-scale (M_e or, equivalently via (1.36), G_0) and the other is the basic timescale (τ_e) from which expressions for τ_D and τ_R can be derived.

$$\tau_R = Z^2\tau_e \tag{1.37}$$

$$\tau_D = 3Z^3\tau_e \tag{1.38}$$

Note that as various definitions of these basic parameters have been presented in literature, one has to be careful in minding parameter consistency across definitions [56].

Doi-Edwards Constitutive Equation

While the reptation idea forwarded by de Gennes [3] has been explored for interpreting linear viscoelasticity, the main advance of Doi and Edwards has been the formulation of a *constitutive equation* for nonlinear viscoelasticity based on tube and reptation ideas. Not without shortcomings, the

formulated constitutive equation offers a good example of a bridge between microscopic physics and macroscopic observables [6, 50].

To understand the idea behind the model, the simplest case for nonlinear viscoelasticity can be considered – the case of stress relaxation after a large step-strain. Different from the case of a small step-strain discussed in 1.3.4, in this case the nonlinear modulus G is a function of both time t and strain γ. It has been found that this modulus $G(t, \gamma)$ obeys *time-strain separability* or is factorizable into time-dependent and strain-dependent components, i.e.

$$G(t, \gamma) = G(t)h(\gamma) \tag{1.39}$$

where the strain-dependent part $h(\gamma)$ is called the damping function. The damping function is experimentally observed to be a decreasing function of the imposed strain [5], a fact attributed by Doi and Edwards to the mechanism of *chain retraction* active only for nonlinear deformations. This mechanism controls the strain-dependent component of the response while reptation governs the time-dependent response of the material.

In the Doi-Edwards model, the retraction process is assumed to be a Rouse-type process and is therefore governed by the Rouse time τ_R. However, considering the case where the stress in chains are due only to the *orientation* of tube segments and not to the *stretch* of the chain in the tube, this retraction process can be assumed to occur instanteneously while reptation certainly requires a longer time to occur. In this regime where only retraction has occured, the expression for the stress becomes

$$\sigma = 3\nu k_B T \langle \mathbf{uu} \rangle = 3\nu k_B T \left\langle \frac{\mathbf{u}' \cdot \mathbf{E}\mathbf{u}' \cdot \mathbf{E}}{|\mathbf{u}' \cdot \mathbf{E}|^2} \right\rangle \tag{1.40}$$

where $\mathbf{E}$ is the deformation gradient tensor defined earlier. Under the *independent alignment approximation*, this expression can be rewritten as

$$\sigma = \frac{3}{5}\nu k_B T \mathbf{Q} \tag{1.41}$$

where $\mathbf{Q}$ is the universal Doi-Edwards Q-tensor which contains the details on the chain retraction process due to deformation and the prefactor 3/5 is due to IAA (i.e. if one does not invoke IAA, a different prefactor must be used to ensure that the stress reduces to the correct linear limit).

In the case of continuously applied deformation or in the general flow scenario, the stress must then be given by a history integral to account for the memory of the material due to viscoelasticity. For the Doi-Edwards model, this integral is as follows

$$\sigma = G_N^0 \int_{-\infty}^{t} m(t-t')\mathbf{Q}[\mathbf{E}(t',t)]dt' \tag{1.42}$$

where $m(t-t')$ is called the memory function and is defined in the previous section as $m(t-t') = -dG(t-t')/dt'$. Note the similarity in form with (1.30) for linear superposition. This is non-trivial since (1.30) was developed by assuming linearity of deformation. In this case, while the the deformation is nonlinear, the contribution of the deformation on the stress at each time interval is assumed to be linear as a consequence of the time-strain separability of G, shown in (1.39).

The validity of the Doi-Edwards model has been attributed largely to the success of the model and its consistency with experimental measurements of the damping function [57, 58] as well as in the mathematical form of (1.42) which belongs to the K-BKZ family of constitutive equations, sought after phenomenologically [50]. However, the model does predict some unusual features not observed previously in experiments such as an instability in the flow curve in shear [7] shown in fig. 1.10. As will be discussed in the following section, the issue of this instability has been resolved a few years ago only by considering additional mechanisms to the basic model.

1.3.6 Extensions of the Doi-Edwards Theory

Contour Length Fluctuations, Constraint Release

From the previous section, it is clear that the basic tube model as formulated by Doi and Edwards [1] has both successes and shortcomings in predicting both linear and nonlinear viscoelasticity. Over the years, extensions to the basic theory have been proposed to amend or improve predictions in various situations. For linear viscoelasticity, it has been recognized that at least two additional non-reptative mechanisms must be included to obtain quantitative predictions, at least in the case of monodisperse melts [59].

The first of these is *contour-length fluctuations* (CLF) that accounts for the difference in dynamics experienced by chain segments in the middle of the chain and chain ends. The latter are obviously less confined and their short-time motion allows the release of stress since they can renew tube orientation near the ends. This introduces a $1/Z$-order correction to the relaxation modulus and accelerates reptation since there is only a fraction of the tube surviving that must be relaxed by reptation [59, 60].

The other correction is *constraint release* (CR) and accounts for a more consistent view of the tube of constraints. The idea is that the tube con-

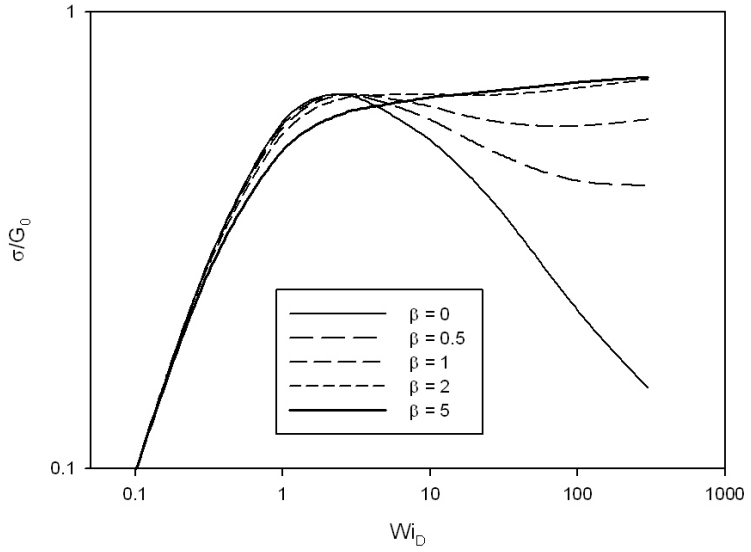

Figure 1.10: Non-dimensional shear stress-shear rate flow curve illustrating the Doi-Edwards instability. Calculations are done using a simplified tube model discussed in 4.2.1 with the nonlinear parameter β. $\beta = 0$ corresponds to the flow curve predicted by the original Doi-Edwards model.

straining the test chain are formed by other chains as well. Hence, it cannot be assumed that the tube will remain static, waiting to be relaxed by the test chain while there is simultaneous relaxation of the other chains. There are various formulations of this concept proposed in literature, an exhaustive discussion of which is beyond the scope of this introduction [61, 62, 63, 64]. The point is that, even at equilibrium, the diffusion or relaxation of the obstacles affords local motion of the tube which translates to stress relaxation.

Advanced formulations of both effects are included in a quantitative version of the tube model by Likhtman and McLeish [59]. Their inclusion significantly improved model predictions, including the $\eta_0 \sim M^{3.4}$ scaling different from the basic reptation prediction. In particular, it is the single-chain effect of CLF that is understood to be responsible for this 3.4-power law [65].

Chain Stretch

For nonlinear viscoelasticity, the basic Doi-Edwards model considers only the affine deformation of the system in flow and the instantaneous relaxation of a part of the stress by chain retraction and relaxation of the other part by reptation. This is valid for flows which are sufficiently strong enough to orient the chains but not stretch them. As orientational relaxation is governed by τ_D while the chain retraction process is governed by τ_R, this would be the case for $1/\tau_D < \dot{\gamma} < 1/\tau_R$.

However, for flows with rates larger than the inverse of the Rouse time, i.e. $\dot{\gamma} > 1/\tau_R$, chain retraction cannot be assumed to proceed instantaneously to preserve tube length. Hence, one must account for the possibility of chain stretching [1, 66, 67, 68]. In such a case, the stress expression from (1.42) will then be written as

$$\sigma = G_N^0 \lambda^2 \int_{-\infty}^{t} m(t-t')\mathbf{Q}[\mathbf{E}(t',t)]dt' \tag{1.43}$$

where λ is the chain stretch defined as the ratio between the present tube length L and the tube length at equilbrium L_0.

$$\lambda = \frac{L}{L_0} \tag{1.44}$$

The physical picture here is that for flows in the chain stretching regime, the surroundings of the molecule are convected by flow and the molecule stretches due to drag arising from this convection. This results in an increase

in the length of the tube as well as a further build-up in the stress beyond that predicted by the original Doi-Edwards model.

Chain stretching manifests in the transient response in shear flows as an overshoot in the shear viscosity and in the first normal stress difference [68] and in the large shear rate branch of the flow curve in steady flows, as shown in fig. 1.10. Note that while the inclusion of chain stretch in tube models allow the prediction of these phenomena, earlier models [66, 67] that include this effect consider chain stretching to be a transient phenomena in shear. Hence, the instability in the steady shear flows would still exist.

Convective Constraint Release

While chain stretch is an important consideration for very fast flows with rates $\dot{\gamma} > 1/\tau_R$, another relaxation mechanism that occurs in even slower flows could be integral in modeling the nonlinear response of entangled polymers. This mechanism proposed previously by Marrucci [45] and further developed by Ianniruberto and Marrucci [46, 69] is called *convective constraint release* (CCR). It is similar to the the constraint release process that occurs in the linear regime although it is active only in nonlinear flows.

The proposal hinges on the idea that the tube of constraints on a test chain is formed by other chains. In the linear regime, these other chains can undergo *diffusion* or reptation thereby allowing some local renewal of topology and local relaxation of the stress [70]. For the nonlinear flow regime, a similar additional topological renewal could occur when the surrounding chains undergo *convection* by flow. Based on the proposal of Marrucci, these two mechanisms would operate in parallel and give rise to an effective relaxation time which can be written simply as

$$\frac{1}{\tau} = \frac{1}{\tau_0} + \beta\dot{\gamma} \tag{1.45}$$

The effective relaxation time τ of the system would be due to reptation and diffusive/thermal constraint release that occurs at a rate of $1/\tau_0$ and this new effect of convective constraint release has a rate proportional to the flow rate $\dot{\gamma}$ with an unknown proportionality constant β, called the CCR parameter. In the absence of further understanding of the effectiveness of CCR, β is unknown and becomes an additional nonlinear parameter for the system, typically assumed to be of order unity. Note that setting $\beta = 0$ will recover the linear limit.

Since all the quantities in (1.45) are positive, it is easy to see that τ is much smaller than τ_0. Therefore, the over-all effect of CCR is to accelerate

the relaxation of orientation (which would otherwise be governed by τ_0). This is the main effect considered in the original proposals [45, 46, 69]. Later, it was recognized that CCR affects not just orientational but also stretch relaxation [71, 72, 73]. Hence, more recent constitutive equations would incorporate both CCR and chain stretching for nonlinear flow predictions. For sufficiently large values of β, such models could also better predict the experimentally measured flow curves for shear. For example, the model of Mead, Larson and Doi which includes both CCR and chain stretch as well as CLF predict a monotonic flow [71]. This model, as well as others, will be the subject of the following section.

State-of-the-Art Tube Models

In the previous sections, various additional relaxation mechanisms to improve the predictions of the basic Doi-Edwards tube model have been discussed. The development of models which account for these important physics has resulted in reasonable, if not excellent, predictions of experimental data for entangled systems. In the linear regime, the aforementioned theory of Likhtman and McLeish [59] provides quantitative fitting of linear viscoelastic data. A similar level of success has also been achieved by the time-marching algorithm developed by van Ruymbeke and co-workers [74] by incorporating similar physics. Indeed, it is also worth mentioning that semi-quantitative models for the linear viscoelasticity of branched polymers have also been developed for stars [75] and even more complex architectures [76, 77] by invoking the tube dilation concept for constraint release [63, 78].

For the nonlinear regime, tube models which incorporate CCR and chain stretch have also been formulated starting from the model of Mead, Larson and Doi [71]. Simple single-segment constitutive equations which do not consider fluctuations have also been developed by Ianniruberto and Marrucci [72, 79, 80]. Finally, the most detailed nonlinear tube model that resolves dynamics below the scale of tube segments has also been formulated by Graham and co-workers [73]. This full model is formulated as a stochastic differential equation and allows prediction of neutron scattering patterns in flow [15] but is quite cumbersome for flow solving calculations. A simplified version, called the Rolie-Poly model [81], was also then presented and was shown to give similar predictions as the full model. It is also worth mentioning that models with the same level of description in the case of branched polymers are far less developed and the most significant advance in connecting the branching structure to rheology has been the Pom-Pom model by McLeish and Larson [82].

The predictions of such models have been examined largely on experiments in shear flows as generating data on monodisperse entangled systems under extensional flow, particularly at the steady state, has been more challenging. The advent of improved methods for extensional rheometry [11, 12] has somewhat changed this situation and there is an increasing data set in literature with which makes comparison with theories possible. These data sets will be considered in Chapter IV. The predictions of some of the mentioned equations will also be verified on sighly more complex superposition flows in Chapter III.

Lastly, it is evident that there are a number of effects that one must consider in predicting the viscoelastic behavior of materials. Hence, simulation methods which have far less assumptions or which can treat these effects numerically have emerged as an important compliment or alternative at arriving at such predictions. These simulation methods and their applications will be the subject of the following section.

1.3.7 Molecular and Mesoscopic Simulations

Atomistic Simulations

Methods for molecular simulations are reasonably well-developed. In the ideal scenario, one would like to do this for atomistically-detailed models, i.e. models which fully resolve chemical structure to accurately describe the nuances in the interactions between polymers. However, resolving the full dynamics of the system, which involves a distribution of timescales all the way up to the terminal relaxation, would be difficult. Likewise, the system size which can be handled by present computers is also limited. Hence, such a luxury is seldom afforded and coarse-graining (or less finer descriptions) of the system are required [83]. Most simulations of the atomistic type have been done only for unentangled melts [83] until the work of Harmandaris and co-workers [84] where the crossover from Rouse to reptation dynamics was demonstrated for a series of polyethylene melts.

However, atomistic simulations still find application in the resolution of polymer dynamics problems which could be dependent on monomer chemistry. An example is the work by Ianniruberto and co-workers on non-equilibrium molecular dynamics simulations of polystyrene oligomers [85] in fast shear flows. The simulations report measurements of the diffusion coefficients of the oligomers as well as monomer friction coefficients and the effects of fast flow. They observe the breaking down of the Einstein relationship between diffusivity and friction coefficient far from equilibrium as

well as the reduction of the latter due to alignment of the monomers [85], akin to what occurs in liquid crystals. This observed effect proves to be important in capturing the rheological behavior of PS melts in extension as will be shown in Chapter IV.

Coarse-Grained Molecular Dynamics Simulations

Coarse-graining or reduced representations of the system where one particle represents a collection of subparticles is done to extend the timescales and system sizes accessible given limited computational power. This allows substantial increase in the simulation time and allows for a more generic description of polymers, an example of which is the bead-spring model of Kremer and Grest [16]. Simulations on entangled systems using this model have been done both to directly determine the linear viscoelastic behavior of polymer melts [86] as well as to verify assumptions and constants typically assumed in tube theories [19]. Methods for projecting these bead-spring models into primitive paths [17, 28], termed *primitive path analysis*, have also been developed and was used to analyze the nature of discrete entanglements recently [87]. A less destructive alternative to this analysis, called *mean path analysis*, has also emerged recently [88] based on the concept of a mean path by Read and co-workers [18]. Despite these advances and the amount of useful information that can be derived from such simulations, simulations of this type are still limited to light to moderately-entangled systems at best due to still huge computational costs.

Slip-link Simulations

In terms of computational cost and accessible timescales, the most promising simulation methods for entangled polymers are the so-called *slip-link simulations* developed as either single-chain or multi-chain models [28, 83]. Here, coarse-graining is at the level of tube or primitive path segments, dynamical evolution is made by integrating stochastic equations and entanglement constraints are incorporated in the form of slip-links. In multi-chain models such as the Primitive Chain Network model (PCN) by Masubuchi and co-workers [22], this constraint is placed in real space. This is shown in fig. 1.11 where a network of primitive chains that are made to evolve in time, similar to MD simulations albeit with less detail. In single-chain models [21, 24, 26, 27], this constraint is virtual and not explicit.

While the modeling of entanglements as discrete binary slip-links seems like an *ad hoc* way of coarse-graining, slip-link models provide a clear rela-

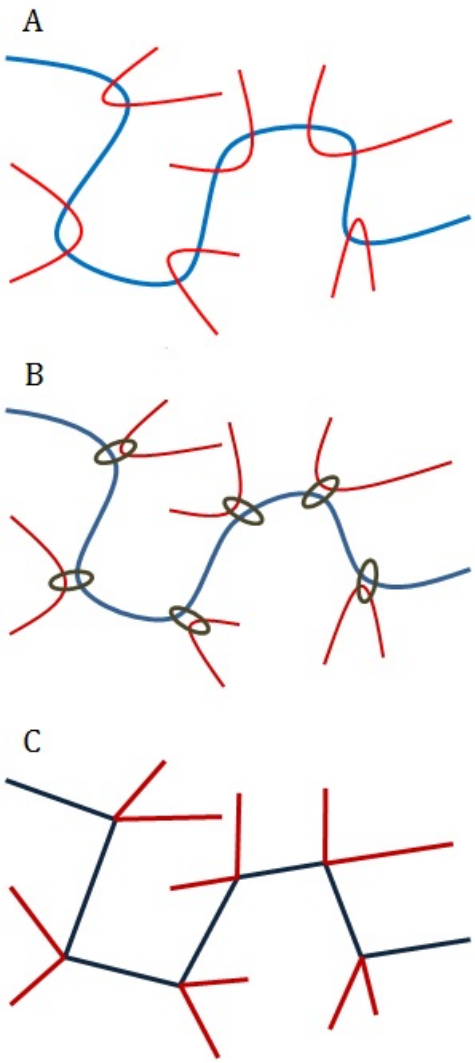

Figure 1.11: The Slip-link Model: The presence of other chains impose topological constraints on a test chain (A). These constraints can be represented by slip-links (gray circles) (B). Effectively, the system is then represented by a set of primitive chains (lines) and slip-link nodes (meeting point between lines) (C).

tionship with tube models and can access the full-range of rheological behavior of systems at low computational cost. Predictions can be obtained for both linear and branched polymers [23, 89] in linear and nonlinear viscoelastic regimes [90, 91]. In the case of the PCN model which will be discussed further in the context of entangled rubbers in Chapter 2, predictions can also be made for heterogeneous polymer systems such as blends and block copolymers to observe phase separation behavior [92].

Despite the success of some of these models, a shortcoming of these models is the thermodynamic consistency and fulfillment of the detailed balance condition for the simulations since a number of the elements and dynamics of the model are done heuristically through algorithms [93]. This has prompted the proposal of a new model by Uneyama and Masubuchi drawing from earlier work and with a more solid thermodynamic framework, where dynamics are derived from a free energy expression [94]. The said model, called the multi-chain slip-spring model combines elements from earlier models formulated in a consistent manner. Recent results for this model show reasonable prediction of equilibrium properties [94].

Another model proposed recently is the translationally-invariant slip-spring model of Chappa and co-workers which is another multi-chain model [95]. The emphasis of this other model is the preservation of equilibrium properties of the entangled fluid and translational and rotational invariance. Such models, while under development, hold promise as emerging alternatives to tube models which invoke some uncontrollable assumptions in modeling chain dynamics.

Chapter 2

Slip-Link Simulations of Entangled Rubbers

2.1 Introduction

Slip-link simulations [21, 22, 24, 26, 27] are emerging as an important approach for predicting entangled polymer behavior, complementary to more conventional tube models [1, 59, 71, 72, 73, 74]. In such simulations, entanglements are treated as discrete local entities that constrain chains in a manner similar to crosslinks in rubbers although slip-links are temporary. Hence, the entangled system is represented by a network of primitive paths connected temporarily by slip-links. This *slip-link network* can then be made to evolve in time by invoking stochastic dynamics, typically by using Langevin equations. Observables such as stress can then be calculated directly from ensemble averages on the network. With such a level of description, i.e. at the entanglement length scale, slip-link simulations are considerably cheaper to run than more detailed simulation techniques, e.g. bead-spring molecular dynamics (MD) simulations [16], and hence can be used to access the full spectrum of dynamics for moderate and well-entangled systems.

One successful slip-link model is the *primitive chain network model* (PCN model) developed by Masubuchi and co-workers [22, 96, 97]. Unlike other slip-link models which are single-chain mean-field models that account for chain connectivity only *virtually*, the PCN model is a many-chain model that accounts for real chain connectivity in physical space similar to MD simulations. However, as mentioned, it has considerable gain in computational power over the latter due to the level of description. Recent formulations of

the model have been applied to the rheological simulation of entangled fluids (melts and solutions) in both linear and nonlinear regime, in shear and elongational flows and can quantitatively predict linear viscoelasticity data [90] and semi-quantitatively predict nonlinear viscoelasticity data [91, 98, 99] with a level of success at least comparable to (if not better than) advanced tube-based models.

Oberdisse and co-workers have also previously applied the PCN model to entangled rubbers [41, 42], specifically end-linked rubbers where crosslinking occurs only in the chain ends hereby making a network with a monodisperse distribution of elastic strands between crosslinks. Such systems are simpler than most melts since networks and rubbers have a *quenched topology*, i.e. slip-links are fixed, while in melts and concentrated solutions, slip-links are continually created and destroyed giving rise to *topology renewal*. As such, they are the simplest physical system which can show the effects that entanglements have on polymer behavior.

The work of Oberdisse et al. shows a discrepancy between the results from simulations and predictions from replica theory [100, 101]. The replica model by Ball and co-workers [100] and revised by Edwards and Vilgis [101] is known to give a stress-strain relation that matches experiments well, as shown for example in fig. 2.1 where it is compared with data on model PDMS networks by Urayama et al. [102], and molecular dynamics simulations [103]. The discrepancy observed by Oberdisse et al. is more prominent at large deformations. This is striking since, as mentioned previously, the model has been quite successful in predicting both linear and nonlinear viscoelastic data for melts and solutions which are much more complex systems where entanglements come into play. Hence, application to entangled rubbers remain as a somewhat problematic scenario for the PCN model.

In this work, effort is given towards understanding why this discrepancy arises and possible ways to improve model predictions for this particular system are outlined. Two types of entangled rubber systems are confronted: end-linked systems based on the previous work of Oberdisse and co-workers [41, 42] and randomly cross-linked systems [104]. For the cross-linked case, better agreement with a standard constitutive models for rubber elasticity by Edwards and Vilgis [101] is observed, different from the end-linked case. Two possibilities for this discrepancy are then considered: (a) the possibility of entanglement stripping in networks at large deformations and (b) softening of the confinement potential at large strains as argued previously by Rubinstein and Panyukov [105]. Neither seem operative or sensible in the context of the PCN model. We also briefly confront the issue of thermodynamic consistency of the PCN model as pointed out by Schieber and

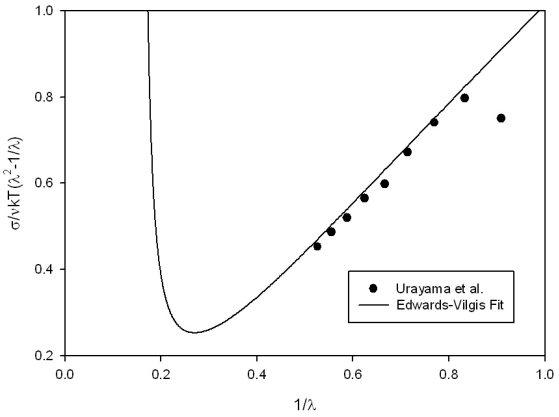

Figure 2.1: Mooney-Rivlin plot of the measured stress-strain curve for a model end-linked PDMS network and corresponding prediction using the theory of Edwards and Vilgis.

Horio [93]. In light of this, a new sliding equation is derived based on a free energy expression for a subchain by Schieber [106, 107] and it is shown here that this new sliding equation provides a slightly different response for the randomly cross-linked system. It is clear, however, that even this more thermodynamically-consistent sliding equation has no bearing in the previous issue with end-linked systems. Some possibilities on how to resolve this discrepancy will be given.

The chapter is organized as follows. First, a description of the PCN model and the methods for preparing the end-linked and randomly cross-linked networks are given. Results from these simulations are then presented and discussed. Possible explanations for the results in end-linked systems are then enumerated, and a derivation for an alternative sliding equation is also presented. Finally, some new simulation results using this new equation are presented. A short summary of the findings and some future outlook make up the conclusion.

2.2 Model Description

2.2.1 Dynamical Equations

In the PCN model, chains are described at the level of primitive path segments. In this context, each segment will be referred to as a subchain and

would consist of two slip-links (or nodes) with the positions $\mathbf{R}_i$ and $\mathbf{R}_{i+1}$ respectively and the number of monomers (or Kuhn segments) subsumed in each subchain n_i. These two quantities, node position and monomer number obey two Langevin equations that govern their dynamics.

Node Motion

The Langevin equation for the position of each node or slip-link $\mathbf{R}_i$ is written as follows.

$$\zeta(\dot{\mathbf{R}}_i - \boldsymbol{\kappa} \cdot \mathbf{R}_i) = \sum_{i=1}^{f} \mathbf{F}_i + \mathbf{F}_o + \mathbf{F}_r \tag{2.1}$$

The left-hand side is the total drag force on the node including the convection term $\boldsymbol{\kappa} \cdot \mathbf{R}_i$ with the friction or drag coefficient ζ while the right-hand side is the balance of all the other forces giving rise to the node motion. In this work, we consider only step-deformations applied to the networks instantaneously at $t = 0$ and released for $t > 0$. Hence $\boldsymbol{\kappa} = 0$ for $t > 0$.

The $\mathbf{F}_i$ term corresponds to the balance of the elastic forces exerted by each subchain on the slip-link and the index i goes from 1 to f, the functionality of the node (or the number of subchains participating in the slip-link). For binary slip-links which constrain two chains, $f = 4$ while for chain ends, $f = 1$. The expression for the elastic force of each subchain is simply the classical expression for entropic springs as follows.

$$\mathbf{F}_i = \frac{3kT}{n_i b^2} f(r_i) \mathbf{r}_i \tag{2.2}$$

where n_i is the number of Kuhn segments in the subchain, $\mathbf{r}_i$ is the subchain vector and $f(r_i)$ is the finite-extensibility factor that corrects for non-Gaussian behavior and which is simply 1 for Gaussian subchains. This comes from the following expression for the inverse Langevin force law for subchains with finite-extensibility [53]

$$\frac{F_i b}{kT} = \mathcal{L}^{-1}\left(\frac{r_i}{n_i b}\right) \tag{2.3}$$

where $\mathcal{L}^{-1}$ is the inverse Langevin function. The factor $f(r_i)$ is then as follows

$$f(r_i) = \frac{n_i b}{3r_i} \mathcal{L}^{-1}\left(\frac{r_i}{n_i b}\right) \approx \frac{1 - r_i^2/3r_{i,\max}^2}{1 - r_i^2/r_{i,\max}^2} \tag{2.4}$$

The rightmost side to (2.4) is the so-called Padé approximation [108] to the inverse Langevin function and $r_{i,\max}$ is the maximum extension of the subchain defined as $r_{i,\max} = n_i b$.

This force balance expression reduces to simple Rouse-dynamics of unconnected slip-links (i.e. nodes with only two subchains). For the case of a binary slip-link, this force balance concept is a correction to the Doi-Edwards theory proposed previously [109] since the original tube model does not satisfy this microscopic balance condition.

The term $\mathbf{F}_r$ corresponds to a random Brownian force with zero mean and variance given by the following.

$$\langle F_r(t) \rangle = 0 \tag{2.5}$$

$$\langle \mathbf{F}_r(t) \cdot \mathbf{F}_r(t') \rangle = 6kT\zeta\delta(t - t') \tag{2.6}$$

Lastly, the $\mathbf{F}_o$ term corresponds to an osmotic pressure term used to mimic excluded-volume effects in the PCN model, where the subchains are phantom, to eliminate network inhomogeneities in space. This term is important in simulations for entangled liquids where there is constraint renewal by creation and destruction of slip-links but somewhat less important for rubbers and will not be discussed further.

Monomer Sliding

The Langevin equation governing the sliding or monomer exchange across two subchains (of the same chain) in a slip-link is governed by the following equation.

$$\zeta_m v = F_m + F_m^r \tag{2.7}$$

where the left-hand side here is, again, the total drag force in the monomer exchange process, ζ_m is the sliding friction coefficient (different from the node motion friction ζ), v is the velocity of monomer exchange across the slip-link and F_m and F_m^r are the one-dimensional analogues of $\mathbf{F}_i$ and $\mathbf{F}_r$. Since there are only two subchains participating in these dynamics as opposed to four subchains in node motion, $\zeta_m = \zeta/2$, where we take the friction contribution of each subchain to be $\zeta/4$. In principle, the values for ζ and ζ_m should be determined locally by the number of monomers participating in a particular slip-link. However, to simplify the model, we simply assume that these friction coefficients are ensemble-averaged coefficients.

Here, what is required is an evolution equation for n and, hence, one must express v in terms of changes in n as follows

$$v = \dot{n}\frac{r_0}{n_0} = \dot{n}\frac{1}{\rho_m} \tag{2.8}$$

where ρ_m is the linear monomer density defined as the ratio n_0/r_0 at equilibrium.

The term F_m corresponds to the balance of the two elastic forces in each subchain across the slip-link. This elastic force balance term can be written as follows.

$$F_m = \frac{3kT}{b^2}\left(\frac{r_1}{n_1} - \frac{r_2}{n_2}\right) \tag{2.9}$$

In later versions of the PCN model [91, 97], different choices for the value of ρ_m have been made. For instance, one could choose ρ_m to be the linear monomer density of the segment which loses monomers based on this force balance – i.e. from the segment with the larger ratio of r_i/n_i [91]. One could also define ρ_m to be the average of the monomer densities of the two subchains [97].

The one-dimensional random force F_m^r like its three-dimensional counterpart has zero mean and variance defined as

$$\langle F_m^r(t)F_m^r(t')\rangle = 2kT\zeta_m\delta(t-t') \tag{2.10}$$

For numerical convenience, a minimum cut-off value for n_i can be defined, normally taken to be 0.1, to prevent 0 or negative monomer number values.

Both equations (2.7) and (2.1) can be discretized for stochastic simulations. These forms are presented in non-dimensional form in the following section.

Nondimensional Equations

For convenience, the equation of motions for $\mathbf{R}_i$ and n_i derived from the Langevin equations (2.1) and (2.7) can be nondimensionalized by rewriting the three main observables $\{\mathbf{r}, n, t\}$ as follows.

$$\tilde{\mathbf{r}} = \frac{\mathbf{r}}{\mathbf{r}_0}, \tilde{n} = \frac{n}{n_0}, \tilde{t} = \frac{t}{\tau_0} \tag{2.11}$$

where the denominators are the equilibrium values. τ_0 is defined as $n_0 b^2\zeta/6kT$, the equilibration time of the subchain segment, and the square of the equilibrium length of the subchain r_0^2 is defined as $n_0 b^2$, similar to the

tube diameter in Doi-Edwards theory [1]. In terms of these nondimensional quantities, the equation of motions for $\mathbf{R}_i$ and n_i derived from (2.1) and (2.7) are then as follows.

$$\Delta\tilde{\mathbf{R}} = \frac{\Delta\tilde{t}}{2}\sum_i f(\tilde{r}_i)\frac{\tilde{\mathbf{r}}_i}{\tilde{n}_i} + \sqrt{\Delta\tilde{t}}\,\mathbf{W} \tag{2.12}$$

$$\Delta\tilde{n}_i = \rho_m\left[\Delta\tilde{t}\left(\frac{\tilde{r}_1}{\tilde{n}_1} - \frac{\tilde{r}_2}{\tilde{n}_2}\right) \pm \sqrt{\frac{\Delta\tilde{t}}{6}}\right] \tag{2.13}$$

where $\mathbf{W}$ is a unit vector with random direction and ρ_m is the linear monomer density whose value is determined by the segment losing monomers, as mentioned previously. For details on the derivation and non-dimensionalization of these equations, the reader is referred to Appendix B. These equations are implemented in a numerical scheme for the stochastic simulations of the PCN model.

Topology Renewal

For topology renewal, we consider here the renewal of entanglements only at the chain-ends by hooking and unhooking, which corresponds to slip-link creation and destruction that occurs in entangled liquids (melts and solutions) but not in networks. This process is triggered whenever the monomer number in the subchain containing a chain end becomes greater than or less than a numerical threshold. In the original scheme presented [22], the thresholds are

$$0.5 < \tilde{n} < 1.5 \tag{2.14}$$

that is to say when the value of $\tilde{n}$ departs largely from the the equilibrium value of 1, the subchain becomes long enough to form a slip-link with another subchain and, conversely when the value becomes lower than the equilibrium value of 1, the subchain is too short to keep the entanglement and disentanglement occurs.

There are several choices for the actual geometry with which one can implement this creation-destruction process and the details of these schemes and their effects on equilibrium distributions of Z, r, n have been presented previously [97]. The main point here is to mention this process as an important routine in for topology or constraint renewal in liquids and this point will be revisited in the following section.

2.2.2 Network Preparation and Simulation Scheme

In the simulations for this work, we consider two types of entangled networks: end-linked networks and randomly-crosslinked networks. For the former, only the previous results generated by Oberdisse [41, 42] are considered and we review here the details involved in the preparation of these networks and in the simulation scheme. For the latter case, a different procedure is used by taking advantage of the full implementation of the PCN model called NAPLES developed by Masubuchi and co-workers for melts and solutions and the method of preparation for this case will also be covered here.

End-linked Networks

In the simulations by Oberdisse and co-workers [41, 42], the end-linked network is prepared first by creating chains as instances of random walks in a 3D box with periodic boundary conditions. The chain nodes (that are not chain ends) are connected with other similar chain nodes in its vicinity to form slip-links while chain ends are connected with other chain ends in the vicinity to form the end-links. The resulting nodes (consisting of two or more previous nodes now sharing a position in space) are then the nodes for the corresponding slip-link network.

Each slip-link node would have a functionality f or number of subchains equal to 4 (2 subchains from 2 chains) while each end-link node can have a functionality of 1, 2, 3 or 4. To form an ideal network with no dangling ends, the only acceptable values would be 3 or 4 for each node and the global average functionality is set to be $f > 3.95$ for the network to be considered close to ideal.

Note that since the original nodes are being displaced from their original positions, the process of creating the network induces some unnatural stretching, particularly for the chain end subchains since there are fewer chain ends and they have to travel a larger distance to find a connection. This unnatural displacement could be relaxed partly by allowing the system to equilibriate by switching on the dynamics for both node motion and monomer sliding discussed in the previous section. This equilibration releases some of the induced strain during network creation however it is insufficient in bringing down the ensemble averages of the observables closer to Gaussian network values shown as follows.

$$\langle \tilde{\mathbf{r}}_i^2 \rangle = \langle n_i \rangle b^2 = n_0 b^2 \tag{2.15}$$

$$\langle \tilde{\mathbf{R}}_j^2 \rangle = N_s \langle \tilde{\mathbf{r}}_i^2 \rangle \tag{2.16}$$

where N_s is the number of subchains in each original chain and $N_s - 1$ is the number of slip-links per chain.

The approach to equilibrium is monitored through the total energy of the system and the dynamics are run long enough for the fluctuations to average out and a constant free energy comes out as indication. This free energy is calculated based on the following expression.

$$\frac{E}{kT} = \frac{3}{2} \langle \tilde{n}_i \tilde{r}_i^2 f(\tilde{r}_i) \rangle \tag{2.17}$$

Equilibration is also understood to be important in eliminating some artifacts caused by not starting simulations with a random state [110].

After equilibration, the network is now ready for deformation to calculate its mechanical response. The deformation is imposed by moving all the beads, the box (and its periodic images) affinely, i.e. by applying the tensor $\mathbf{E}$ to each position vector $\mathbf{R}_i$, and letting the network relax. Due to the periodic boundary conditions, the network would then behave as if the deformation was imposed at infinity. After letting the network relax, in a manner akin to equilibration, the stress tensor which is defined as follows is calculated.

$$\boldsymbol{\sigma} = \nu \langle \tilde{\mathbf{F}}_i \tilde{\mathbf{r}}_i \rangle \tag{2.18}$$

where $\tilde{\mathbf{F}}_i$ is the elastic force of the subchain in terms of the nondimensional subchain length $\tilde{\mathbf{r}}_i$.

In the case of uniaxial extension, which is the only deformation considered here, the measured stress is in terms of the stress difference between the components of $\boldsymbol{\sigma}$ along the extension and lateral directions, i.e. $\sigma = \sigma_{xx} - \sigma_{yy}$.

Randomly-Crosslinked Networks

For the randomly-crosslinked network, the slip-link network is prepared from a pre-equilibriated melt of chains [104]. In this melt, the number of slip-links $Z = N_s - 1$ in each chain follows a distribution due to fluctuations [97] arising from the dynamics of node motion, monomer sliding as well as topological rearrangement, all of which are active during equilibriation. A fraction of the slip-links here are then converted into crosslinks hereby freezing topological renewal about that point, as shown graphically in fig. 2.2.

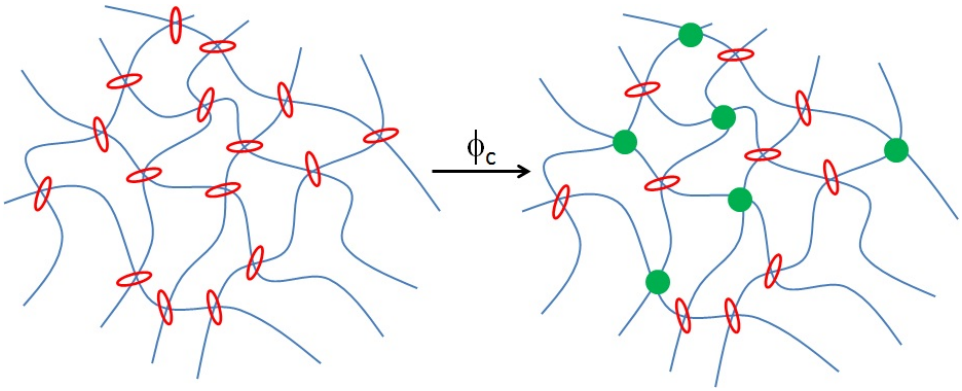

Figure 2.2: Preparation of a randomly-crosslinked entangled network from an entangled melt

For sufficiently large values of the converted fraction ϕ_c, we expect the formation of a percolating network which exhibits network behavior. To illustrate this, we show simulations done previously by Masubuchi for $Z = 5$ in fig. 2.3 [104]. This figure shows critical gel behavior for $\phi_c = 0.25$ and a prominent rubbery plateau emerges at $\phi_c = 0.5$. These findings are consistent with simple percolation theory [53] which predicts critical gel formation for $\phi = 1/(Z-1)$. This critical gel also manifests a power law behavior for both the storage and loss moduli, consistent with findings from experiments [111]. Note that there is viscous dissipation or relaxation even if one converts all the slip-links to crosslinks, as shown plot for $\phi_c = 1.0$ and this can be due to the presence of chain ends.

In this method, the starting point is an entangled melt equilibriated previously by switching on all the dynamics and has well-behaved equilibrium statistics. Hence, the resulting network is clearly in a suitable initial state for deformation experiments to be performed in a manner similar to that discussed for end-linked rubbers. The randomly-crosslinked networks prepared in this way are similar to actual networks where the length of the entanglement strand (or the number of entanglements between two crosslinks) follow distributions. In contrast, the entanglement strands (or the number of entanglements) in the previous case (end-linked networks) are strictly monodisperse.

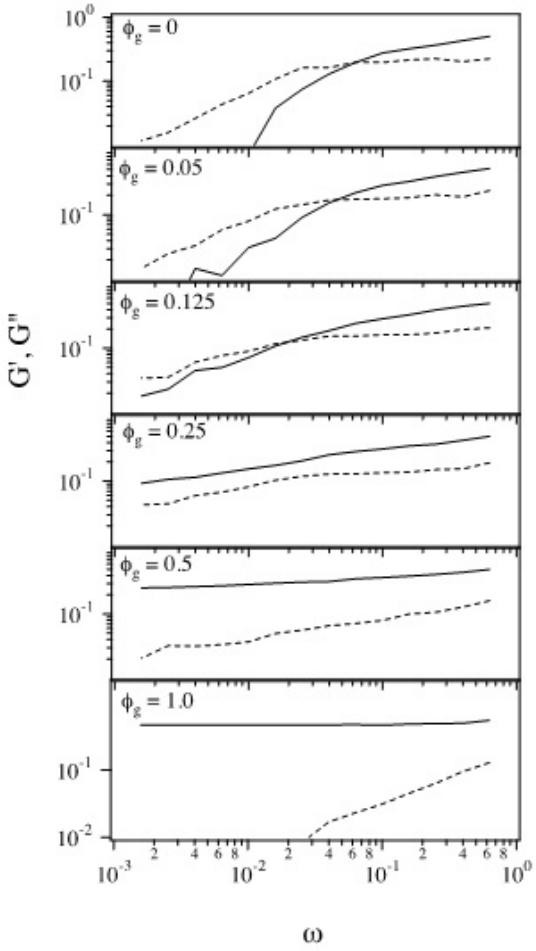

Figure 2.3: Storage and loss moduli for an entangled melt Z=5 with a fraction of slip-links converted into crosslinks from previous simulations of Masubuchi [104]

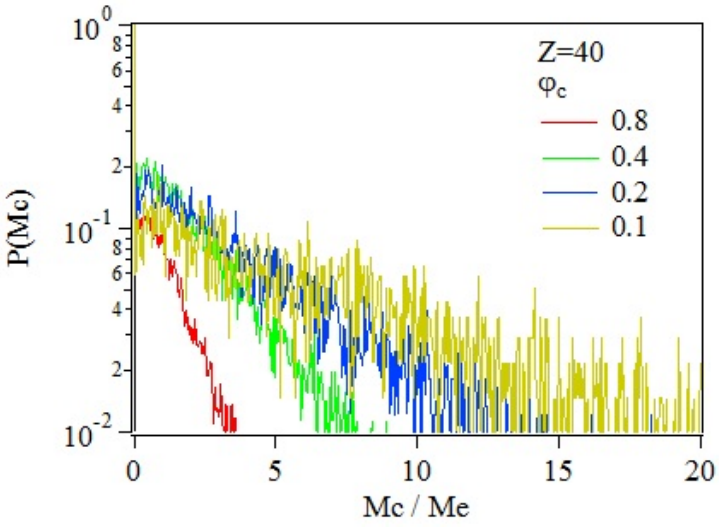

Figure 2.4: Distribution of the molecular weight between crosslinks for a melt with $Z = 40$ as a function of the crosslink fraction

2.3 Results and Discussion

2.3.1 Randomly-Crosslinked Networks

In this section, we present and discuss the results obtained from uniaxial extension of the randomly-crosslinked networks and compare them with the previous results of Oberdisse and co-workers [41, 42] for the end-linked case. Simulations here were done in a cubic cell of of length 8 (in non-dimensional units, where the equilibrium length of a subchain is 1) with periodic boundary conditions [112]. We maintain a segment density of 10 for all simulations, hence the number of chains for a simulation with Z segments is given by $5120/Z$.

The distribution of the length of the elastic strand in between two crosslinks (in terms of the molecular weight M_c) is shown in fig. 2.4 as a function of the crosslink fraction ϕ_c for a melt which originally had Z = 40 slip-links per chain. As expected the distribution becomes narrower for larger crosslink fractions and is much more broad for smaller crosslink fractions since longer strands have a likelihood of remaining undivided if one converts only a few slip-links into crosslinks. Knowledge of this distribution is relevant in understanding the mechanical behavior of random networks since shorter strands between crosslinks contribute more towards

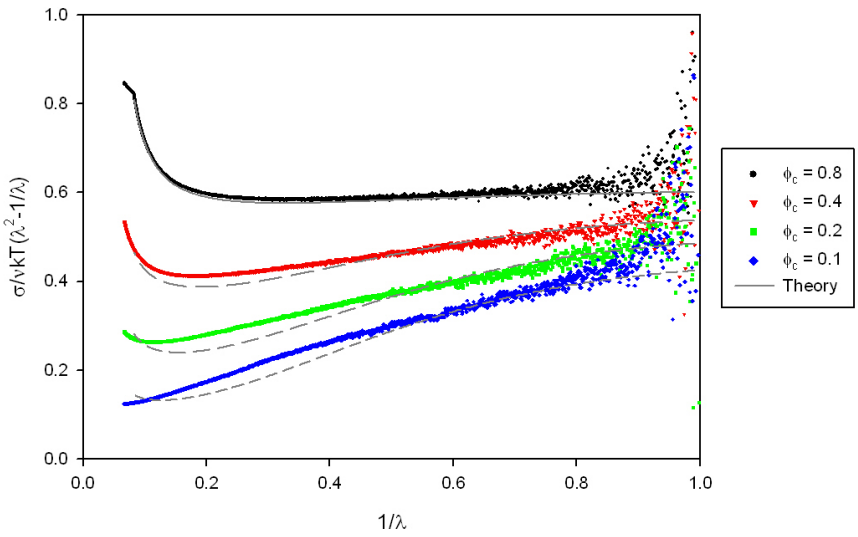

Figure 2.5: Mooney-Rivlin plot of the stress-strain curves for randomly-crosslinked networks with Z=40 and varying crosslink fraction ϕ_c: Curves are fits using the theory of Edwards and Vilgis.

the elasticity of the network while longer strands which have more slip-links contribute more towards relaxing stress since slip-links can release some tension by sliding.

The stress-strain curve for these networks with varying ϕ_c are then presented using the Mooney-Rivlin representation in fig. 2.5. The abscissa for this plot corresponds to the inverse of the applied elongational strain λ while the ordinate corresponds to the elongational stress σ normalized by the factor $\nu kT(\lambda^2 - 1/\lambda)$. νkT corresponds to the modulus of the network, where ν is the volume density of elastic strands for the system, while the factor $\lambda^2 - 1/\lambda$ comes from the stress expression for a Neo-Hookean solid [113]. In this plot, a neo-Hookean solid, which follows *affine deformation* would have a horizontal curve with a value of 1 for the normalized stress while materials that deform sub-affinely would have curves below this horizontal line. In particular, a positive slope in this plot is taken as a signature of entanglement effects in the elastic behavior [113].

The effect of the crosslink fraction is prominent in this plot. The largest crosslink fraction case $\phi_c = 0.8$ manifests an almost horizontal profile from small to large deformations at the normalized stress level close to 0.5 and

this reduction is attributed to the fluctuations of the nodes in space [96], as with *phantom networks*. The slope in the plot also becomes larger as the crosslink fraction becomes smaller, i.e. as the proportion of slip-links increase. This can be attributed to the trapped entanglements which are expected to induce further strain softening at large deformations. The plot also shows the divergence of the stress at large strains due to the finite-extensibility incorporated in the model (Gaussian networks do not exhibit this divergence).

Fig. 2.5 also shows gray curves corresponding to predictions using the theory of Edwards and Vilgis [101], a generalization of the replica theory presented earlier by Ball and co-workers [100] that includes finite-extensibility. Notice that contrary to findings of Oberdisse and co-workers [41], which are replotted here in fig. 2.6 , the results from the PCN model are well described by the calculations using Edwards-Vilgis for the model parameters.

In fig. 2.6 which is based on data reported previously [42] for end-linked networks, the effect of entanglements can again be seen from the limit of $Z = 0$ entanglements, which is a horizontal line with a Mooney-stress equal to half of the affine value of 1, consistent with phantom network predictions [53, 96] to increasing number of entanglements which exhibit a progressive increase in strain softening. The case of $Z = 8$ clearly compares poorly at large deformations with the result using the Edwards-Vilgis equation without finite-extensibility. It is also easy to see that comparison of the simulation result for $Z = 6$ with the experimental data of Urayama [102] for end-linked PDMS would exhibit similar disparity since the slope in the experimental data is much greater than that exhibited by the simulation result.

As mentioned previously, the results presented here are striking since the PCN model predictions for the more complex case of randomly-crosslinked networks appear to be less problematic than the insufficient strain softening predicted for end-linked networks. Certainly, the physical systems are different and, subsequently, the modeling scheme used to arrive at predictions for the two systems are also different, particularly the method of network preparation, and these differences might be significant. However, they are temporarily set aside in favor of the possibility that there might be a missing ingredient in the modeling framework. This ingredient which could be applied in all cases but only significantly affects the results for the end-linked system would be a non-trivial modification for the PCN model and is, hence, worth investigating. In the following sections, we examine two such possibilities explored in this work.

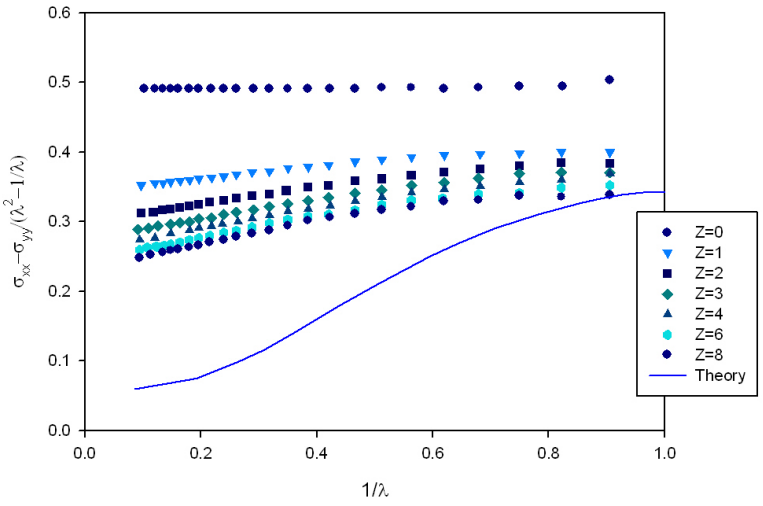

Figure 2.6: Mooney-Rivlin plot of the stress-strain curves for end-linked networks from previous simulations by Oberdisse et al. with varying slip-link number from $Z = 0$ to $Z = 8$: The curve, shown for comparison, is the calculation for Z = 8 using the theory of Edwards and Vilgis.

2.3.2 Entanglement Stripping at Large Deformations

The first possibility considered is the idea of *entanglement stripping* at large deformations which is based on the idea of weak and strong entanglements putforward previously. The existence of these strong and weak entanglements have been studied recently by Anogiannakis and co-workers [87] in both polyethylene networks and melts using molecular dynamics simulations. Hawke and Read also use this concept of strong and weak entanglements in formulating a model for the observed stress overshoots in extensional flows of low-density polyethylene [114] where entanglement stripping could occur at chain ends. Here, we consider entanglement stripping in the context of networks (which have no chain ends). While the exact physical mechanism for this is somewhat loose or uncertain, it is an effect which can introduced to the model and we can determine its impact on mechanical behavior here.

The working idea, in the context of the PCN model, is that some entanglements are weak or less persistent and are lost or stripped progressively as deformations become larger, i.e. as one goes from right to left in the Mooney-Rivlin plot. For instance, for the case of $Z = 8$, this entanglement number is valid only at low deformations (where the simulation results coincide with theory). At some larger deformation, the elastic response of the system corresponds to that of a system with $Z < 8$, as if a few entanglements were lost or stripped by applying the deformation. The question that remains is that of how much disentanglement must occur to obtain the spread of behavior predicted by Edwards and Vilgis [101].

To examine this working idea, one would ideally generate simulation results for an end-linked system with $Z = 8$ and total monomer number per chain $(Z + 1)n_0$. This would mean a monomer number of n_0 for each subchain. Succeedingly, one would generate results for $Z = 7, 6, 5, \ldots$ but keeping the same total monomer number per chain thereby increasing the monomer number for each subchain by a factor of $(Z + 1)/(Z_{\text{eff}} + 1)$ where Z_{eff} is the number of slip-links after disentanglement. This would result in a lower elastic force and a lower stress.

In the absence of a working code for an end-linked network, the other possibility would be to use the results generated previously by Oberdisse et al. [42] shown previously in fig. 2.6 and rescale them to obtain the same level of disentanglement as that proposed in the earlier paragraph. Specifically, consider the family of curves ranging from $Z = 0$ to $Z = 8$ shown in fig. 2.6. These calculations were made using chains with different total monomer numbers, $(Z+1)n_0$ to be exact, which is specific to the value

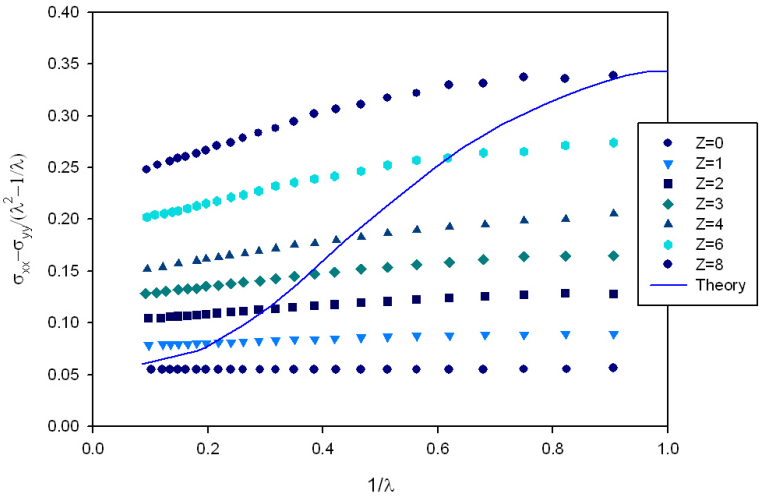

Figure 2.7: Mooney-Rivlin plot of the stress-strain curves for end-linked networks from previous simulations by Oberdisse et al. with varying slip-link number from $Z = 0$ to $Z = 8$ but rescaled by the factor : The curve, shown for comparison, is the calculation for Z = 8 using the theory of Edwards and Vilgis.

of Z, as well as by implicitly assuming the same density of elastic strands ν since the measured stress-strain curves for each value of Z are normalized by the same factor. However, what we require are simulations with varying Z, as in fig. 2.6, but for the same total monomer number chain corresponding to Z = 8 or, equivalently simulations for systems with lower densities of entanglement strands as a result of disentanglement. This rescaling of the density ν from its equilibrium value will then allow us to generate the desired family of curves, shown in fig. 2.7.

To obtain this density scaling factor, for the equilibrium Z, the total number of subchains per chain is $Z+1$, if there are N_c number of chains for the total volume V, the density ν is given by the expression.

$$\nu = N_c(Z+1)/V \tag{2.19}$$

After disentanglement, the remaining number of slip-links becomes Z_{eff} and, hence, the total number of subchains per chain becomes $Z_{\text{eff}}+1$ and hence the density is $\nu_{\text{eff}} = N_c(Z_{\text{eff}}+1)/V$. The ratio between these two densities then becomes

$$\frac{\nu}{\nu_{\text{eff}}} = \frac{Z+1}{Z_{\text{eff}}+1} \tag{2.20}$$

and this is the rescaling factor. The Mooney stress $\sigma/\nu kT(\lambda^2 - 1/\lambda)$ for $Z = 7, 6, \ldots$ should then be multiplied by the factor $(Z+1)/(Z_0+1)$ where $Z_0 = 8$ in the case considered here to obtain fig. 2.7.

Note that these rescaled results in fig. 2.7 cover the full range predicted from Edwards-Vilgis theory, which we assume is representative of behavior observed in experiments. This gives some credence to this disentanglement or entanglement stripping idea. However, to match the theory at large deformations, almost total entanglement release must occur resulting in the parent chain with $Z = 0$. Despite the idea that a fraction of the entanglements at equilibrium could be weak and, hence, possible to release or no longer active at large deformations, it seems physically implausible that all the entanglements will be released at large deformations.

The connection of this idea of strong and weak entanglements should also be discussed in light of the recent work of Anogiannakis and co-workers mentioned earlier [87]. Using MD simulations and the Creta algorithm [115] for extracting the primitive path, they investigated the nature of entanglements in polyethylene networks and melts. In their work, they define the strength of the entanglement in terms of the *persistence* of the contact between two chains. Some contacts are long-lasting and persitent, these are referred to as

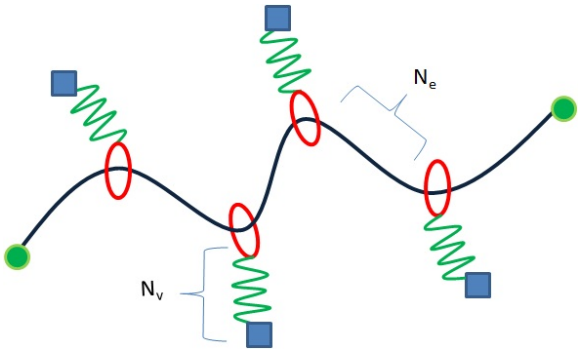

Figure 2.8: The Slip-Spring Model: Entanglement constraints are imposed on a chain by means of slip-links attached to virtual springs attached to the elastic background.

strong entanglements while other short-lived and temporary and correspond to weak entanglements and they hold that the weak entanglements do not contribute to the mechanical behavior of the material, even at low deformations. It is then clear that the number of entanglements at equilibrium, which determine the strength of the modulus, are all strong which would make the earlier approach of entanglement stripping more implausible and heuristic, at best.

2.3.3 Strain-Dependence of the Tube Potential

The second possibility considered is the strain-dependence of the tube potential proposed previously for entangled networks by Rubinstein and Panyukov [105]. In their model, entanglement constraints on a chain are represented by *virtual springs* that are attached to the affinely-deforming elastic background as shown here in fig. 2.8.

Here, the virtual springs represent the harmonic confinement potential that confine the chain in the tube-like region but allow fluctuations within the region. These springs do not contribute to the stress (which is only summed over the elastic forces corresponding to real subchains) though they do contribute in the fluctuations of the slip-link positions in space.

From renormalization arguments whose details are not presented here, Rubinstein and Panyukov argue that the strength of this confinement potential, represented by the monomer number in the virtual spring N_v, weakens with increasing deformation λ [105]. For instance, if one assumes, initially that $N_v = N_e$, where N_e is the monomer number in the elastic strand be-

tween slip-links, one would find that after a deformation λ that the virtual springs would stretch with the affinely deforming background and would, after renormalization, result in an effective confinement equal to λN_e. This would correspond to larger allowed fluctuations of the chain in the weakened harmonic potential which would lead to strain softening. From this idea, the same authors also propose a constitutive model for network elasticity [116].

To investigate the strength of this idea, we conducted stochastic simulations using a "toy" single-chain model where the tube constraint on the chain is represented by *virtual springs*. Similar to the slip-spring model of Likhtman [27] though at a more coarse-grained level of description, this is essentially a numerical version of the system considered by Rubinstein and Panyukov [105] which we evolve using the same dynamical equations for node motion and monomer sliding discussed previously in section 2.2.1 for the Primitive Chain Network model. This is then, essentially, a single-chain version of the PCN model where the fluctuations of the slip-link in space is governed by the force balance between the real chains and the virtual spring (as opposed to only real chains in the full multi-chain PCN model) and this introduces the parameter N_v in the system which regulates the virtual spring strength. Note that there is a difference in this "numerical implementation" with the model proposed by Rubinstein-Panyukov [105] as well as in the slip-spring simulation of Likhtman [27]. In their formulations, there is a certain degree of freedom in choosing the number of slip-links/virtual springs N_s which, based on renormalization arguments, would depend on the strength of the confinement N_v. In our toy model, we make the choice for N_s based on the number of entanglements Z for the system and we don't vary this choice.

Tentatively, we let $N_v = N_e$ in order to make the effect of the virtual spring confinement comparable to the elastic forces of the real chains. Then, we vary the ratio N_v/N_e to see the effects of softening the tube confinement potential on the mechanical behavior of this "toy" system. Note that for $N_v \gg N_e$ that the introduction of virtual springs would be meaningless and the chain will simply take on Rouse dynamics, subject to the constraint that the chain ends are also fixed to the affine background. In contrast for $N_v \ll N_e$, we recover the affine deformation limit since the virtual spring is infinitely strong and it would pull the chain to the elastic background.

Fig. 2.9 shows the results of the single-chain simulations for various values of the ratio N_v/N_e. Here, we see that while this slip-spring system does predict some inherent strain softening without varying N_v, as shown by the positive slope in the curves that this strain softening is, again, insufficient to match the softening predicted by the theory of Edwards and Vilgis [101].

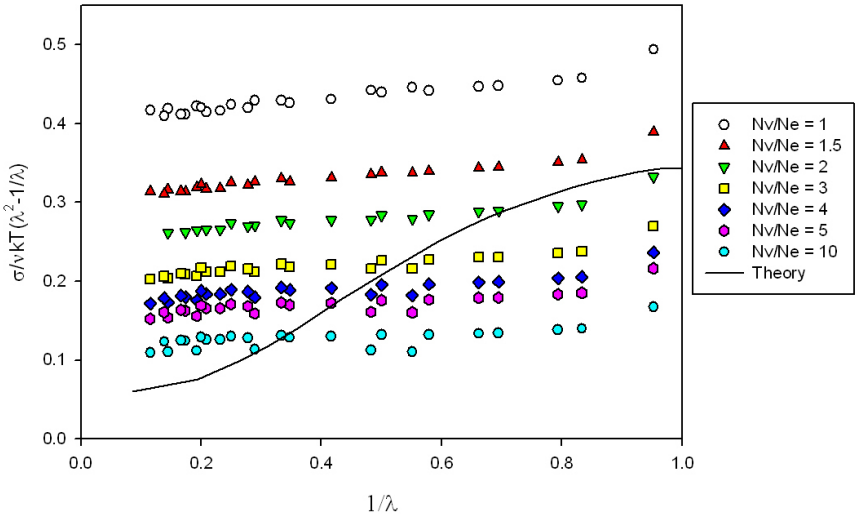

Figure 2.9: Mooney-Rivlin plot of the stress-strain curves obtained from single-chain slip-spring simulations with varying virtual spring strength for Z = 8: The curve show for comparison, is the calculation for Z = 8 using the theory of Edwards and Vilgis.

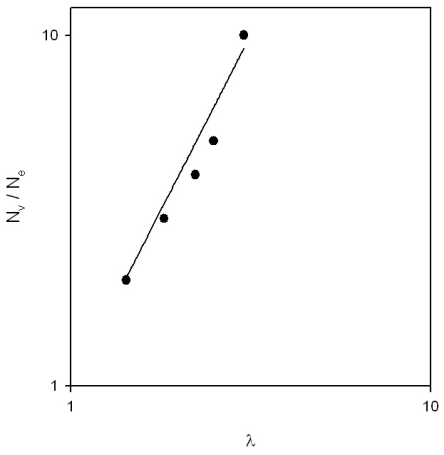

Figure 2.10: Plot of the relative virtual spring strength versus applied strain. Straight line shows the scaling prediction of Rubinstein and Panyukov $N_v \sim \lambda^2$.

This softening would be due to the monomer sliding dynamics which changes the system response from that of a phantom-like network to the positively sloped profile showed here.

It is also apparent from the family of curves generated by varying the ratio of N_v/N_e that the weakening of the confinement potential in this system allows full recovery of the predicted stress-strain curve from the replica theory of Edwards and Vilgis. Again, the underlying physical framework between the two are different but we are using the results from the latter as a representative of experimental data (which is somewhat sparse other than the work of Urayama [102]). At the lowest deformation, i.e. $1/\lambda \sim 1$, an $1.5 < N_v/N_e < 2$ seems to recover the correct low-deformation value of the stress and, hence, the modulus. For suceeding deformations, the value of this ratio must increase to match the theory all the way to $N_v/N_e > 10$ for larger deformations.

Indeed, if one plots the N_v/N_e ratio as a function of the λ with which this curve intersects the prediction of Edwards-Vilgis (which we take as representative of experimental data), one would obtain for the 5 data points generated here a rough power law with power equal to ~ 2, as shown in figure 2.10. This means that $N_v \sim \lambda^2$, somewhat consistent with the result of Rubinstein-Panyukov (see fig. 2c in [105]).

The connection of this idea to the real multi-chain PCN model, however, deserves further comment. While we have shown here that the idea allows recovery of the elastic behavior when applied to the "toy" single chain simulation we considered here, the connection of this to the multi-chain system is somewhat less clear since the confinement effect brought about by topological interactions or entanglements between chains are accounted for by the slip-link binding two chains together in the PCN model while these were introduced through virtual springs on the slip-links in one chain. The latter idea along with the progressive weakening of the virtual spring cannot be applied to the slip-links in the PCN model since there are 4 subchains participating in each link, making it a full network node and introduction of a weaker 5th spring will not alter its confinement brought about by the other 4 subchains. Hence, it is important to consider other possibilities to amend this discrepancy.

2.3.4 Chemical Potential-Driven Monomer Exchange in Slip-links

Lastly, we briefly consider the issue of thermodynamic consistency of the dynamics of the PCN model as pointed out by Schieber and Horio [93]. They argue that the monomer sliding equation, discussed in section 2.2.1, is inconsistent with the implied underlying free energy of the system. They put forward that a more rigorous choice or more thermodynamically-consistent choice would be to use the chemical potential as a driver of this monomer exchange.

A similar conclusion has been developed previously by Greco [117] by analyzing the subchain as a "small system" that is well outside the thermodynamic limit of many particles (where the "particles" here are Kuhn segments) and where fluctuations are important. Greco holds that the condition for inner equilibrium, arrived at by exchange of Kuhn segments across a slip-link (or what we refer to here as monomer sliding), is better stated by the condition that the chemical potential μ is equal for the two subchains – i.e. $\mu_\alpha = \mu_\beta$ where α, β refer to the two subchains. This is in contrast with the other choices one could make, for example that the tension f is equal for both subchains (as in the case of the PCN model [22]) or that the linear monomer density ρ_m is equal for both subchains. He holds that while all three conditions or choices are equivalent from the perspective of Doi-Edwards theory [1], they no longer hold when the subchain is more correctly treated as a "small system".

To improve the situation regarding this, we consider changing the equa-

tion for monomer dynamics by basing it on the chemical potential, as prescribed in the arguments of Schieber and Horio as well as Greco. This is one approach in developing a more thermodynamically-consistent many-chain slip-link model for entangled polymers. The other more involved approach is currently being undertaken by Masubuchi and Uneyama in their development of a new multichain slip-spring simulation [94] with a clear underlying thermodynamic framework.

To change the equation for monomer sliding, one would then require a free energy expression for the subchain, in terms of the observables $\mathbf{r}_i, n_i$ and from this, one can derive the chemical potential. Here, we use the free energy expression reported by Schieber for an entangled strand [106, 107].

$$F_{\text{subchain},i} = \frac{3}{2}\frac{kTr_i^2}{n_i b^2} + \frac{3}{2}\log N_i \tag{2.21}$$

The chemical potential μ_i for the subchain i is then given by the following expression.

$$\mu_i = \left(\frac{\partial F}{\partial n_i}\right)_{T,V} = \frac{3}{2}kT\left(\frac{1}{n_i} - \frac{r_i^2}{n_i^2 b^2}\right) \tag{2.22}$$

Schieber also presents a sliding equation based on this expression for μ [107].

$$\Delta n_i = \frac{1}{kT\tau_K}\left(\mu_{i+1} - \mu_i\right)\Delta t \pm \sqrt{\frac{2\Delta t}{\tau_K}} \tag{2.23}$$

The following non-dimensional observables can then be defined.

$$\tilde{n} = \frac{n}{n_0},\ \tilde{r} = \frac{r}{r_0},\ \tilde{t} = \frac{2t}{\tau_K n_0^2} \tag{2.24}$$

And by using the definitions in (2.24) and combining equations (2.22) and (2.23) one can obtain the following discrete non-dimensional form for this new sliding equation.

$$\Delta\tilde{n} = \frac{3}{4}\Delta\tilde{t}\left[\left(\frac{\tilde{r}_i^2}{\tilde{n}_i^2} - \frac{\tilde{r}_{i+1}^2}{\tilde{n}_{i+1}^2}\right) + \left(\frac{1}{\tilde{n}_{i+1}} - \frac{1}{\tilde{n}_i}\right)\right] \pm \sqrt{\Delta\tilde{t}} \tag{2.25}$$

This last equation is then implemented in the numerical scheme for stochastic simulation in lieu of (2.13). Note that the characteristic time τ_K introduced by Schieber in equations (2.23) is the timescale for the motion of a single Kuhn step. Since it becomes included in the non-dimensionalization of t in (2.24) and we are only concerned with observables at equilibrium,

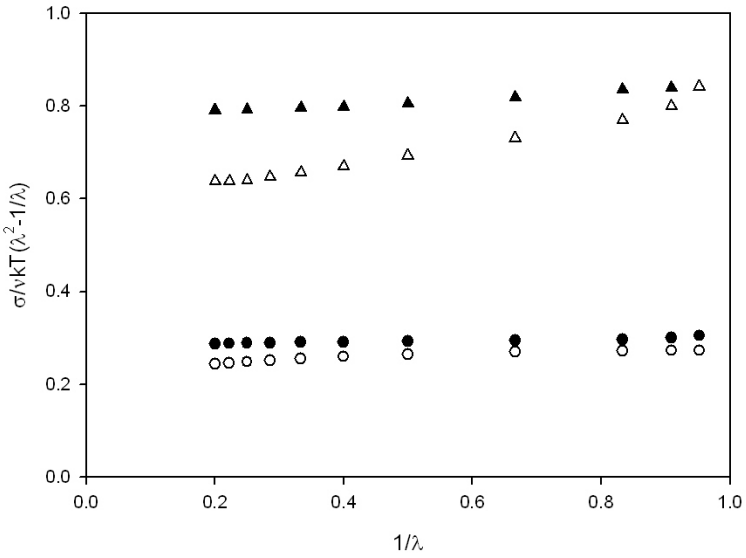

Figure 2.11: Mooney-Rivlin plot of the stress-strain curves obtained from single-chain simulations with $Z = 6$ and $N_v/N_e = 2.5$ for both the affine deformation case (triangles) and the fluctuating nodes case (circles): comparison between tension-driven (black) and chemical potential-driven (white) monomer sliding dynamics.

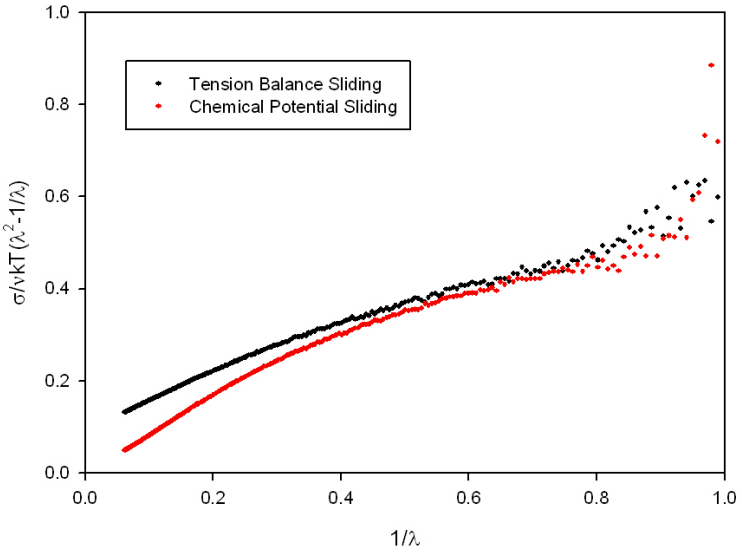

Figure 2.12: Mooney-Rivlin plot of the stress-strain curves obtained from multi-chain simulations of a randomly-crosslinked network with $Z = 10$ and $\phi_c = 0.4$: comparison between tension-driven and chemical potential-driven monomer sliding dynamics.

it does not need to be specified for the simulation. Results in using (2.25) as the monomer sliding equation for the single-chain "toy" simulation and multi-chain simulation of a randomly-crosslinked network are shown in figures 2.11 and 2.12 respectively.

In fig. 2.11, we confront the effects of a different sliding equation on the single-chain "toy" model, both in the case of non-fluctuating nodes (i.e. nodes attached by infinitely stiff virtual springs to the affine background) as well as in the case of fluctuating nodes (i.e. nodes attached by virtual springs with strength comparable to the elastic force of the subchain). In the former case, where the effect of sliding is in isolation, the chemical potential-driven sliding induces significantly more strain softening than the tension-driven sliding. The latter leads to very little, though present, strain softening. However, when coupled with both node fluctuations in space, as in the case of the virtual spring system, the effect of changing the sliding equation is less prominent.

Fig. 2.12 also shows the effect of this modification in the context of the multi-chain simulation discussed previously for randomly-crosslinked networks. The simulation here is done for a Gaussian network so there is continual strain softening at large strains. In this scenario, there is some effect in changing the sliding equation, particularly an increasing slope at behavior large deformations. This is essentially due to the change introduced which modifies the underlying free energy for the model as well as the driving force derived from this free energy. Given the more rigorous nature of the new sliding equation, this is clearly the more correct prediction by the PCN model on the stress-strain behavior. However, this observed change is minor compared to the discrepancy observed for end-linked networks. Hence, this change in dynamics probably will not affect the predictions for the end-linked case drastically, as in the case shown here (for randomly-crosslinked networks). Hence, the reason behind the discrepancy for that particular system still remains a mystery.

On a final note, the importance of this work deserves a few comments. Slip-link simulations or, indeed, many-chain models or treatments of entangled networks are somewhat few in literature. Most theoretical treatments involve a mean-field approach, except for the work of Ball et al. and Edwards and Vilgis using the replica formalism. Other than the molecular dynamics simulations of Grest, Everaers and co-workers [103] and the recent work of Anogiannakis et al. [87], there are also very few other modeling attempts on these systems especially at the level of description slip-links and entanglement strands as with the PCN model. To our knowledge, the only attempt to apply slip-link simulations to the problem of entangled networks has been

in the recent work of Jensen and co-workers [118] where they applied the single-chain discrete slip-link model of Schieber et al. [25] on the elastic behavior of both ideal networks and imperfect networks with dangling ends. However, their work is different from the direction of this current work in the sense that (1) their model is a single-chain model and (2) they considered only the behavior of the networks in the linear range, i.e. at low frequencies, and not at large strains. Since the slip-link models are significantly more coarse-grained than the MD simulations work mentioned, it fills a niche for a simple model that adequately captures the necessary physics for simulation of such systems but at significantly lower computational cost. Hence, the development of the PCN model along these ranks is important in filling this niche. This remaining discrepancy problematized here could also be indicative of some missing ingredients in the basic model formulation, corrections to which might be relevant also for the simulation of more complex systems such as entangled melts and solutions which the PCN model seems to adequately describe, as of the present. This would motivate future work in this direction.

2.4 Conclusions

In this chapter, we have explored the general problem of applying the Primitive Chain Network model in simulating entangled rubbers. This was motivated by the previous work of Oberdisse and co-workers [41, 42] which reported a discrepancy between simulation results and predictions from the well-established replica model of Edwards and Vilgis [101], which has been validated by experimental data. In this case, we have applied the PCN model to the case of randomly-crosslinked networks, which have a distribution of the elastic strand length between crosslinks, as opposed to end-linked networks, where all strand lengths are equal. We found that simulation results in this case are more consistent with the Edwards-Vilgis calculations. Hence, it stands that the PCN model fails only for what is expected to be the simple case of end-linked rubbers.

To improve model predictions for this case, we considered two possibilities on how to eliminate the discrepancy. The first is by introducing disentanglement or entanglement stripping based on the idea of strong and weak entanglements. It was shown however that to capture the full range predicted by Edwards and Vilgis that full disentanglement is necessary, a possibility which seems to be physically implausible. The second is by considering the strain-induced weakening of the confinement potential in the

chain as proposed previously by Rubinstein and Panyukov [105] and demonstrated numerically here using a single-chain "toy model". However, this idea seems to be effective only for models which explicity account for the tube confinement via harmonic potentials such as in the "toy model" considered here as well as in the slip-spring model of Likhtman [27] and the inclusion of this effect is less straightforward for the case of the PCN model where the confinement is by chains acting on other chains, consistent with a many-chain perspective. Hence, this discrepancy for end-linked networks remains an open problem for the PCN model.

We also confronted the thermodynamic inconsistency of the present sliding model as pointed out by Schieber and Horio [93] similar to ideas previously put forward by Greco [117]. A more thermodynamically-consistent monomer exchange equation would be one driven by differences in the chemical potential of the two subchains and we have presented such a sliding equation based on some earlier proposals by Schieber [107]. This sliding equation modifies the strain softening behavior one can observe in the toy single chain model and in the multi-chain model implemented for a randomly-crosslinked network. However, the change is somewhat minor and probably will not significantly modify the model predictions for end-linked networks.

We suspect that the problem could be connected to the method of network preparation used to obtain the starting equilibriated states for simulation. There is a clear difficulty in obtaining this and there are probably some techniques which could be picked up from MD simulations [103]. Likewise, an alternative would be to use networks equilbriated in MD simulations as direct input to the PCN model by doing primitive path analysis [17, 115] to convert the system into a primitive path network. The PCN model could then be used to obtain stress-strain curves for this network for less computational effort. If the results are in better agreement with those obtained from MD simulations or with the predictions with Edwards-Vilgis, clearly the problem is directly connected to network preparation.

Chapter 3

Tube Models for Parallel Superposition Flows

3.1 Introduction

Experiments on superposition flows provide effective means for understanding the nonlinear behavior of viscoelastic materials and for verifying the validity of constitutive models [119, 120, 121]. The idea is to perturb a system that is already experiencing some background flow by superimposing another flow field. This perturbation could be in the form of a small-amplitude oscillatory shear applied either parallel or orthogonal to the flow. These experiments generate a set of *superposition moduli* – nonlinear analogues of the dynamic moduli in linear viscoelasticity which depend on the shear rate. Constitutive equations are then validated by comparing their predictions with data on such spectra [119, 120].

In the context of entangled polymers, developing constitutive equations based on molecular models as basis for viscoelastic behavior [1, 9] could enable the molecular interpretation of results from such experiments. In the case of nonlinear shear flows, the molecular mechanisms that must be accounted for in such models include chain retraction [5, 6], chain stretching [66, 67] and convective constraint release (CCR) [45, 46, 69]. From these mechanisms, molecular constitutive equations that predict the rheological behavior have been developed [71, 80, 73, 81, 122]. In general, these models are quite successful as their predictions compare reasonably with data from rheometry.

For superposition flows, Somma and co-workers report modeling and experiments on polydisperse melts [121]. Their experiments were done in

stress-controlled mode on a polydisperse propylene melt and the modeling of the results was based on a simple tube-based constitutive equation [80]. They observed that the superposition storage modulus was more drastically affected by shear flow while the superposition loss modulus barely changed. Data for both moduli agree with their theoretical model for low to intermediate applied stresses.

Similar work on more narrowly-dispersed systems obtained in strain-controlled mode have also been reported recently by Wang and co-workers [43, 44]. In their experiments on monodisperse and nearly-monodisperse polybutadiene solutions, a new feature emerged which is the dynamic crossover at low frequencies that is observed to shift in flow. In the quiescent state, this crossover frequency is a signature of the terminal relaxation in monodisperse systems and the inverse of this crossover frequency is the effective relaxation time of the system. This relaxation time would be equivalent to the disengagement time τ_D due to both reptation [3] and tube length fluctuations [59]. Wang and co-workers observed that this effective relaxation time shifts universally as a function of shear rate. They then intepreted this as an acceleration of the relaxation of the system due to flow, consistent with the idea of convective constraint release (CCR) [43, 44].

Finally, others present theoretical predictions on the behavior of these superposition moduli in flow using other approaches [123, 124]. Uneyama and co-workers use a generic dynamic model for polymers with an anisotropic mobility tensor and results from linear response theory to derive expressions for the superposition moduli [123]. Mead also presented calculations for these moduli using a polydisperse extension of a tube model with CCR [122] for both parallel and orthogonal superposition cases [124]. Both papers report qualitative agreement with previous experiments though no actual comparisons with data are presented.

In this work, we confront the data from the experiments of Wang and co-workers [43, 44] on narrowly-dispersed polymer solutions using a molecular constitutive equation based on the tube model [80] similar to the approach by [121]. The objectives are two-fold: (1) to validate the approach by Somma and co-workers by analyzing narrowly-dispersed systems and (2) to investigate the role of CCR and other molecular mechanisms in understanding data on superposition flows. In particular, we seek to test the claim of Wang and co-workers that the shifting of the effective relaxation time with flow is consistent with CCR.

This chapter is organized as follows. First, we describe the modeling approach used, particularly the constitutive equation of Marrucci and Ianniruberto [80] and the linear expansion approach to obtain expressions for

the superposition moduli [121]. Then, we compare these results with experimental data by Wang and co-workers on solutions. These results will be discussed in light of the molecular theory used. Finally, a short summary of these findings and future outlook on the problem constitute the conclusions.

3.2 Model Description

3.2.1 Constitutive Equation

To model the experimental data, we use the differential tube-based constitutive equation with CCR [80] proposed by Marrucci and Ianniruberto. While more detailed full-chain models are available, e.g. the integral model of Mead, Larson and Doi [71] or the full-chain nonlinear model of Graham and co-workers [73], the simple form of this differential model lends itself well to perturbation analysis where an analytical expression for the superposition spectra is desired. Despite its simplicity, this equation has a direct correspondence to molecular theory since it was based on tube model ideas.

The Marrrucci-Ianniruberto model has an evolution equation for the tensor $\boldsymbol{A}$ which is defined below as the non-dimensional second moment of the distribution of subchain end-to-end vectors $\boldsymbol{rr}$.

$$\boldsymbol{A} = \frac{\langle \boldsymbol{rr} \rangle}{r_0^2} \tag{3.1}$$

The dynamics of $\boldsymbol{A}$ is then given by the following equation.

$$\frac{d\boldsymbol{A}}{dt} = \boldsymbol{\kappa} \cdot \boldsymbol{A} + \boldsymbol{A} \cdot \boldsymbol{\kappa}^T - \frac{1}{\tau}\left(\boldsymbol{A} - \frac{\mathrm{tr}\boldsymbol{A}}{3}\boldsymbol{I}\right) - \frac{1}{3\tau_R}(\mathrm{tr}\boldsymbol{A} - 1)\boldsymbol{I} \tag{3.2}$$

The equation above contains two relaxation times: τ_R, the Rouse time of the chain which governs stretch relaxation and τ, which governs orientational relaxation and is expressed here as a function of τ_D, the disengagement time of the chain.

$$\frac{1}{\tau} = \frac{2}{\tau_D} + \left(\frac{1}{\tau_R} - \frac{2}{\tau_D}\right)\frac{\beta(\mathrm{tr}\boldsymbol{A} - 1)}{1 + \beta(\mathrm{tr}\boldsymbol{A} - 1)} \tag{3.3}$$

Note that only τ_R and τ_D are constant for a given polymer system, as both are related to the average molecular weight of the chains. Here, τ varies with flow through the convective constraint release mechanism (CCR) [45, 80] as regulated by the parameter β, the so-called CCR parameter. β is

the only nonlinear parameter in this model and is held to be of order unity in previous CCR models [45, 46, 73, 80, 81].

Finally, the stress tensor $\boldsymbol{\sigma}$ can be determined from the second moment of the distribution of subchain end-to-end vectors $\boldsymbol{r}$ and subsequently from $\boldsymbol{A}$ as follows.

$$\boldsymbol{\sigma} = \nu\langle \boldsymbol{F}\boldsymbol{r}\rangle = \frac{3\nu kT}{r_0^2}\langle \boldsymbol{r}\boldsymbol{r}\rangle = 3\nu kT\boldsymbol{A} = G\boldsymbol{A} \tag{3.4}$$

It should be mentioned that this single-mode equation reduces in the linear limit to the Maxwell equation which has a single relaxation time (in this case, the orientation relaxation time). For predictions for real polymeric systems which exhibit a spectrum of relaxation times even in the linear range, it is inevitable that one must use a multi-mode approach which can be done, using the present model, treating the stress as a sum of independent contributions from different modes as follows.

$$\boldsymbol{\sigma} = \sum_i G_i \boldsymbol{A}_i \tag{3.5}$$

In such a multi-mode approach, each relaxation mode would be characterized by two parameters from linear viscoelasticity: G_i, the fractional modulus which gives the weight of the mode contribution, and $\tau_{0,i}$ which is the orientational relaxation time of the mode at equilibrium. Both of these parameters can be obtained by fitting the linear viscoelastic spectrum using several Maxwell modes, easily facilitated by software such as Reptate[1].

Other than these parameters characterizing the linear viscoelastic spectrum and the nonlinear parameter β, one would also need to specify the stretch relaxation time $\tau_{R,i}$. However, this is not an easy task. Hence, for simplicity we assume that in the situations considered here that stretch can be reglected, i.e. $\tau_{R,i} = 0$, and that stress is determined purely by orientation. In reality, this would be the case for monodisperse (or nearly monodisperse) systems with flow rates less than the inverse of the Rouse time τ_R though in general not the case for polydisperse systems.

In this case, (3.2) reduces to the no-stretch version given here as follows

$$\frac{d\boldsymbol{A}_i}{dt} = \boldsymbol{\kappa}\cdot\boldsymbol{A}_i + \boldsymbol{A}_i\cdot\boldsymbol{\kappa}^T - \frac{1}{\tau_i}\left(\boldsymbol{A} - \frac{1}{3}\mathbf{I}\right) - \frac{2}{3}(\boldsymbol{\kappa} : \boldsymbol{A})\boldsymbol{I} \tag{3.6}$$

[1]Reptate: Rheology of Entangled Polymers: Toolkit for Analysis of Theory and Experiment - a free software developed by Jorge Ramirez and Alexei Likhtman. Available online at http://reptate.com

and the orientational relaxation times are given by the expression

$$\frac{1}{\tau_i} = \frac{1}{\tau_{0,i}} + 2\beta\boldsymbol{\kappa} : \mathbf{A}_i \tag{3.7}$$

which is a simplified form of (3.3) and close in form to the original equation proposed by Marrucci for CCR [45]. Other details on this model can be found in the original paper by Marrucci and Ianniruberto [80].

3.2.2 Linear Expansion Approach

Following the previous work [121], we use a linear expansion of the superimposed flow on the constitutive equation to obtain analytical expressions for the superposition moduli. Here, we outline the procedure for doing this in detail. A minor difference between the calculation presented here with respect to the previous case is that we consider strain-imposed measurements while Somma and co-workers used stress-imposed measurements.

The experiment is done by applying a steady shear flow with rate $\dot{\gamma}$ and a small-amplitude oscillatory shear $\gamma_0 \sin \omega t$ with strain amplitude γ_0 and frequency ω on this steady flow. In terms of the velocity gradient tensor $\boldsymbol{\kappa}$, this can be written as follows

$$\boldsymbol{\kappa}_T = \boldsymbol{\kappa} + \boldsymbol{\kappa}_{||} \tag{3.8}$$

where $\boldsymbol{\kappa}$ is the velocity gradient tensor due to the background flow, $\boldsymbol{\kappa}_{||}$ is due to the superimposed flow and $\boldsymbol{\kappa}_T$ is the total velocity gradient tensor. In shear flow, the only non-zero components of these tensors are the xy-components which are related as follows

$$\dot{\gamma_T} = \dot{\gamma} + \gamma_0 \omega \cos(\omega t) \tag{3.9}$$

where $\dot{\gamma}_T$ is the total shear rate from the superposition of the two flows. In terms of the total shear strain, this can be rewritten as follows.

$$\gamma_T(t) = \dot{\gamma} t + \gamma_0 \sin \omega t \tag{3.10}$$

It follows that the stress response to this superimposed flow can be written in terms of two components as well

$$\boldsymbol{\sigma}_T = \boldsymbol{\sigma} + \boldsymbol{\sigma}_{||} \tag{3.11}$$

where $\boldsymbol{\sigma}$ is the stress due to the background flow, $\boldsymbol{\sigma}_{||}$ is the stress due to the superimposed flow and $\boldsymbol{\sigma}_T$ is the total stress. Again, the component of

interest in these tensors would be the xy-component. For $\boldsymbol{\sigma}_{||}$, in the limit of small γ_0, the xy-component can be written in terms of two parts that are in-phase and out-of-phase with the applied oscillatory shear

$$\sigma_{||} = G'_{||}\gamma_0 \sin(\omega t) + G''_{||}\gamma_0 \cos(\omega t) \tag{3.12}$$

where $G'_{||}$ and $G''_{||}$ are the superposition moduli, the quantities of interest.

To obtain the final expressions for the superposition spectra, the definitions for $\boldsymbol{\sigma}_T$ and $\boldsymbol{\kappa}_T$ are combined with the constitutive model given by equation (3.6), which is expressed in terms of the $\mathbf{A}$-tensors.

Return to equation (3.6), the term on the left-hand can be transposed to the right-hand side as follows.

$$0 \;=\; -\frac{d\mathbf{A}_i}{dt} + \boldsymbol{\kappa}\cdot\mathbf{A}_i + \mathbf{A}_i\cdot\boldsymbol{\kappa}^T - \frac{1}{\tau_i}\left(\mathbf{A}_i - \frac{1}{3}\mathbf{I}\right) - \frac{2}{3}(\boldsymbol{\kappa} \;:\; \mathbf{A}_i)\mathbf{I} \tag{3.13}$$

In (3.13), all the terms in the right-hand side are containing various powers of γ_0, the strain amplitude of the superimposed shear. Considering that γ_0 is small, we can assume that all higher-order powers of γ_0 starting from 2 would be very small and have negligible contribution. Hence, we can focus our attention on terms that are linear in γ_0. By letting these terms be equal to 0 and focusing on the xy-component, which contains $G'_{||}$ and $G''_{||}$, we are able to obtain expressions for these superposition moduli in terms of $A'_{||}$ and $A''_{||}$. For brevity, the exact expressions for each mode are presented in Appendix C.

Since, we are considering a multimode approach, we sum the contributions from various modes to obtain the total superposition moduli for the system which is simply

$$G'_{||}(\omega, \dot{\gamma}) = \sum_i G_i A'_{||}(\omega, \tau_i, \dot{\gamma}) \tag{3.14}$$

$$G''_{||}(\omega, \dot{\gamma}) = \sum_i G_i A''_{||}(\omega, \tau_i, \dot{\gamma}) \tag{3.15}$$

where G_i are the fractional moduli that give the weight of each mode.

Expressions (3.14) and (3.15) are then used to compare with experimental data in the following section.

Table 3.1: Material parameters for PBD solutions

	M_w [kg/mol]	PDI	c [wt. %]	τ_D [s]	Z	Data Source
3% PB2.6M	2600	1.625	3%	90.91	29	[44]
5% PB0.7M	750	1.01	5%	29.8	13	[43]
10% PB0.7M	750	1.01	10%	17.7	27	[43]

3.3 Results and Discussion

In this section, we confront the data on polybutadiene solutions from the experiments of Wang and co-workers [43, 44]. The details on these solutions are reported in table 3.1 and the relaxation spectrum obtained by fitting the linear viscoelastic response and used in the multimode calculations are given in Appendix A.

First, we confront the data presented by Li and Wang on a polybutadiene solution with polydispersity of 1.625 [44]. While this system is not narrowly-dispersed, the linear response of the material still shows the dynamic crossover in the low frequency region as shown in the linear viscoelastic response in fig. 3.1. The figure also shows the best fit obtained using Reptate involving 7 relaxation modes. It was observed that the introduction of more modes does not significantly improve the obtained fit.

For the superposition experiment, Li and Wang report the superposition moduli for one shear rate $\dot{\gamma} = 0.04s^{-1}$ where they varied the temperature. Considering only the spectrum at the reference temperature for the linear viscoelastic response, we obtained predictions for these moduli using the analytic expressions obtained from section 3.2.2 shown in fig. 3.2.

Model predictions compare well with the measured superposition moduli for this shear rate as shown in fig. 3.2. The effect of varying the CCR parameter β on the model predictions is found to quite subtle as shown in figure where predictions for $\beta = 0, 0.5$ and 1 are shown to be very similar. The only noticeable effect is near the terminal region of the loss modulus which is slightly affected by β. However, the dynamic crossover, which is the region of interest, is barely altered by varying β.

Li and Wang also report data on the reciprocal of the crossover frequency, taken to be the effective relaxation time of the system, as a function of the shear rate which is plotted in fig. 3.3. They observed that their data for this relaxation time τ_{eff} scales universally with the applied rate $\dot{\gamma}$ with a prefactor of 5, which is also shown in fig. 3.3 as the solid line. Calculations

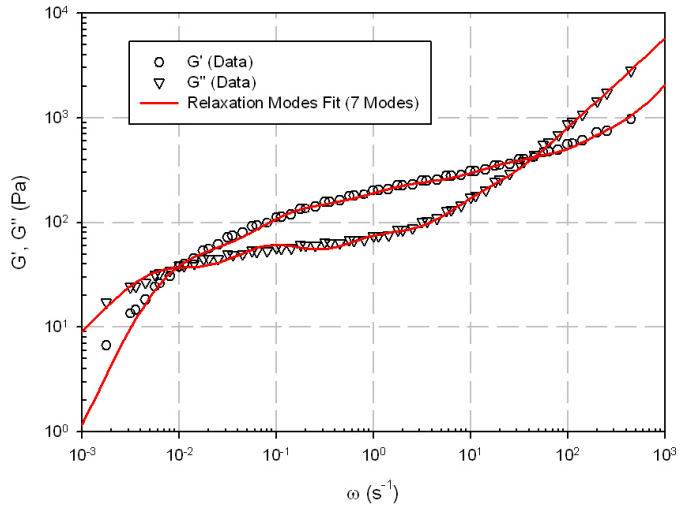

Figure 3.1: Linear viscoelastic response of the 3% PBD solution from the experiments of Li and Wang. Solid curves are fits using multiple Maxwell modes.

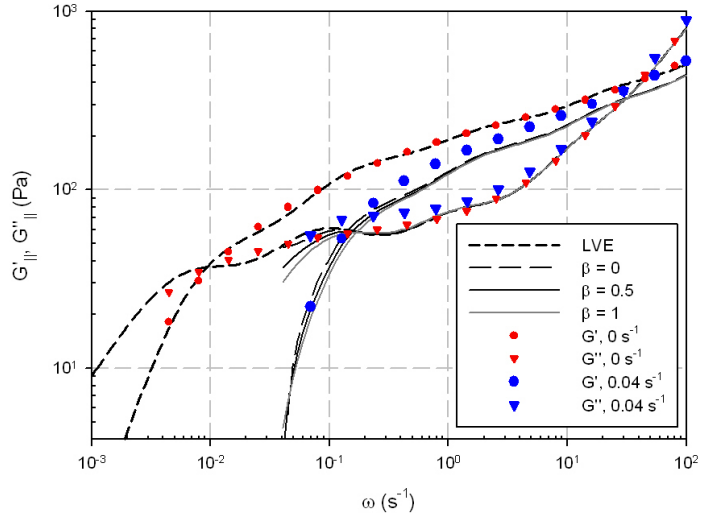

Figure 3.2: Superposition moduli data for the 3% PBD solution of Li-Wang with shear rate of $0.04s^{-1}$ and calculations using various values of β.

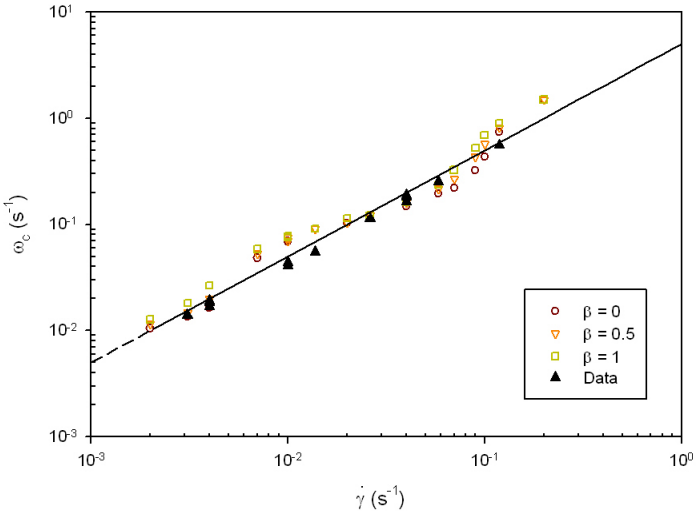

Figure 3.3: Plot of the effective relaxation time vs. shear rate: Open symbols are data by Li and Wang, closed symbols are calculations and the line corresponds to $1/\tau_{\text{eff}} = 5\dot{\gamma}$.

similar to that shown in fig. 3.2 were performed for some of values of the rates they examined and are also plotted in fig. 3.3.

We observe that both data and calculated values for the effective relaxation time follow the empirical scaling they reported as shown in fig. 3.3. However, consistent with fig. 3.2, it was observed that these calculated values were not largely effected by varying the CCR parameter β.

We also considered the more detailed data set reported by Boukany and Wang [43] from similar superposition experiments on monodisperse ultra-high molecular weight polybutadiene solutions (5% and 10% weight fractions). These samples are well-entangled and which have a polydispersity of 1.05, as shown in table 3.1. Their linear viscoelastic response and corresponding curves fitted using relaxation modes are shown in fig. 3.4.

For these samples, Boukany and Wang report both the scaling behavior of the crossover frequency for both solutions as well as the values of the superposition moduli for wider range of shear rates. We confront these data by performing calculations using the analytic expressions obtained for the superposition moduli by linear expansion, discussed in section 3.2.2.

Figures 3.5 and 3.6 show the comparison between the predictions for the

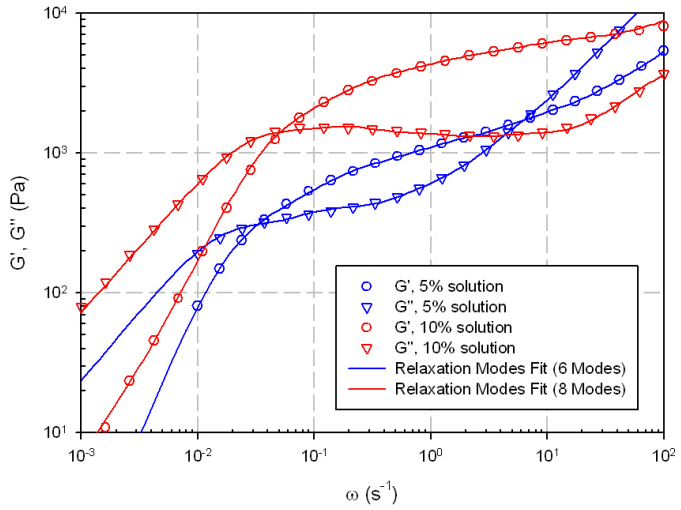

Figure 3.4: Linear viscoelastic response of the 5% and 10% PBD solutions from the experiments of Boukany and Wang. Solid curves are fits using multiple Maxwell modes.

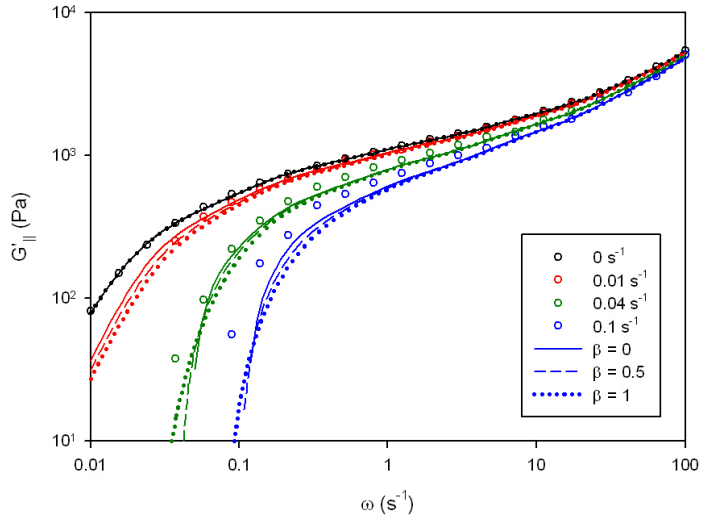

Figure 3.5: Storage modulus calculation for the 5% monodisperse solution of Boukany and Wang

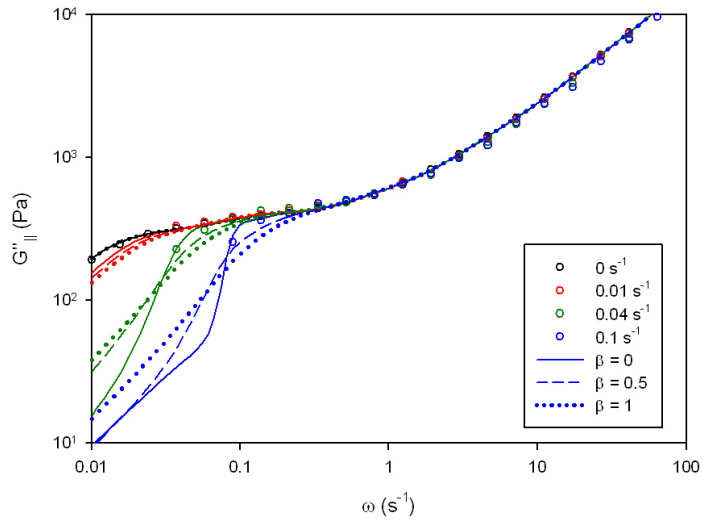

Figure 3.6: Loss modulus calculation for the 5% monodisperse solution of Boukany and Wang

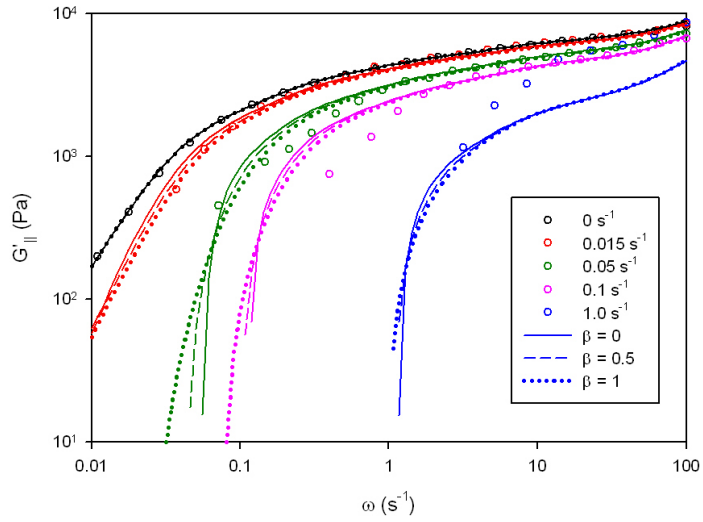

Figure 3.7: Storage modulus calculation for the 10% monodisperse solution of Boukany and Wang

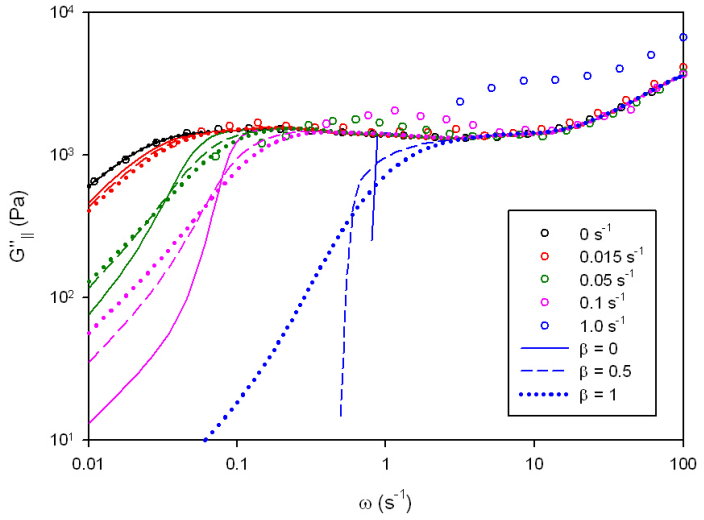

Figure 3.8: Loss modulus calculation for the 10% monodisperse solution of Boukany and Wang

storage and loss moduli for the 5% solution and the data from Boukany and Wang [43]. Here, the previous observation of Somma and co-workers that the effect of shear flow is more drastic on G' than on G'' [121] is verified by both data and calculations. Similarly, as observed previously in calculations for the Li-Wang data, the only effect of shear on the latter is near the terminal region. Both data sets seem to be reasonably described by the model although there is an increasing deviation in the storage modulus predictions at larger rates. The model predictions are also slightly shifted to higher frequencies than the data, an effect that is slightly affected by increasing β. For the case of the loss modulus, the data can also be reasonably captured by the model although the effect of changing β near the terminal region causes some unnatural features for the largest rate at $\beta = 0$ though well outside the what is covered by available data.

For the case of the 10% solution, which is more entangled than the 5% solution ($Z = 27$ vis-a-vis $Z = 13$), model agreement seems less favorable as seen in figures 3.7 and 3.8. For the storage modulus, there is increasing discrepancy with the data at larger rates, as in the 5% solution, but as this data set accesses much larger rates (up to $\dot{\gamma} = 1.0$), more features of this discrepancy are identified. For instance, the discrepancy for the second

largest rate $\dot{\gamma} = 0.1$ is only for the terminal region and the data is somewhat more shifted to high frequencies than the model prediction. For this rate, the model still captures the plateau region. However, this is not the case for the largest rate $\dot{\gamma} = 1.0$. For this rate, the calculations using the model hardly fit the data at all and the plateau predicted is much lower than the plateau exhibited by the data. Note that this discrepancy is not affected by the choice of CCR parameter whose effect is again observed to be quite minimal.

For the loss modulus, the model fails to fit the data quantitatively especially at larger rates similar to the case of the storage modulus. For the 10% solution, in contrast with the previous systems examined, experimental data for the loss moduli don't fully superimpose at large frequencies, especially for the two largest rates. The theoretical calculations, on the other hand, superimpose at large frequencies but, expectedly, not near the terminal region. This discrepancy, which is most drastic for the largest rate $\dot{\gamma} = 1.0$, is again irrespective of β which has some effect only near the terminal region.

In figures 3.9 and 3.10, both the storage and loss moduli predictions ($\beta = 1$) and data are shown to highlight the effects of CCR and shear on the dynamic crossover. For the 5% solution (fig. 3.9), data agreement with the theoretical calculations seems reasonable, except for the largest rate ($\dot{\gamma} = 0.1$). In closer inspection, the theoretical predictions for this rate come close but actually do not intersect. As the experimental data for this rate does show the actual crossover (as well as the second crossover at higher frequencies), this feature could be limitation of the current approach where stretch is not considered and the stretch relaxation time, τ_R, is set to 0. For this particular rate, owing to the need to obtain an effective relaxation time, we define the crossover frequency as the frequency where the difference between G' and G" is at a minimum (i.e. where the two curves almost intersect).

It should be mentioned that, while the feature of non-intersecting G' and G" may seem unphysical, such profiles have been observed experimentally by Boukany and Wang in superposition flows of DNA solutions, though at very large rates [43]. These have been reported in the same paper as the polybutadiene solutions data though we have not analyzed the data set on DNA since they are known to exhibit shear banding or non-homogeneous velocity profiles [43]. While, Boukany and Wang report that the presence of banded profiles do not affect the superposition flow behavior, we contend that the non-homogeneity of the velocity field would make any direct or straightforward constitutive analysis of those data less valid.

For the case of the 10% solution, as shown in fig. 3.10, it was already

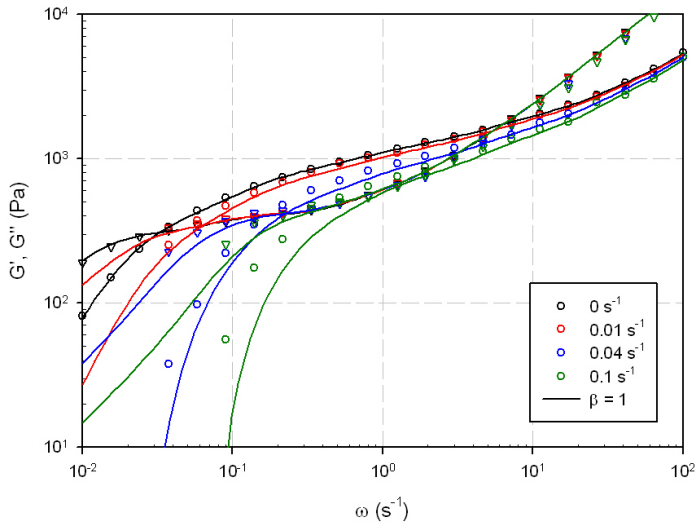

Figure 3.9: Superposition moduli calculations for the 5% monodisperse solution: Open symbols are data, curves are calculations for $\beta = 1$.

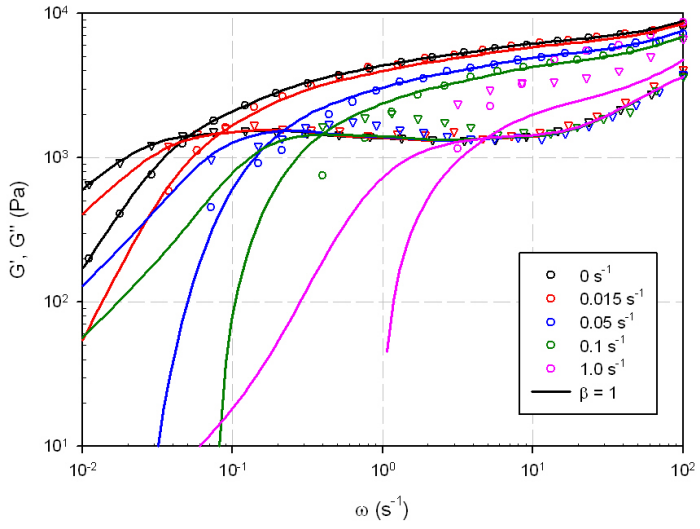

Figure 3.10: Superposition moduli calculations for the 10% monodisperse solution: Open symbols are data, curves are calculations for $\beta = 1$.

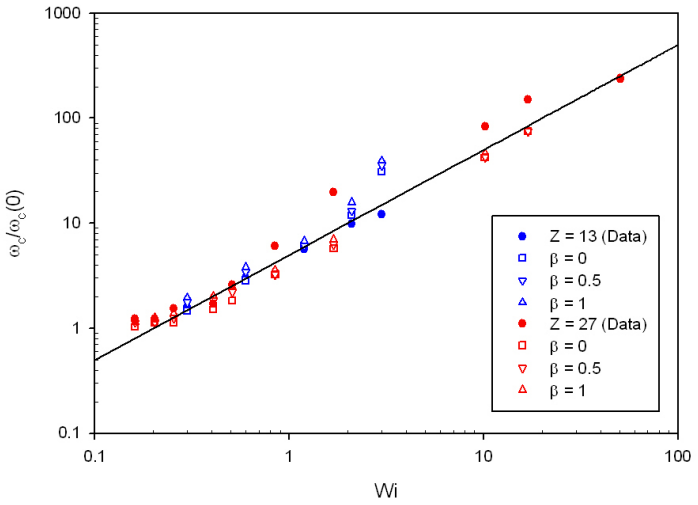

Figure 3.11: Plot of the relative crossover frequency as a function of the terminal relaxation time Weissenberg number (Wi = $\dot{\gamma}\tau$): Closed symbols are data for the 5% and 10% solutions by Boukany and Wang, labeled Z = 13 and Z = 27, respectively, open symbols are calculations and the line corresponds to $1/\tau_{\text{eff}} = 5\dot{\gamma}$.

pointed out that the model fails drastically in fitting the data for the superposition moduli in at the largest rate and this is apparent in the figure. Meanwhile, the crossover seems to be reasonably captured at the lower rates. This increase in the level of the loss modulus at high frequencies could be indicative of stretching which we have neglected in the model on purpose to keep the expressions simple and to be able to derive an analytical expression for the moduli. The inclusion of stretch in the model could introduce two difficulties: the first is in obtaining an analytical solution, though an alternative would be a numerical solution of the equations, and the second is in obtaining a stretch relaxation time for each mode, which is not straightforward.

Despite these difficulties in obtaining quantitative agreement with the data on superposition moduli for both 5% and 10% solutions, it still seems worthwhile to understand the relative scaling of the effective relaxation time with the shear rate which we show here in fig. 3.11. We plot the crossover frequency normalized by the crossover frequency without flow versus the terminal relaxation time Weissenberg number ($\dot{\gamma}\tau$). We report both data

and calculations as well as the empirical scaling $1/\tau_{\text{eff}} = 5\dot{\gamma}$, as reported by Li and Wang [44], as a straight line in fig. 3.11.

It could be observed in fig. 3.11 that the model, in general, underestimates the crossover frequency compared to the data at larger rates ($Wi > 1$), particularly for the more entangled case (the 10% solution), though this seems to be irrespective of inclusion (or non-inclusion) of CCR, which is known to be important in this regime. The discrepancy, of course, could be traced back to the detailed analysis of the superposition moduli made earlier regarding the difficulty of including stretch in this simple approach.

Indeed stretch could be important, for example, in the largest rate considered for the 10% solution ($\dot{\gamma} = 1.0$) which has a terminal relaxation time $\tau_D = 17.7$. This disengagement time is not equivalent to the reptation τ_{rept} time but is shorter due to contour length fluctuations. However, if we take this to be the reptation time, keeping in mind that the actual reptation time is longer, and recalling an approximate relationship between the Rouse and reptation times as follows $\tau_{\text{rept}}/\tau_R \approx 3Z$, we can then estimate that the Rouse time is at least 0.21. This would make the critical rate for stretching to be $\dot{\gamma} \leq 4.58$ which is of the same order of magnitude as the rate in the largest case. It is then strongly likely that stretching effects could be important.

It should also be mentioned that most predictions and data for all the monodisperse systems considered here, as shown in fig. 3.12, roughly form a mastercurve along the line correponding to the empirical scaling pointed out by Wang and co-workers [43, 44]. The agreement with this relation, however, should not be taken as validation of the model, for purposes already mentioned earlier during the confrontation of the superposition moduli. It has been shown that some data points especially at large rates actually severely underestimate the crossover and calculations do not always reasonably capture the data for superposition moduli.

Lastly, we comment on the main molecular mechanism responsible for the effective shifting of the superposition moduli in flow. Regarding this, Wang and co-workers claim that the effective shifting observed is a signature of convective constraint release (CCR) [43, 44]. The concept of CCR, as proposed previously by [45], posits that the effective relaxation time of the entangled system in flow is smaller than its relaxation time at equilibrium due to the convective release of some entanglements in flow. This acceleration of the relaxation of the system due to flow can be expressed simply as follows

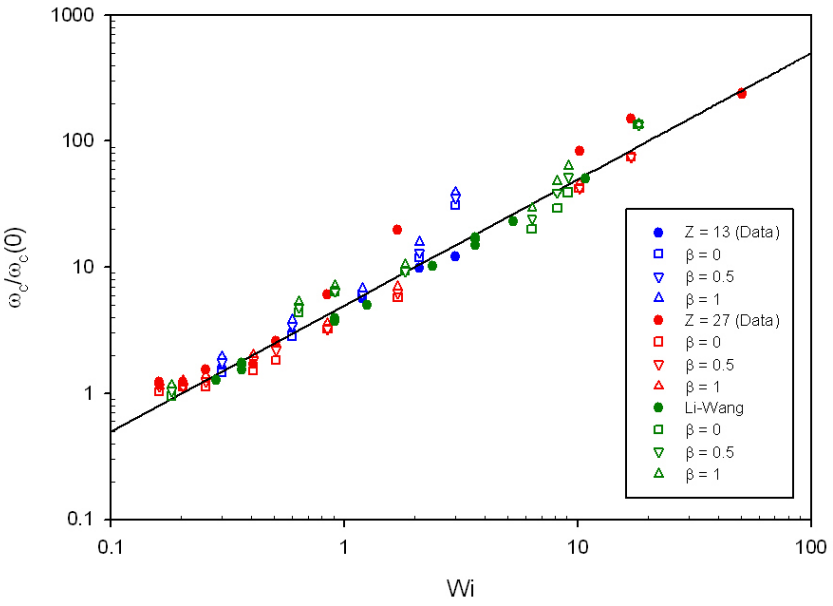

Figure 3.12: Master curve of the relative crossover frequency as a function of the Weissenberg number ($\dot{\gamma}\tau$) for the monodisperse solutions investigated: closed symbols correspond to data, open symbols correspond to calculations while the line corresponds to $1/\tau_{\text{eff}} = 5\dot{\gamma}$.

$$\frac{1}{\tau_{\text{eff}}} = \frac{1}{\tau_0} + \beta\dot{\gamma} \tag{3.16}$$

based on the first CCR paper of [45]. Here, β is the parameter regulating the effectiveness of CCR as a relaxation mechanism.

With equation (3.16) in mind, it is tempting to assume that the universal scaling of the reciprocal of the relaxation time with the shear rate observed experimentally by Wang and co-workers is consistent with this equation and take $\beta = 5$ as the prefactor shown by the experiment. This view, however, is oversimplified as shown here in our analysis of their data. We demonstrated reasonable model agreement with the data for a range of rates independent of the choice made for β. In most cases, choosing $\beta = 0$, which corresponds to no CCR in the model, could still reasonably fit the experimental data as the effect of varying β is mostly on the behavior around the terminal region. Hence, based on what is left in the model, we claim that this effective shifting of the superposition moduli and the dynamic crossover is simply due to *orientation* of the melt along the shear direction and is not connected strongly to CCR, opposite to the claim of Wang and co-workers.

It is easy to see how orientation due to flow gives rise to an effective loss of elasticity, as observed in the shifting of $G'_{||}$, when the mechanism of chain retraction is considered [5, 6]. During flow, tube segments along the shearing direction are deformed affinely. In the regime of non-stretching flows, retraction of the chain from its deformed state along the tube occurs to preserve the tube length. This would give rise to an effective loss of entanglements (and longer effective tube segments) which corresponds to less elastic objects in the system.

Recently, Mead also identified orientation as one of two effective physical mechanisms in superposition flows [124] from an analysis of the predictions of a single-mode constitutive equation [122]. The other mechanism is the cut-off of the long timescale portion of the relaxation spectrum by flow [124]. Mead attributes this cut-off to CCR which is observed to be relevant in the behavior of a single relaxation mode. However, in the multimode analysis we presented here, we note that some of the slow modes indeed shift with flow while other fast modes do not. Ultimately, the dynamic crossover observed in flow arises from the intersection of the storage and loss superposition moduli which are obtained by summing over various modes (some of which shift while some do not) and we find that CCR is less relevant in this multimode context.

In general, the idea of convective constraint release is still not fully understood given that the effect still introduces an *adjustable parameter* in

nonlinear models. Indeed, to an extent, β is an important parameter in nonlinear rheology, more so in light of recent findings on shear banding and other unusual phenomena [35, 36, 37] by Wang and co-workers. These findings prompt them to propose the possibility of the breakdown of the Doi-Edwards tube picture in nonlinear flows [38]. The alternative perspective to this, however, would be to consider those findings within the tube framework, where CCR is an important mechanism, to understand which situations could be captured reasonably [125, 126]. In most of these calculations, β is an important parameter as it regulates the stability of the resulting flow curve. Some of the phenomena reported by Wang and co-workers could indeed be captured by the Doi-Edwards theory if there is a certain degree of instability inherent in the system as shown in literature [125, 126]. However, while motivational, these topics are beyond the scope of this work.

3.4 Conclusions

In this chapter, we confronted some recent experiments done on parallel superposition flows by Wang and co-workers [43, 44] on monodisperse and nearly-monodisperse polybutadiene solutions. Based on the previous approach of Somma and co-workers [121], we confronted the data using a simple tube-based constitutive equation with convective constraint release (CCR) developed previously by Marrucci and Ianniruberto [80]. Using a linear expansion approach on this simple constitutive equation allows the derivation of analytical expressions for the superposition moduli, nonlinear analogues of the storage and loss moduli for linear viscoelasticity. These expressions can then be compared with the data.

In comparing with the experimental data by Wang and co-workers, we observed that the effect of shear flow is more drastic on the storage modulus than in the loss modulus, where the only effect of flow on the latter is near the terminal regime. This has also been observed previously by Somma and co-workers in polydisperse melts. However, the real novelty of doing the experiments in monodisperse systems, is the observation of the dynamic crossover of the superposition moduli which is effectively shifted in flow [43, 44]. Measure data on this shifting, as reported by Wang and co-workers, empirically follows the trend $1/\tau_{\text{eff}} \sim 5\dot{\gamma}$ where τ_{eff} is the reciprocal of the frequency where the crossover occurs.

Model agreement with the measurements is quite reasonable given the simplicity of the approach but only up to intermediate rates. Predictions

were also observed to be largely independent of the choice for β, which governs the effectiveness of CCR in the model. The former point is important as chain stretching could be a crucial effect at larger flow rates, close to the inverse of the Rouse time for the system. The latter point is important as well as it invalidates the previous claim of Wang and co-workers that the observed shifting of the relaxation time is due to CCR.

Indeed, while CCR is an attractive candidate for rationalizing the experiments, such a view is oversimplified given that the choice of $\beta = 0$ in the present model can still reasonably capture, to some extent, this crossover behavior. Hence, we contend that the observed shifting of the superposition moduli and the dynamic crossover is due simply to *orientation* of the melt in flow and not due to CCR. At large rates, stretch could be important and, indeed, it could be this combination of stretch and orientation which governs the data in such rates. However we posit that disentanglement in flow by CCR or related ideas remain less valid as molecular mechanisms for rationalizing these data from superposition experiments.

Chapter 4

Simple Tube Models for Nonlinear Rheology with Monomer Friction Reduction

4.1 Introduction

Recent improvements of rheological methods enable the examination of tube model predictions for nonlinear viscoelasticity. For the case of extensional flows, advances in filament stretching rheometry generated reliable though somewhat controversial data on both the start-up and steady response of entangled linear polystyrene (PS) solutions [127, 128] and melts [129, 130] with narrow molecular weight distribution.

Contrary to expectations from tube models with chain stretch [66, 71, 72, 73], the data sets show qualitatively different behavior for solutions and melts. Sridhar and co-workers measured the extensional viscosity $\eta_{\rm el}$ of concentrated PS solutions using this filament stretching technique. Their data showed a clear upturn for rates larger than the inverse Rouse time (τ_R) of the polymer [127, 128]. Meanwhile, measurements by Hassager and co-workers on PS melts showed no evidence of this upturn [129]. They also found that for rates between the inverse disengagement time (τ_D) and the inverse Rouse time (τ_R) where orientational relaxation is effectively frozen that $\eta_{\rm el}$ for the PS melts showed a scaling with the elongational rate $\dot{\epsilon}$ with the power of –1/2 rather than –1 as expected from tube models [129]. Extensional measurements on similar PS melts using a different technique also confirm this behavior [131]. These remarkable findings have lead some to question if there are fundamental rheological differences between melts

and solutions which are expected to behave similarly [32, 33].

Considering this data set on monodisperse PS melts, Marrucci and Ianniruberto proposed the *interchain/intertube pressure effect* (ICP) as an additional relaxation mechanism for tube models to remove the discrepancy between the model and experiments [132]. The model predicts the observed –1/2 scaling of the extensional viscosity with the extensional rate and introduces another characteristic time, the tube diameter relaxation time (τ_A). The inclusion of this effect on a tube-based constitutive model, such as the molecular stress function (MSF) model, as done by Wagner and co-workers allowed a satisfactory description of the PS melt data [133]. However, one shortcoming of this idea was revealed when extensional data on bidisperse PS melts emerged, again from filament stretching [130]. This new data set could still be reasonably described by tube-based models including the tube pressure effect but not without seemingly arbitrary adjustments of τ_A [134, 135]. The other shortcoming, which is possibly more significant, is that it fails to distinguish between the different behavior of melts and solutions. To put it in another way, it is still unclear why the tube pressure effect is needed in modeling the data for melts but not for solutions.

Recently, an alternative explanation has emerged also from the original proponents of the ICP [47] based on the idea of flow-induced monomeric friction reduction (MFR). This effect has a long history in rheology [136, 137] but has not been considered within the framework the tube model. The proponents argue that the assumption of a constant monomeric friction (ζ), i.e. its value remaining close to its value at equilibrium (ζ_0), is valid only when the flow is not strong enough to change the molecular environment of a monomer (in this case, a Kuhn segment). In the context of entangled polymers, this is the case for polymer melts in flows faster than the orientation relaxation/disengagement time (τ_D) but slower than the stretch relaxation/Rouse time (τ_R). In this case, the chain structure at the length scale of a Kuhn segment remains isotropic and it is only the global chain structure that is perturbed. However, for flows faster than the stretch relaxation time, the environment at the scale of a Kuhn segment no longer remains isotropic as the segments start aligning. Hence, there could be some deviation of the monomeric friction from its equilibrium value. In polymer solutions, where the environment of the subchain consists of solvent molecules which remain isotropic even at fast flows, this monomeric friction reduction should be absent and ζ remains at the equilibrium value.

Yaoita and co-workers [98, 99] explore this idea further by extracting the reduction from stress relaxation data of a monodisperse PS melt [138]. Then, they included this friction reduction effect in slip-link simulations of entan-

gled polymers under elongation, yielding predictions in semi-quantitative agreement with the data on monodisperse PS solutions [127] and melts [129]. In a later paper, Ianniruberto and co-workers extract the dependence of the monomeric friction with a sufficiently defined order parameter ($\mathcal{S}$) from stress-optical data on monodisperse PS melts [131]. The mathematical form of this behavior was also confirmed by conducting non-equilibrium molecular dynamics (NEMD) simulations on PS oligomers in fast shear flows [85].

In this work, we show that the inclusion of monomeric friction reduction in simple tube-based constitutive models allows reasonable description of the elongational rheology data on monodisperse PS melts and solutions [127, 129, 130], similar to what has been shown by Yaoita and co-workers, albeit using more detailed slip-link simulations in their case [98, 99]. Further, using the same modeling approach, we also fit data on nonlinear shear flows of PS melts [51, 139]. Finally, to further validate the model, we consider data on the stress relaxation of a PS melt after cessation of flow from the work of Nielsen and co-workers [138].

This chapter is organized as follows. In the section on theory, we discuss the modeling approach based on the simple tube-based constitutive equations that will be used and the description of the order parameter dependence of the monomeric friction presented in previous papers [85, 99]. Then, we compare the resulting predictions of the models with the corresponding data on solutions and melts. These will be discussed in light of the underlying molecular theory. Some final remarks and an outlook on future work constitute the last part of the chapter.

4.2 Model Description

4.2.1 Constitutive Equations based on Tube Theory

To predict the nonlinear rheology for the entangled systems, we use two simple tube-based constitutive models: the Mead-Larson-Doi (MLD) model [71], which has an integral equation for the orientation, and the differential approximation by Ianniruberto and Marrucci (IM) [72, 79].

Mead-Larson-Doi Model The MLD model considers the effects of chain retraction [5, 6], chain stretch [66, 67] and convective constraint release (CCR) [45, 46] on the stress in fast flows. The model is formulated by assuming a decoupling of stretch (denoted by the scalar quantity λ) with orientation (represented by the tensor $\mathbf{S}$) [71]. It is composed of a general

expression for the stress $\boldsymbol{\sigma}$ in terms of λ and $\mathbf{S}$ and their corresponding evolution equations shown here

$$\boldsymbol{\sigma} = \frac{15}{4} G_N^0 \lambda^2 \mathbf{S} \tag{4.1}$$

$$\mathbf{S}(t) = \int_{-\infty}^{t} dt' \, \frac{\partial P(t,t')}{\partial t} \, \mathbf{Q}\left[\mathbf{E}(t,t')\right] \tag{4.2}$$

$$\frac{\partial P(t,t')}{\partial t} = -\left[\frac{1}{\tau_D} + \beta\left(\boldsymbol{\kappa}\colon \mathbf{S} - \frac{\dot{\lambda}}{\lambda}\right)\right] P \tag{4.3}$$

$$\dot{\lambda} = \lambda\, \boldsymbol{\kappa}\colon \mathbf{S} - \left[\frac{1}{\tau_R} + \beta\left(\boldsymbol{\kappa}\colon \mathbf{S} - \frac{\dot{\lambda}}{\lambda}\right)\right](\lambda - 1) \tag{4.4}$$

In (4.2), $P(t)$ is the fraction of tube segments that remain oriented at time t, the tensor $\mathbf{Q}[\mathbf{E}(t,t')]$ is the classic Doi-Edwards tensor [1, 5, 6] while the tensor $\boldsymbol{\kappa}$ in (4.3) and (4.4) is the deformation gradient tensor.

Note that the expressions for $\mathbf{Q}[\mathbf{E}(t,t')]$ in elongation and shear given in the original Doi-Edwards papers [5, 6] are obtained by invoking the *independent alignment approximation* (IAA). For expressions for $\mathbf{Q}[\mathbf{E}(t,t')]$ without the IAA, we use the expression reported by Marrucci and de Cindio [140] for the case of extensional flows. Note that this choice for $\mathbf{Q}$ also affects the prefactor in the stress expression (4.1) which is 5 for the case invoking IAA and 15/4 without IAA.

The time constants τ_D and τ_R correspond to the *disengagement time* and the *Rouse time* respectively. The former governs orientational dynamics, given by equations (4.2) and (4.3), while the latter governs stretch dynamics, given by equation (4.4). Both are constants for a given material. Hence, the only parameter in the model is β, which regulates the effectiveness of CCR as a relaxation mechanism. In the original MLD paper [71], this is assumed to be 0.5 in (4.4) while replaced by a switch function in (4.3). Note that since β appears in both orientation and stretch equations, CCR in this model is assumed to affect both dynamics.

It should be mentioned that equation (4.3) is different from the original evolution equation for $P(t)$ owing to some simplifications assumed here. Other than the replacement of the switch function by β, the orientation relaxation time in (4.3) is simply τ_D while this is given by $\lambda^2\tau_D$ in the original model [71]. Here, we assume that stretch has no effect on increasing this relaxation time.

The above set of equations can also be extended to a multimode version which should be used when dealing with real polymer systems which exhibit a spectrum of relaxation times. In such an approach, one considers several modes for orientational relaxation (each represented by an orientation tensor $\mathbf{S}_i$) while only considering, for convenience, a single mode for the stretch. When also considering finite-extensibility, which is important in extensional flows at very large rates, the stress expression (4.1) then becomes

$$\boldsymbol{\sigma} = \frac{15}{4} f(\lambda)\lambda^2 \sum_i G_i \mathbf{S}_i \tag{4.5}$$

where $f(\lambda)$ is the finite-extensibility factor to be defined later and G_i is the weight of each orientation tensor $\mathbf{S}_i$. Each mode for the orientation will obey the following equation, equivalent to (4.2)

$$\mathbf{S}_i(t) = \int_{-\infty}^{t} dt' \, \frac{\partial P_i(t,t')}{\partial t} \, \mathbf{Q}\left[\mathbf{E}(t,t')\right] \tag{4.6}$$

where the quantity P_i obeys an equation analogous to (4.3), as with the stretch λ to (4.4).

$$\frac{\partial P_i(t,t')}{\partial t} = -\left[\frac{1}{\tau_i} + \beta\left(\boldsymbol{\kappa} : \overline{\mathbf{S}} - \frac{\dot{\lambda}}{\lambda}\right)\right] P_i \tag{4.7}$$

$$\dot{\lambda} = \lambda\, \boldsymbol{\kappa} : \overline{\mathbf{S}} - \left[\frac{1}{\tau_R} + \beta\left(\boldsymbol{\kappa} : \overline{\mathbf{S}} - \frac{\dot{\lambda}}{\lambda}\right)\right] (f(\lambda)\lambda - f_{eq}) \tag{4.8}$$

Notce that an additional orientation tensor $\overline{\mathbf{S}}$, here referred to as the average orientation tensor, appears in the term containing β in both (4.7) and (4.8). This means that the acceleration of relaxation brought about by CCR applies only on the global or average orientational relaxation and not on the relaxation of each mode. This tensor evolves following (4.6) similar to a "regular" orientation tensor for a relaxation mode but with a relaxation time defined as the average relaxation time $\overline{\tau}$ as follows.

$$\overline{\tau} = \frac{\sum_i G_i \tau_i^2}{\sum_i G_i \tau_i} \tag{4.9}$$

Finally, there is the finite-extensibility factor $f(\lambda)$ that accounts for the departure of the entropic force from Gaussian behavior due to the finite number of monomers in the chain segments. This correction imposes a limit

on the stretching of the chains ($\lambda_{\max}$) and is defined in terms of the inverse Langevin function $\mathcal{L}^{-1}$ as follows.

$$f(\lambda) = \frac{a}{3\lambda b}\mathcal{L}^{-1}(\frac{\lambda b}{a}) \tag{4.10}$$

This factor enters both the stretch equation (4.8) as well as the final expression for the stress (4.5).

Ianniruberto-Marrucci Model Owing to the difficulty of using integral models in some situations, we consider a differential approximation to the evolution of the orientation tensor such as that presented by Ianniruberto and Marrucci (IM) [72, 79].

Still assuming a decoupled representation of stretch and orientation and including finite-extensibility, the stress can be written as follows.

$$\boldsymbol{\sigma} = 6f(\lambda)\lambda^2 \sum_i G_i \mathbf{S}_i \tag{4.11}$$

Here, λ obeys equation (4.8) as in the MLD model while $\mathbf{S}_i$ obeys the following differential equation.

$$\mathbf{S}_i \cdot \dot{\mathbf{S}}_i + \dot{\mathbf{S}}_i \cdot \mathbf{S}_i = \boldsymbol{\kappa} \cdot \mathbf{S}_i^2 + \mathbf{S}_i^2 \cdot \boldsymbol{\kappa}^T - 2\mathbf{S}_i^2 \, \boldsymbol{\kappa} : \mathbf{S}_i - \frac{2}{\tau_i}\mathbf{S}_i \cdot \left(\mathbf{S}_i - \frac{1}{3}\mathbf{I}\right) \tag{4.12}$$

Note that τ_i in this model corresponds to the effective characteristic time, as affected by CCR, and not the actual characteristic time for each mode $\tau_{0,i}$, and is defined as follows

$$\frac{1}{\tau_i} = \frac{1}{\tau_{0,i}} + \beta \left(\boldsymbol{\kappa} : \overline{\mathbf{S}} - \frac{\dot{\lambda}}{\lambda}\right) \tag{4.13}$$

where $\overline{\mathbf{S}}$ is again the average orientation tensor characterized by the average relaxation time $\overline{\tau}$, defined by eq. (4.9) and discussed in the previous section. This tensor also evolves using equation (4.12)

It should also be mentioned that equation (4.12) was derived based on the assumption of a strain measure $\tilde{\mathbf{Q}}$ different from the Doi-Edwards $\mathbf{Q}$-tensor. This new tensor is defined as

$$\tilde{\mathbf{Q}} = \frac{\mathbf{C}^{-1/2}}{\mathrm{Tr}(\mathbf{C}^{-1/2})} \tag{4.14}$$

where $\mathbf{C}$ is the Finger tensor. This strain measure was proposed by Marrucci and co-workers based on arguments on local force balance in the entanglements [109, 141]. This choice also introduces the prefactor 6 in the stress expression (4.11), different from the prefactor in the previous expression (but giving rise to the same stress in the linear limit).

In the succeeding sections, we use both the MLD and IM equations in predicting the steady-state elongational viscosity for the PS melts in consideration but only the IM equation for building the start-up response for elongation, shear and stress relaxation as well as in modeling PS solutions.

4.2.2 Order Parameter-Dependence of the Monomeric Friction

As mentioned in the introduction, Ianniruberto and co-workers propose that monomeric friction reduction (MFR) occurs when there is change in the environment of the monomer from isotropic to anisotropic, i.e. when other monomers start to align. In the framework of the tube model, this would occur when the chain is both oriented and stretched significantly. Orientation corresponds to the alignment of tube segments while stretch corresponds to alignment of subchain segments in scales lower than that of a tube segment. Both are required to generate an anisotropic environment for the monomer.

In other forms of soft matter such as liquid crystals, alignment is typically described by an *order parameter* [1]. In the context of the tube model, it is clear that the order parameter should be expressed in terms of both stretch (λ) and orientation ($\mathbf{S}$) as these are the main dynamical variables. Following Yaoita and co-workers [99], we define this order parameter, $\mathcal{S}$, as follows

$$\mathcal{S} = \tilde{\lambda}^2 \overline{S} \tag{4.15}$$

where $\tilde{\lambda}$ is the normalized stretch given by the ratio λ/λ_{max} while $\overline{S}$ is the orientational anisotropy of the components. For solutions, this is given by $\phi_P S_P$ where ϕ_P is the polymer volume fraction while this is simply by S_P for melts (since the $\phi_P = 1$). S_P can then be obtained from the eigenvalues of the orientation tensor, $\mathbf{uu} = \mathbf{RR}/{R_0}^2$, where $\mathbf{R}$ is the chain end-to-end vector. For elongational flows, this is

$$S_P = u_x^2 - u_y^2 \tag{4.16}$$

where x and y denote the components parallel and perpendicular to the stretching direction. For shear flows, this is

$$S_P = \sqrt{(u_x^2 - u_y^2)^2 + 4(u_x u_y)^2} \tag{4.17}$$

where x and y are the shear and gradient directions.

Given the order parameter $\mathcal{S}$, one then needs the dependence of the monomeric friction ζ on this quantity for incorporation in molecular models. This has been obtained from assumed rheological signatures of MFR in previous work: the acceleration of stress relaxation after cessation of elongational flow in entangled PS melts [138] in the paper of Yaoita et al. [99] and the departure from the stress-optic law during the elongation of PS melts [131] in the work of Ianniruberto and co-workers [85]. Following certain assumptions, the latter analysis yields the following power law dependence of ζ with $\mathcal{S}$ after a minimum value $\mathcal{S} = 0.063$ has been reached, before which the value of ζ is the same as in equilibrium.

$$\frac{\zeta}{\zeta_0} = 0.0097\mathcal{S}^{-1.64} \tag{4.18}$$

This form is simpler than the expression obtained by Yaoita et al. and predicts a steeper dependence of the monomer friction reduction with the order parameter [85]. This mathematical form has also been confirmed by atomistic simulations conducted by Ianniruberto and co-workers on PS oligomers in nonlinear shear [85] which seems to give an even steeper dependence that approaches this power law (4.18) for longer oligomers. The stress-relaxation data used by Yaoita et al. [99] also suffers from poor-resolution of the small-timescale behavior which results in the underprediction of the friction reduction [85]. Hence, we choose to include this version of the monomer friction in the tube models which is done by modifying all the characteristic times in the model as follows

$$\frac{\tau}{\tau_0} = \frac{\zeta}{\zeta_0} \tag{4.19}$$

where τ is an effective or shifted characteristic time due to MFR from its equilibrium value τ_0. This corresponds to an effective acceleration of all physical relaxation processes due to the reduction of the basic monomeric friction.

Note that our present treatment of this effect assumes an isotropic reduction in the basic monomer friction in all the relaxation processes. In reality, the change in monomer diffusivity (or monomer friction) is in fact anisotropic, as seen in atomistic simulations [85]. Indeed, the physics of this new effect we are introducing is much more complicated than what is given

Table 4.1: Material parameters for PS melts considered

	M_w [kg/mol]	PDI	τ_R [s]	τ_D [s]	T_{ref} [K]	Data Source
50k	51.7	1.03	6.4	5.0	403	[130]
100k	102.8	1.02	22.9	94	403	[130]
200k	200	1.04	91.5	961	403	[129]
390k	390	1.06	329	11351	403	[129]
145k	145	1.03	1160.58	14000	393	[138]
200k	200	1.06	0.091	1.33	448	[139]
182k	182.1	1.03	0.0423	0.21	453	[51]

Table 4.2: Material parameters for PS solutions considered

	M_w [Mg/mol]	PDI	c [wt. %]	τ_R [s]	τ_D [s]	Z	T_{ref} [K]	Source
7.35% 3.9M	3.9	1.05	7.35%	0.27	1.20	14.8	294	[127]
10% 3.9M	3.9	1.05	10.0%	0.28	4.10	27.4	294	[127]

here in our current treatment. However, as a first attempt to introduce this modification, we restrict our attention to the isotropic modification of the relaxation processes. The modifications used in the slip-link simulations of Yaoita et al. followed a simialr spirit [99].

In the following section, we present the results of including this effect in the tube-based constitutive equations discussed in the previous section.

4.3 Results and Discussion

4.3.1 Linear Viscoelasticity and Material Parameters

We report the material parameters for the various PS melts and solutions considered in tables 4.1 and 4.2 respectively. The molecular weight, polydispersity and reference temperatures for the experiment done are taken from the corresponding papers while the relaxation times reported here deserve further comment.

The terminal relaxation time τ_D can be obtained directly from linear viscoelasticity and it corresponds to the reciprocal of the frequency in the first cross-over point of G' and G'' [113]. Meanwhile, the Rouse time τ_R

cannot be obtained directly from the linear viscoelastic spectrum and must be determined through other means. In some cases, previous estimates for τ_R are available in literature – e.g. the series of PS melts 50k-390k as reported by Wagner et al. [133]. For the other melts, the method for calculating τ_R presented by Ianniruberto and Marrucci [142] based on the classical formula by Osaki et al. [57] is applied. The approach is to take as reference the estimated τ_R for the shortest PS melt (PS50k) as reported by Wagner et al. [133] and scale it for the other longer PS melts in terms of the molar mass ($\tau_R \sim M^2$). Since the τ_R calculated by Ianniruberto and Marruci are based on PS melts at 403K, these values must then be shifted to the corresponding temperature by standard time-temperature superposition (TTS). This involves shift factors calculated using the WLF equation [113] whose constants are reported in the published sources for the data mentioned above.

Note that the scaling relationship $\tau_D \approx 3Z\tau_R$ commonly used to approximate τ_R is only accurate if one has the reptation time τ_{rept} and not simply τ_D since the latter is due to reptation accelerated by tube length fluctuations [59]. A reasonable estimate for τ_R using τ_D should then account for these fluctuations as done, for example, by Bhattacharjee et al [128].

To compare with theoretical models, the linear viscoleastic (LVE) spectra reported for the melts must also be fitted by a discrete number of relaxation modes i, each with a characteristic time $\tau_{0,i}$ and a fractional modulus G_i. This fitting has been done by Wagner and co-workers for the series of PS 50k-390k melts in extension and 200k melt in shear and spectra are reported in their papers [133, 143]. For the other melts, this fitting was done using the open-source software Reptate[1] a sample result of which was shown earlier in fig. 1.7. The linear viscoelastic spectra used for modeling all these melts and solutions are given in Appendix A.

4.3.2 Elongational Flows of Monodisperse PS Melts

Figures 4.1 and 4.2 show data and calculations for the steady-state extensional viscosity for the PS melts in filament-stretching experiments [129, 130]. As discussed previously, this data set has been modeled previously using tube-based approaches modified to account for the tube pressure effect [133, 135]. Here, it is our task to show that the same agreement with theory could be achieved, within the framework of our simple model, by invoking

[1]Reptate: Rheology of Entangled Polymers: Toolkit for Analysis of Theory and Experiment - developed by Jorge Ramirez and Alexei Likhtman. Available online at http://reptate.com

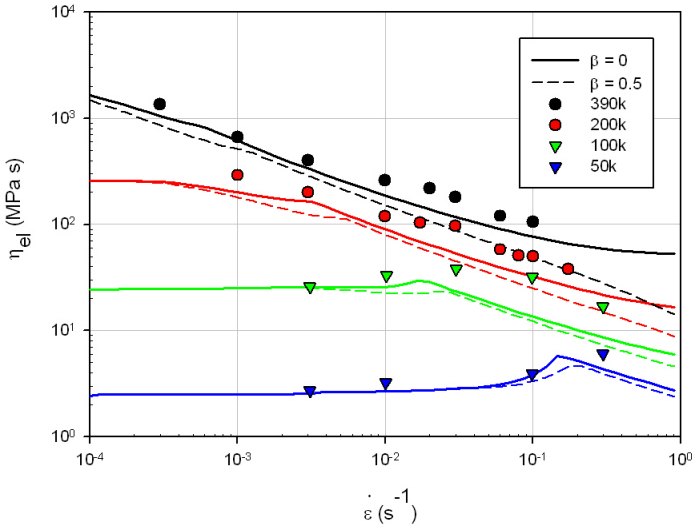

Figure 4.1: Steady-State Extensional Viscosity Data for PS Melts and Calculations using the Mead-Larson-Doi Model

monomeric friction reduction (MFR) [47, 85, 99].

Fig. 4.1 corresponds to calculations done using the Mead-Larson-Doi model without CCR ($\beta = 0$) and with CCR ($\beta = 0.5$). The latter value is chosen in correspondence with the original MLD paper where it is set to 0.5. Notice that while both curves follow the general trend of the data, there is good agreement only for low rates for all polymers and the model predictions start deviating once stretch begins to enter - i.e. when $\dot{\epsilon} \sim 1/\tau_R$. Once significant stretching occurs, the monomer friction reduction effect takes over and effectively reduces the stress. This is more prominent for the lower molecular weight melts (PS100k and 50k) which show a slight kink in the plot. The model also has better agreement for the higher molecular weight melts which is somewhat expected given the stretch-orientation decoupling invoked in the formulation of the model. This decoupling could be too severe especially for the lower molecular weight melts since the timescales for stretch and orientation in those cases are not as well separated. This is not unique to the simple model, here presented, but also manifests in more detailed approaches such as in the work of van Ruymbeke et al. [135] which invokes the same decoupling.

Fig. 4.2 corresponds to calculations done using the Ianniruberto-Marrucci

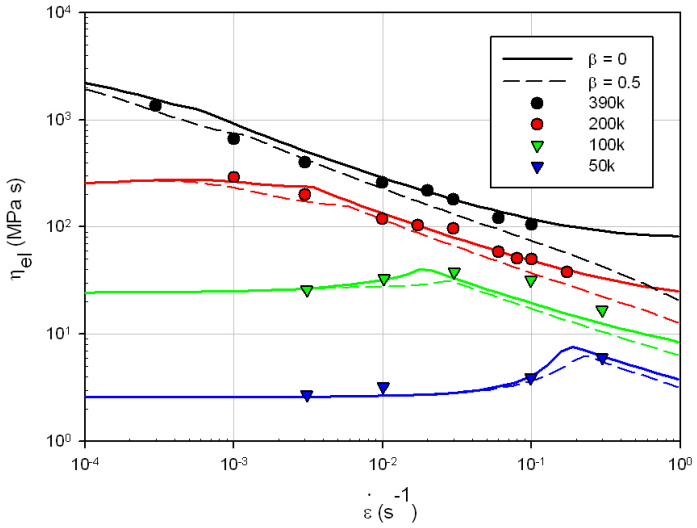

Figure 4.2: Steady-State Extensional Viscosity Data for PS Melts and Calculations using the Ianniruberto-Marrucci Model

model again without CCR ($\beta = 0$) and with CCR ($\beta = 0.5$), where the latter value of β is chosen to match the previous model. The model, which uses a differential approximation to the evolution of the orientation tensor, seems better at describing the data quantiatively, especially for the larger molecular weight melts (PS200k and 390k). Again, we rationalize this discrepancy between short and long chain melts by the stretch-orientation decoupling invoked. It is also observed that model predictions with CCR ($\beta = 0.5$) are slightly worse than those without CCR ($\beta = 0$) though still following the general trend of the data as shown in calculations from both models. This could indicate that CCR is a less important mechanism for this case of steady extensional flows. Similar observations regarding this effect of CCR has also been reported by Dhole and co-workers in their development of a differential tube model in an attempt to model the same data on PS melts [144] although by invoking the tube pressure idea [132] in this case. They report that the inclusion of CCR in their model spoils agreement with the data.

We also present the model predictions of the transient response of the higher molecular weight melts, PS200k and PS390k in figs. 4.3 and 4.4. From these figures, one could see that the general trend of the transient

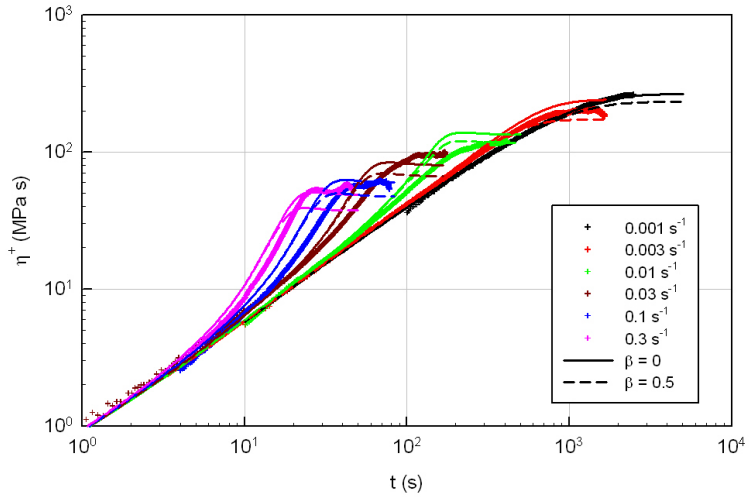

Figure 4.3: Start-up of Extensional Flow Data and Calculations for the PS200k Melt using the Ianniruberto-Marrucci Model

response can be captured by the model. As expected from the results for the steady-state calculations, the IM model can describe the transient response well. The effect of CCR is minor on the start-up behavior and the choice of parameter only affects the steady-value, which for both PS 200k and 390k melts often lie in between the curves corresponding to $\beta = 0$ and $\beta = 0.5$. Note also that the theoretical curves do not exactly match the growth of the start-up data as the increase to steady-state is slightly faster for the theoretical predictions. This, however, is due to some artefact in the measurement at the short-time behavior as the slope of the data does not exactly match the expected slope for a solid-like response (also given by the linear viscoelastic envelope).

The key result here in this section is that the inclusion of the MFR in tube models allows reasonable fitting of the extensional viscosity data for monodisperse PS melts. To gain further insight on the MFR mechanism in the model, it is useful to look at the behavior of the stretch λ and the monomeric friction ζ in transient and steady-state situations. Their steady-state values for the different PS melts considered are showed in fig. 4.5.

Figure 4.5 shows that the steady state values for λ and ζ/ζ_0 for all PS melts collapse into curves that depend only the value of β for the calculation except for the values corresponding to PS50k, pointing to a generally

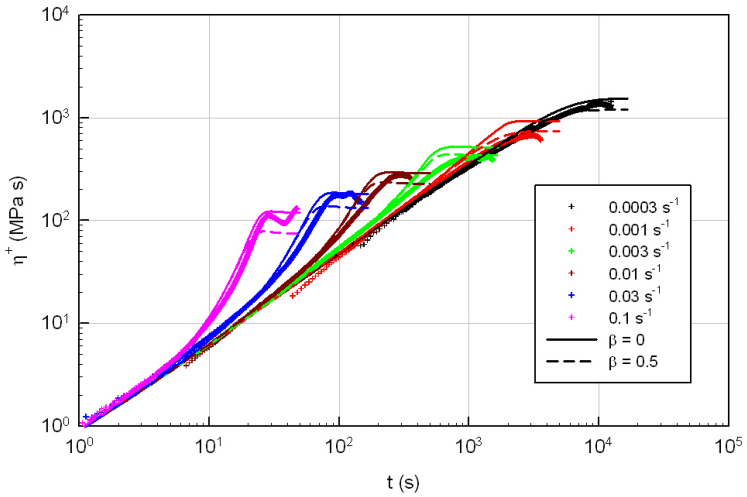

Figure 4.4: Start-up of Extensional Flow Data and Calculations for the PS390k Melt using the Ianniruberto-Marrucci Model

molecular weight independent mechanism. The exclusion of PS50k is not unusual since the melt is only mildly-entangled ($Z \approx 3-4$) and there is no real separation of the time scales for stretch and orientation (i.e. $\tau_R \approx \tau_D$) so the model is not expected to perform well. The figure also shows that the critical Weissenberg number to trigger chain stretching is slightly lower than the one needed to trigger the monomer friction reduction. This is consistent with the order-parameter dependence of ζ/ζ_0 since a minimum order and succeedingly a minimum stretch (assuming that orientation has fully occured) is required to activate the reduction. The presence (or absence) of CCR in the model, given by the selected β value, also plays an important role in the MFR mechanism since CCR affects stretch relaxation. It allows the relaxation of a part of the stretch giving rise to lower stretch values given an applied rate. In turn, the amount of stretch in the system determines the reduction of ζ.

Figures 4.6 and 4.7 show the behavior of λ and ζ in the start-up of extensional flow for PS200k and 390k respectively. First, note that the departure of λ from 1 is observed to occur at at an earlier time than the deviation of ζ from ζ_0. This stretching is responsible for the upturn of the transient viscosity from the linear viscoelastic envelope. Once a certain critical stretch of ≈ 1.4 is reached (orientation is assumed to have occured

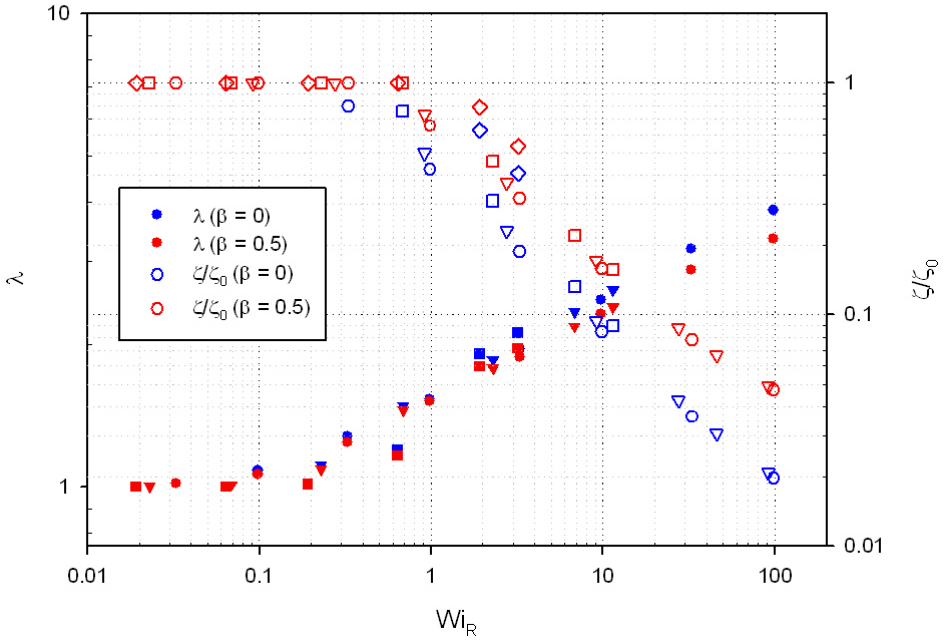

Figure 4.5: Steady-state values of the stretch λ (solid symbols) and the monomer friction reduction coefficient ζ/ζ_0 (open symbols) as a function of the Rouse time Weissenberg number ($Wi = \dot{\epsilon}\tau_R$) for PS390k (circles), PS200k (triangles), PS100k (squares) and PS50k (diamonds)

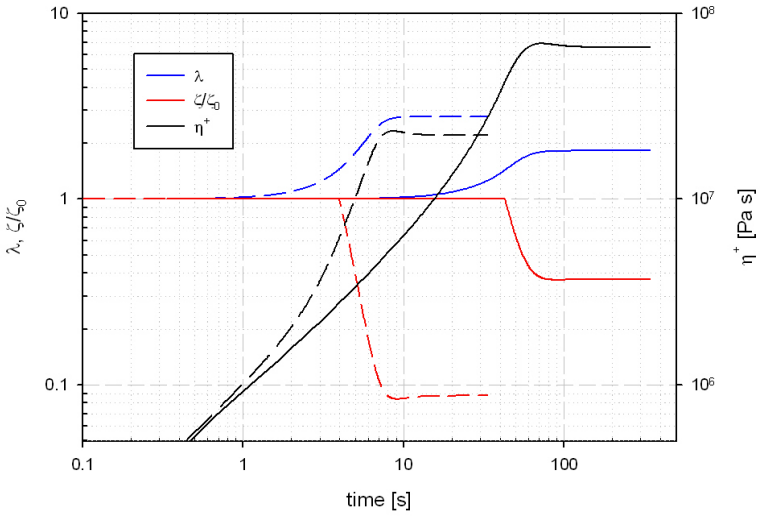

Figure 4.6: Behavior of the stretch λ and monomer friction reduction coefficient ζ/ζ_0 (open symbols) during start-up of extensional flow for PS200k for $\dot{\epsilon} = 0.3s^{-1}$ and $0.03s^{-1}$ (left to right) and $\beta = 0.5$ using the IM model

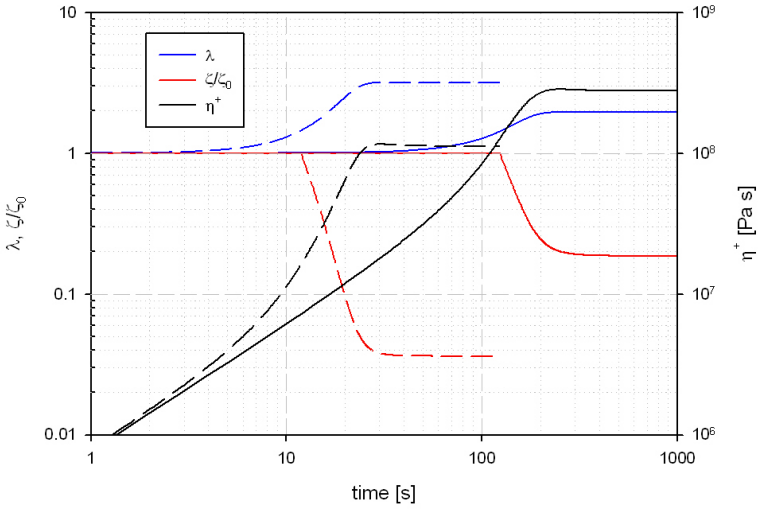

Figure 4.7: Behavior of the stretch λ and monomer friction reduction coefficient ζ/ζ_0 (open symbols) during start-up of extensional flow for PS390k for $\dot{\epsilon} = 0.1s^{-1}$ and $0.01s^{-1}$ (left to right) and $\beta = 0$ using the IM model

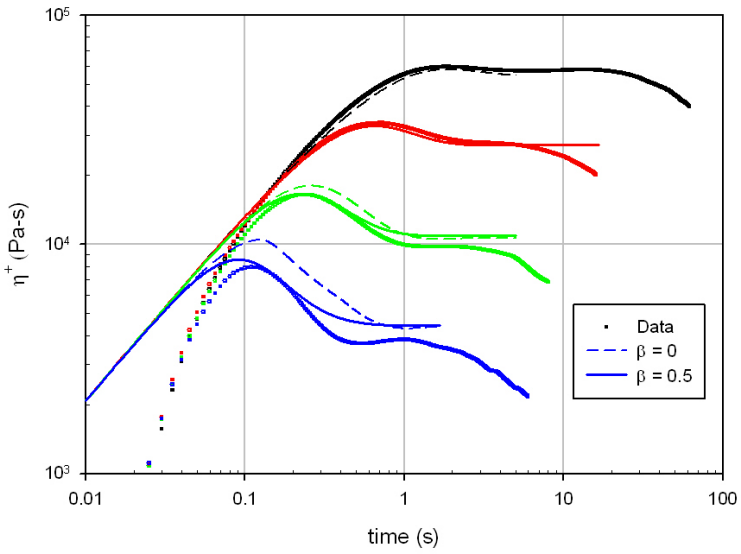

Figure 4.8: Transient shear viscosity during start-up of shear flow for the PS200k melt and calculations using the modified Ianniruberto-Marrucci model for rates $1s^{-1}$, $3s^{-1}$, $10s^{-1}$, $30s^{-1}$

fully), the MFR mechanism is triggered and ζ decreases in value until it reaches a steady-state along with λ and η^+. This value is also observed to be invariant with β as expected.

As mentioned earlier, the main result in this section is the reasonable agreement of predictions from simple tube models modified to incorporate monomeric friction reduction with experimental data on PS melts in extension. In the succeeding sections, we confront data on PS melts in other types of flow (shear, stress relaxation) to further validate this approach.

4.3.3 Shear Flows of Monodisperse PS Melts

We report the results of model predictions for shear flows in figs. 4.8, 4.9, 4.10 and 4.11. The data used for comparison are from the experiments of Schweizer et al. [139] and Snijkers and Vlassopoulos [51]. Both experiments use a *cone-partitioned-plate fixture* to minimize the effects of edge fracture that may occur in melts at large shear rates. We expect that the monomeric friction reduction mechanism included in the model is less important here since the subchains are often not stretched strongly in shear as opposed to

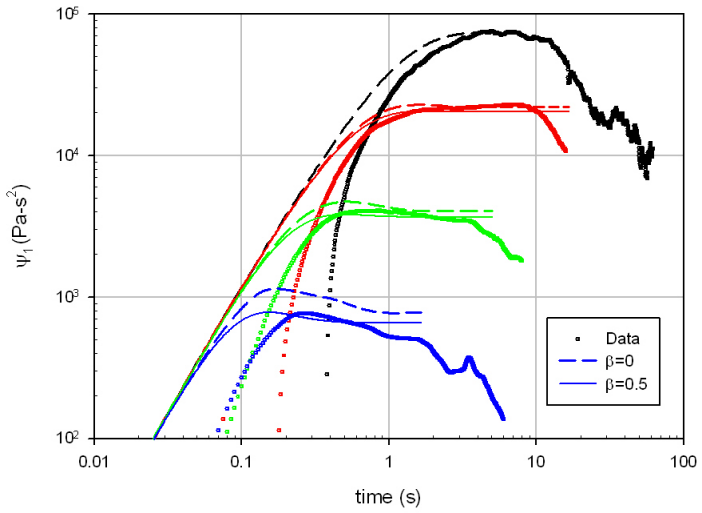

Figure 4.9: First normal stress difference coefficient in start-up of shear flow for the PS200k melt and calculations using the modified Ianniruberto-Marrucci model for rates $1s^{-1}$, $3s^{-1}$, $10s^{-1}$, $30s^{-1}$

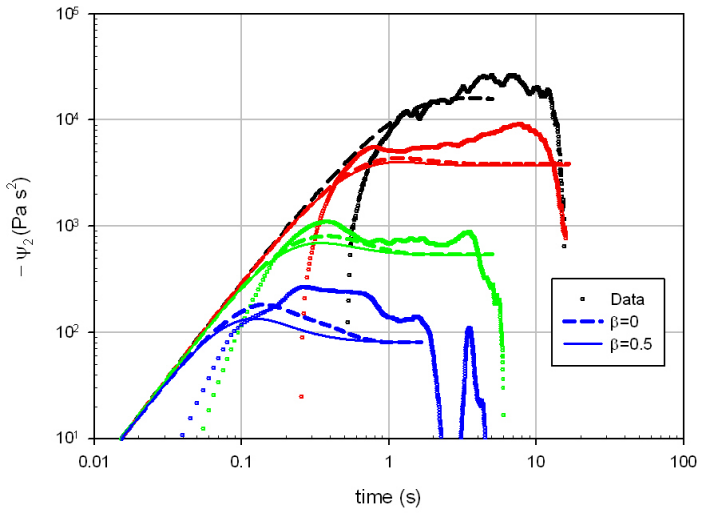

Figure 4.10: Second normal stress difference coefficient in start-up of shear flow for the PS200k melt and calculations using the modified Ianiruberto-Marrucci model for rates $1s^{-1}$, $3s^{-1}$, $10s^{-1}$, $30s^{-1}$

the case in elongation. However, the model with this untriggered mechanism should still be able to reasonably describe shear data.

Fig. 4.8 shows the shear viscosity growth data for start-up of shear flow obtained by Schweizer et al. [139]. This data for PS200k shows some problems in the measurement at short time as the data falls far under the theoretical prediction. Similarly, there is further decrease in the viscosity at long time. Hence, the only real useful comparison with the data should be made in intermediate times. Model agreement here is best at low rates while the discrepancy increases as one goes to higher rates possibly due to an overestimation of the stretch since the model only uses a single mode for the stretch, while a distribution of stretch seems to be closer to reality.

Predictions for the coefficient of the first- and second-normal stress differences are in figs. 4.9 and 4.10 respectively. There is similar agreement with the data at intermediate times and especially at the lower rates. In all predictions, the choice of β only has a minor effect on the steady shear viscosity though it clearly affects the height of the transient overshoot observed in the η^+, Ψ_1 and $-\Psi_2$ calculated.

Fig. 4.11 shows a comparison with the data on a PS182k melt from the experiments by Snijkers and Vlassopoulos [51]. This data set shows shear viscosity measurements for a wider range of shear rates. The measured values are generally consistent with theoretical predictions from low to intermediate rates while some discrepancies can be observed for the two largest rates. This discrepancy could be attributed to an overestimation of the stretch, as mentioned earlier. The choice of β also has a very small effect on the steady value of the viscosity though there is a stronger effect in modulating the height of the overshoots. These overshoots are normally attributed to transient chain stretching which can then be relaxed by CCR, if included in the model [67]. Both effects are amplified at larger rates since CCR becomes more active for more modes, while it is less active for the fast modes at low rates.

We also show flow curves corresponding to the steady values reported in the start-up curve, fig. 4.11, in figures 4.12 and 4.13, cast in viscosity and stress forms respectively. Fig. 4.12 shows the shear thinning behavior typical of entangled liquids as well as correspondence of the data with the flow curve calculated using the modified constitutive equation presented here except at the two largest rates. The data also seems to validate the empirical Cox-Merz rule [46] which relates the steady shear viscosity in flow conditions to the dynamic viscosity $\eta(\omega)$ from linear viscoelasticity.

In the stress version of the flow curve, fig. 4.13, we observe that the growth of the stress is purely monotonic and matches well with the theoret-

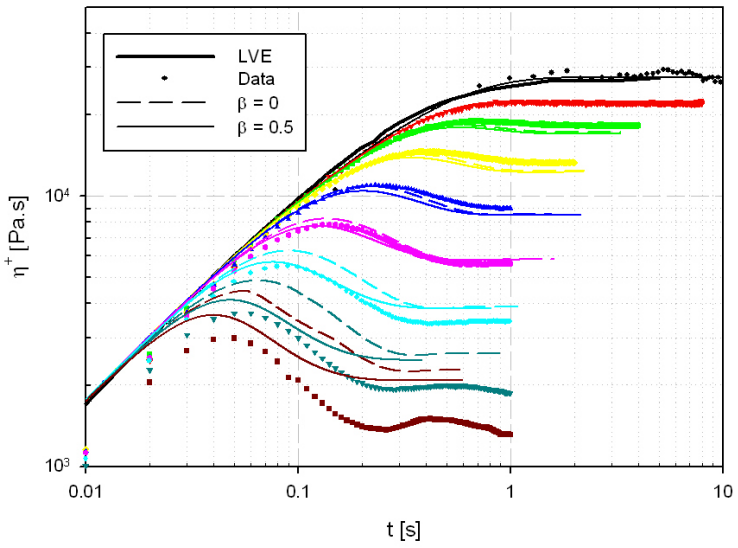

Figure 4.11: Transient shear viscosity during start-up of shear flow for the PS182k melt and calculations using the modified IM model for rates $0.10s^{-1}$, $1.78s^{-1}$, $3.16s^{-1}$, $5.62s^{-1}$, $10.0s^{-1}$, $17.8s^{-1}$, $31.6s^{-1}$, $56.2s^{-1}$ and $70.0s^{-1}$

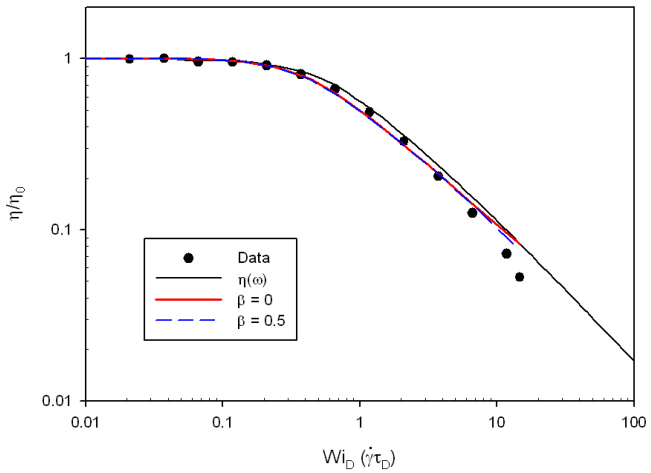

Figure 4.12: Steady shear viscosity for the PS182k melt as a function of disengagement time Weissenberg number ($\dot{\gamma}\tau_D$) and calculations using the modified IM model. The solid curve shows the dynamic viscosity obtain from linear viscoelasticity.

ical predictions for both $\beta = 0$ and $\beta = 0.5$ except for the two largest rates. These two rates show deviation from the earlier figure and are probably a signature of some artefacts in the measurement. It is possible that these rates are close to the limit of validity for this fixture. Since the flow curve is plotted in terms of the Weissenberg number defined based on the Rouse time ($\dot{\gamma}\tau_R$), it can be seen that this deviation starts with the onset of chain stretching, also predicted by the theory.

Note that Snijkers and Vlassopoulos reported that the rates they explored are below the onset of stretching based on the Rouse time they estimated using the relationship $\tau_D \approx 3Z\tau_R$ from the disengagement time τ_D. As discussed in section 4.3.1, this estimate is somehow inaccurate since τ_D is not equal to the *reptation time* since it is smaller due to tube length fluctuations and it is the reptation time that scales with the Rouse time via the factor $3Z$. Our estimate of the Rouse time based on a rescaling of the calculations of Ianniruberto and Marrucci [142] obtained by integrating the total drag force along the contour of the polymer is probably a better estimate. Based on this value, the last two rates already access the stretching regime.

The monotonic behavior of the steady stress as a function of the shear

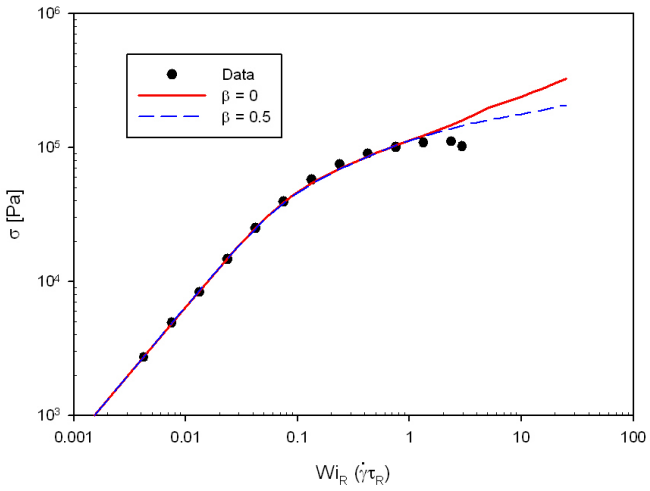

Figure 4.13: Steady shear stress for the PS182k melt as a function of the Rouse time Weissenberg number ($\dot{\gamma}\tau_R$) and calculations using the modified IM model.

rate for the value $\beta = 0$ may seem peculiar and deserves some comment. In single mode calculations, the expected behavior for the steady stress if taking $\beta = 0$ is non-monotonic as shown in fig. 1.10 and manifests the instability predicted by Doi and Edwards [7]. However, when considering a spectrum of relaxation times, as in this case, this non-monotonicity could be smeared out by summing over all the modes giving rise to a monotonic curve as shown here. Similarly, the fact that chain stretch is included in the model would mean that the stress would continue on increasing well above $Wi_R \approx 1$. Note that in this regime of large rates, the inclusion of CCR starts to matter since CCR also operates in stretch relaxation and not just in orientational relaxation. This gives rise to a lower predicted steady stress value for larger values of the CCR parameter. However, this regime is only barely accessed by the data so no further comments can be given.

Finally, the stretch in these shear cases considered do not get larger than the critical value λ_{crit} required to activate the monomeric friction reduction mechanism in general. The notable exception is for the two fastest rates in PS182k $\dot{\gamma} = 56.2s^{-}1, 70.0s^{-}1$ though the reduction here is only transient and the equilibrium value of ζ is recovered at the steady-state. This is shown in fig. 4.14.

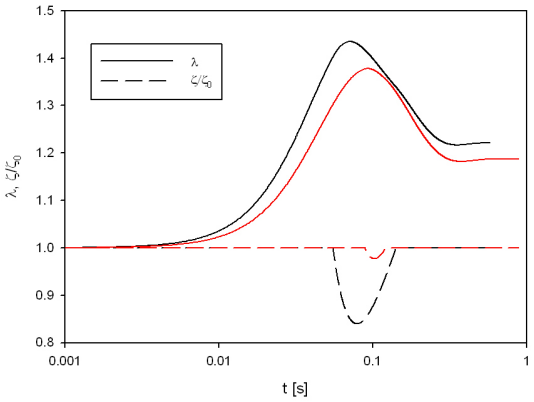

Figure 4.14: Transient stretch (λ) and monomer friction reduction (ζ/ζ_0) for the PS182k melt calculated using the modified IM model for rates = $56.2s^{-1}$ (red) and $70.0s^{-1}$ (black).

4.3.4 Stress Relaxation After Cessation Flow of Monodisperse PS Melts

We also consider the data from the experiments of Nielsen and co-workers on stress relaxation after cessation of elongational flow [138] on a PS145k melt. This data set shows accelerated stress relaxation for melts that experienced larger elongational rates. Yaoita and co-workers use this in obtaining the order parameter-dependence of the monomeric friction and also fit the same data using slip-link simulations [99].

In figure 4.15, we compare model predictions from the Iannirubertо-Marrucci differential equation modified to include MFR with the experimental data [138]. Model predictions use $\beta = 0$ and $\beta = 0.5$ for the CCR parameter. The choice $\beta = 0$ seems to more consistent with steady and transient elongational viscosities for the melts considered so far, in section 4.3.2. This is verified in fig. 4.15 for the start-up part where the model agreement with the data is better for $\beta = 0$ (except for $\dot{\epsilon} = 0.0003$). In the start-up part, the choice $\beta = 0.5$ seems to underestimate the final stress level.

However, for the stress relaxation part, model agreement is generally better for $\beta = 0.5$ possibly because of this underestimation since the initial stress before the decay is smaller than the initial stress for the data. For $\beta = 0$ where the stress starts at a value comparable to the data, the theoretical

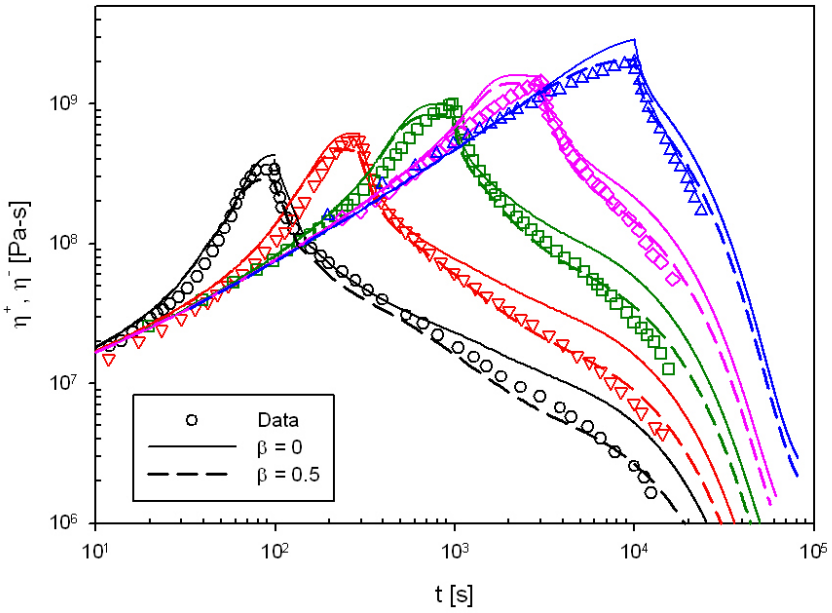

Figure 4.15: Start-up and relaxation viscosities for the PS145k melt for rates $\dot{\epsilon} = 0.03, 0.01, 0.003, 0.001$ and 0.0003 (left to right). Symbols are data from Nielsen et al. while curves are predictions using the modified Ianniruberto-Marrucci model.

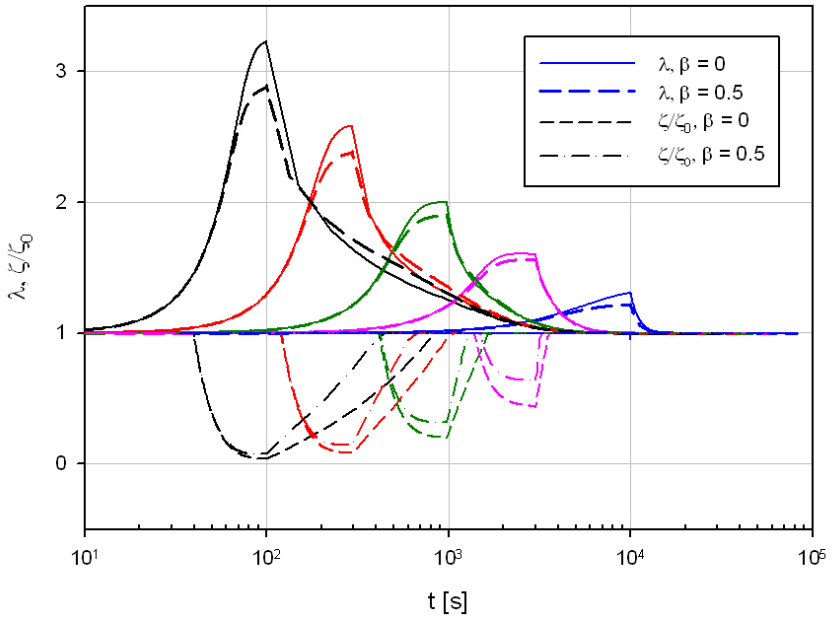

Figure 4.16: Stretch (λ) and monomer friction reduction coefficient (ζ/ζ_0) for the start-up and relaxation of the PS145k melt for rates $\dot{\epsilon} = 0.03, 0.01, 0.003, 0.001$ and 0.0003 (left to right).

prediction is consisent only in the initial stage of the stress relaxation and the deviation broadens at long time. In general, the viscosity η^- is observed to relax faster than this prediction.

We also analyze the start-up and stress relaxation processes in terms of the stretch λ and the MFR coefficient ζ/ζ_0 as shown in fig. 4.15. λ has an equilibrium value of 1, increases up to a maximum value as the melt is extended and then relaxes back to 1 during cessation of flow. Conversely, ζ/ζ_0 starts at 1 and starts to decrease when the stretch reaches the minimum critical value and it then relaxes by increasing back to 1 upon cessation of flow. Note that while the reduction is triggered at a later time (since a critical value of λ must be reached before reducing the friction), the relaxation of both λ and ζ/ζ_0 occur simultaneously during cessation of flow. However, ζ/ζ_0 reaches the equilibrium value of 1 before λ. This is true for all the rates considered. The inclusion of CCR in the system, regulated by the value of β, is also observed to accelerate the relaxation of ζ to its equilibrium value.

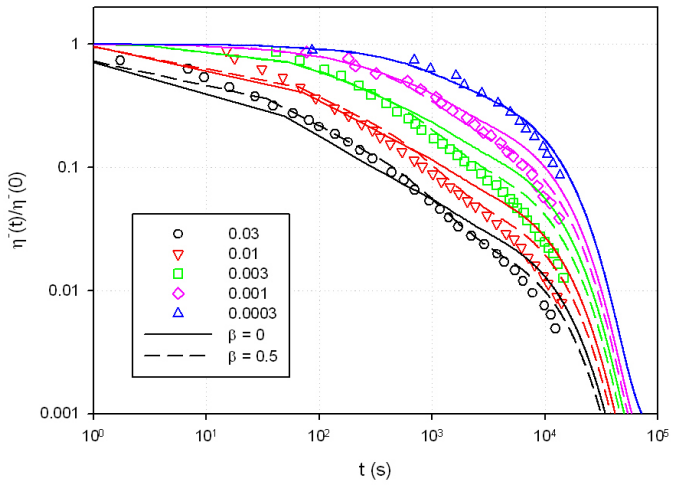

Figure 4.17: Stretch (λ) and monomer friction reduction coefficient (ζ/ζ_0) for the start-up and relaxation of the PS145k melt for rates $\dot{\epsilon} = 0.03, 0.01, 0.003, 0.001$ and 0.0003 (left to right).

To highlight the acceleration of the stress relaxation as a function of the elongation rate $\dot{\epsilon}$ experienced by the melt before cessation flow, we isolate and replot the relaxation part of the viscosity curve in fig. 4.17. Here, the quantity presented is $\eta^-(t)$ normalized by its value upon cessation of flow $\eta^-(0)$ versus time t. In this plot, we suppress the importance of the initial values of the stress at the start of relaxation which, from fig. 4.15, do not perfectly coincide for both data and predictions, particularly for $\beta = 0.5$. Instead, the focus is on the general trend of the relaxation process which is faster for the larger elongation rates, prior to cessation of flow. In general, the data seems to confirm the behavior from theoretical predictions though the calculations for $\beta = 0.5$, i.e. including CCR, seems to match the data better since predictions without CCR only has agreement at early time. We take this agreement as a validation of the modified constitutive equation we have presented.

4.3.5 Elongational Flows of Monodisperse PS Solutions

Lastly, we show here that the same modeling approach can also be applied to PS solutions. The data confronted here are on PS solutions with 7.35% and 10% concentrations of an high molecular weight PS from the experiments of

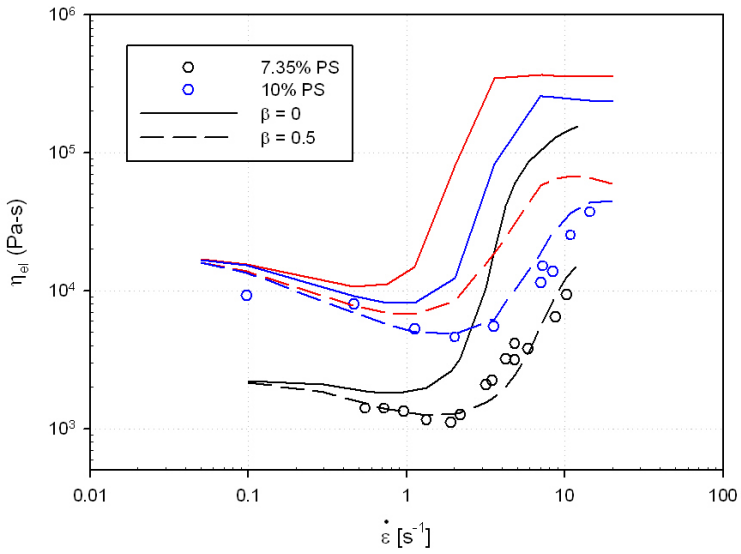

Figure 4.18: Steady elongational viscosity as a function of the elongation rate for the PS solutions. Solid and dashed curves are predictions using the modified IM model. Two predictions are presented for the 10% solution with the blue curves corresponding to $\tau_R = 0.28$ and red curves corresponding to $\tau_R = 0.46$.

Sridhar and co-workers [127, 128]. Other details on the materials are given in table 4.2. Here, we consider data on the steady elongational viscosity for both solutions reported by Bhattacharjee et al. [127] and data on the transient stress growth for the 10% solution reported in a subsequent paper [128].

Figure 4.18 shows data for the steady-state elongational viscosity for both solutions by Bhattacharjee and co-workers [127] as well as theoretical predictions from the modified Iannirubertо-Marrucci model. The black curves are predictions for the 7.35% solution using $\tau_R = 0.27$. This value is obtained from the work of Yaoita and co-workers [98] where they examined the same solutions using slip-link simulations. The prediction using this value for τ_R and using $\beta = 0.5$ seems to reasonably match the data while the prediction using the same τ_R but without CCR, i.e. $\beta = 0$, is less successful in capturing the data.

Yaoita et al. also report a value of $\tau_R = 0.46$ for the 10% solution [98],

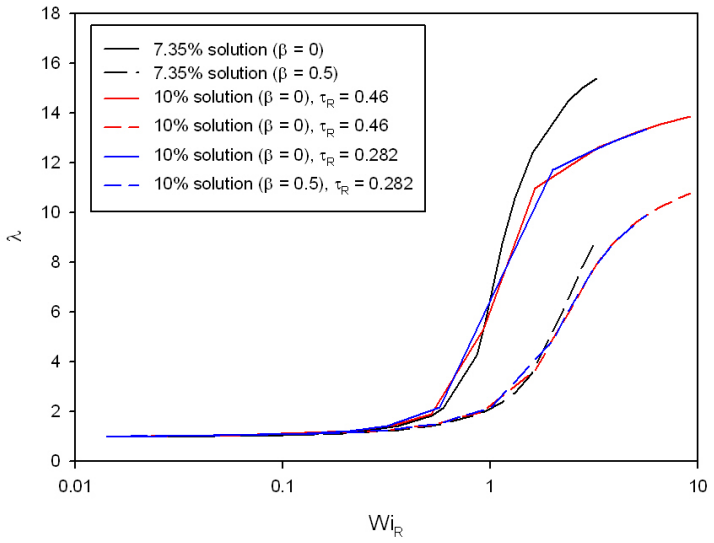

Figure 4.19: Stretch (λ) as a function of Rouse time Weissenberg number $Wi_R = \dot{\epsilon}\tau_R$ for both PS solutions.

corresponding to the red curves in fig. 4.18. The comparison with the red curves with the data, shown by the blue symbols, is clearly less successful compared to that for the 7.35% solution. We then considered an alternative value of $\tau_R = 0.28$ as reported by Bhattacharjee et al. in a subsequent paper [128] and predictions for this value correspond to the blue curves in fig. 4.18. The agreement with the data using this value of τ_R and $\beta = 0.5$ is more reasonable. For $\beta = 0$, the prediction is again very different from the data and the elongational viscosity minimum and upturn are overestimated.

From these results, two clear points are apparent. The first is the importance of the parameter choice for the calculations, particularly with respect to the Rouse time τ_R. In particular, for the 7.35% solution, we obtained a value for τ_R from detailed multi-chain slip-link solutions [98] which seems to work in capturing the data, if one includes CCR. However, the value obtained using the same simulations for the 10% solution seems less successful, as shown by the red curves in fig. 4.18. The value for τ_R that did give a reasonable prediction was from Bhattacharjee et al. [128] who compared the data with predictions from the original Ianniruberto-Marrucci model [72]. In their estimate, which was based on τ_D, they accounted for contour length fluctuations using the theory of Milner-McLeish [75] to obtain a rep-

tation time which is then related to $3Z\tau_R$. While reasonable, this estimate is model-dependent as are all estimates for τ_R based on τ_D [127] and this induces some uncertainty among other possible uncertainties reported previously by Osaki et al. [145] which could be as much as a factor 5. Note that the two estimates here differ only by a factor of 1.63 which is not huge though significant in drastically altering the model predictions.

The second point is regarding the importance of including CCR in the model. In the previous sections, there is some uncertainty regarding this when considering PS melts since the choice of β has a very mild effect on model predictions in those cases with the choice of $\beta = 0$ seemingly more successful in steady and start-up of extensional flow while the choice of $\beta = 0.5$ seems to be preferred in the case of stress relaxation. Here, for the case of PS solutions, the choice has a clear difference and the inclusion of CCR in the model seems to be important in matching the data. A reason for this is apparent when one considers the evolution of the stretch λ as a function of the non-dimensionalized rate $\dot{\epsilon}\tau_R$ as shown in fig. 4.19.

Note that near the onset of chain stretching ($Wi_R \approx 1$), the curves for both solutions superimpose though they eventually differ at large rates due to differences in the finite-extensibility factor. In general, the stretch values explored in the extension of these solutions for $Wi \approx 1 - 10$ are significantly larger than the stretch values explored in the melts for similar rates. The reduced stretching in melts is, of course, due to the MFR which suppresses the stretching by effectively shifting the stretch relaxation time to lower values via equation (4.19). This difference in stretch levels is significant in the issue of CCR since CCR is a mechanism for stretch relaxation and its inclusion in the model can reduce the predicted stretch, also apparent in fig. 4.19.

Returning to fig. 4.18, it is clear that calculations including CCR in the model better match the measured data and this reflects the importance of accounting for CCR in the model. The calculations here for the 10% solution for both values of τ_R which does not include CCR has the feature of having a large growth of the stretch, reflected in fig. 4.19. This induces the triggering of MFR which causes the change in the slope of λ beyond a certain Wi_R. It also manifests in the steady elongational viscosity as the plateau or slight reduction of η_{el}. This feature is certainly not exhibited by the elongational viscosity data and, hence, MFR occuring in the solutions considered here probably does not occur. Certainly, the inclusion of CCR in the model reduces this possibility (since the stretch may never reach the critical value required to trigger MFR) and the corresponding predictions match the data reasonably.

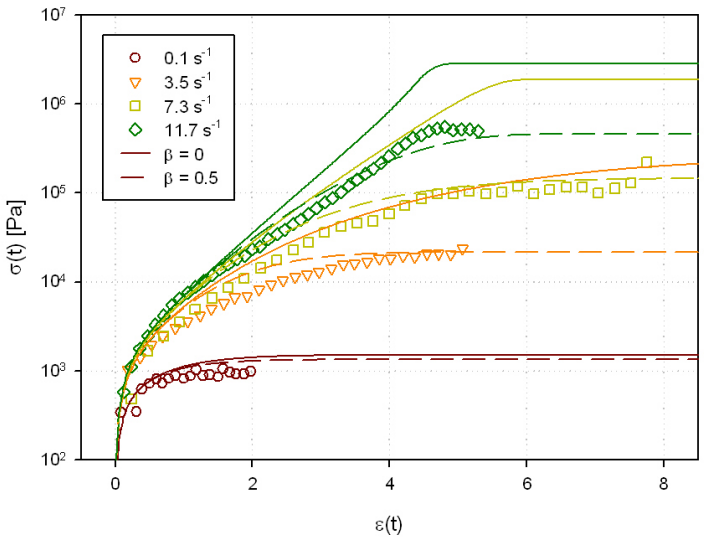

Figure 4.20: Stress growth curve for the 10% PS solution during the start-up of extensional flow. The x-axis is the total deformation applied. Solid and dashed curves are predictions using the modified IM model.

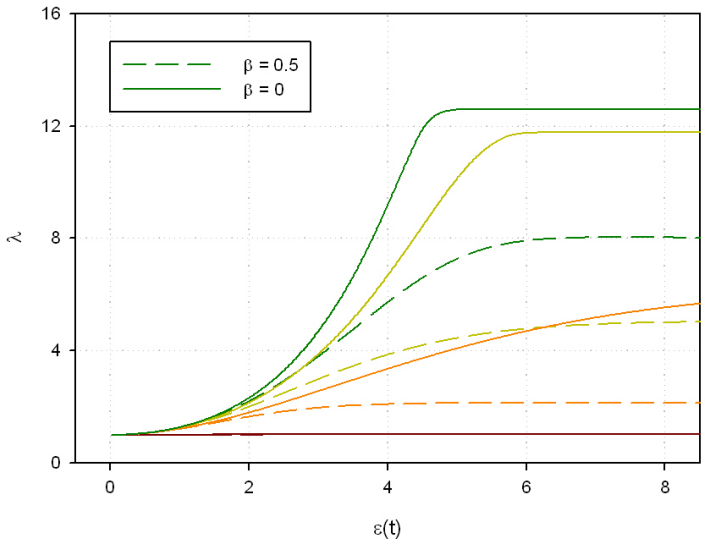

Figure 4.21: Stretch (λ) predictions for the 10% PS solution from the modified IM model as a function of total deformation applied.

We also consider the transient stress growth curve for one of the solutions (10% PS) [128], the data for which are presented in fig. 4.20 along with theoretical predictions using the modified IM model for two values of the CCR parameter β. Figure 4.20 clearly shows that the inclusion of CCR is important in matching the data – calculations using $\beta = 0.5$ correspond to the data reasonably while those using $\beta = 0$ deviate significantly particularly at the largest rates. This is again rationalized by the role of CCR in stretch relaxation. This is also apparent when one considers the stretch calculated with the model with and without CCR, as in fig. 4.21.

Finally, we summarize the results for the extensional rheology of solutions and melts by plotting the steady stress normalized by the plateau modulus G_0^N versus the nondimensionalized extensional rate for some of the PS solutions and melts considered here in fig. 4.22. The solution data for the steady stress clearly manifests an upturn or increase in slope for $Wi = \dot{\epsilon}\tau_R \approx 1$ while the melt data for the steady stress continues increasing without the upturn and this have lead some to question the fundamental difference between melts and solutions [32]. Here, we developed the idea of flow-induced monomeric friction reduction (MFR) for explaining this difference and we formulated a simple modeling approach that accounts for the

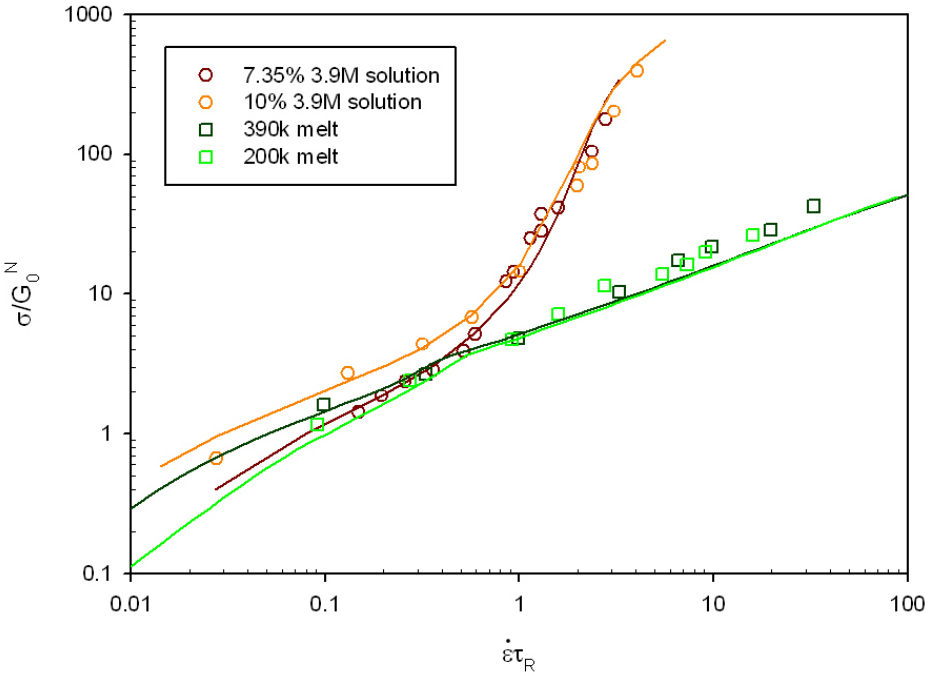

Figure 4.22: Normalized steady stress for PS solutions and melts as a function of their Rouse time Weissenberg number. Data are shown by open symbols while theoretical predictions using the modified IM model using $\beta = 0.5$ are solid curves.

MFR. This approach can be applied successfully for both melts and solutions and can reasonably capture the trend of both data sets as shown in fig. 4.22. This monomer friction behavior is not the only difference between the two, as recently pointed out by Huang and co-workers [33]. The maximum-extensibility ($\lambda_{\max}$) which is determined by the number of Kuhn segments in each entanglement strand (N_e) is also obviously different for melts and solutions with the latter having a lower maximum-extensibility. This difference is also included in our model since we incorporate finite-extensibility effects.

It is important to note that this attempt to model both the data on PS solutions [127, 128] and on PS melts [129, 130] is not the only one in literature. Sridhar and co-workers have observed that the PS solutions data are at least qualitatively consistent with tube models accounting for both chain stretch and CCR as reported in their original papers [127, 128, 146]. Regarding the PS melts, as mentioned in the introduction, there are models which invoke the idea of interchain/intertube pressure (ICP) [133, 134, 135] that can capture the extensional data for the melts. The shortcoming of the ICP approach, however, is that it does not distinguish between melts and solutions and it is unclear why the ICP is essential only in melts. There has also been no reported evidence (rheological or otherwise) corroborating the idea of tube diameter changes in melts under nonlinear flows.

Recently, Kushwaha and Shaqfeh report results from slip-link simulations done in planar extensional flow which they relate to the measured data on PS melts [147]. They observed that the primary extensional viscosity in their simulation exhibited the extensional thinning observed in experiments. However, the scaling they obtained is $\eta_{\text{el}} \sim \dot{\epsilon}^{-0.66}$ which is somewhat steeper than what was reported. More importantly, their conclusion is not without reservation as the simulations were done in planar extensional flow and not in uniaxial extension. Their simulation method is also derived from the slip-link model of Masubuchi, et al [22, 91] which has been applied in uniaxial extension [91, 98] but shows no extensional thinning.

Other than the work of Yaoita and co-workers on slip-link simulations which invoked the monomeric friction reduction discussed here [98, 99] the only other reasonable attempt to model the data on both melts and solutions has been due to Park and co-workers [148]. They considered a configuration-dependent friction coefficient in their stochastic simulations. This factor is regulated by a parameter k and affects the relaxation time directly. Results of their simulation are found to be in agreement with the experimental data on monodisperse PS melts [129] and PS solutions [127] for the choice $k = 0.99$ for both. In their model, this would correspond physically to

some fully aligned state of the system. Their way for accounting for this effect is, however, more *heuristic* and is regulated by the parameter k whose molecular basis is not nkown. It is also not clear

The difference with their work and in what we present here, however, is their more *heuristic* way of accounting for the effect which is based on a parameter k whose molecular basis is not known. It is also not clear if their simulations distinguish between melts and solutions since the same value for k is used for both. In contrast, the approach here has a more solid physical basis for the modification and the actual MFR effect was extracted directly from data and confirmed by detailed simulations.

4.4 Conclusions

In this chapter, we confronted nonlinear rheology data on PS solutions [127, 128] and melts [129, 130]. In extensional flow, the two systems behave differently with solutions showing extensional thinning followed by an upturn in the elongational viscosity, consistent with current tube models, while the melts showed continuous extensional thinning with no upturn. Here, we explored the mechanism of flow-induced monomer friction reduction (MFR) proposed and developed in previous work [47, 99, 85] by incorporating it in simple tube-based constitutive equations – particularly the integral equation of Mead, Larson and Doi (MLD) [71] and the differential equation of Ianniruberto and Marrucci (IM) [72, 79].

Predictions of both models compare well with the available data on PS melts for both steady-state and transient. For the case of steady-state predictions, predictions from the IM model are better in fitting the data than the MLD model particularly for the case of $\beta = 0$ corresponding to no CCR in the system. Predictions with CCR $\beta = 0.5$ also capture the general trend of the data though the fit is better for the calculations without CCR. The same observation was also true for transient calculations.

To further validate the model, we also confront nonlinear shear rheology data on PS melts [51, 139] and data agreement was found to be reasonable though with some deviations are larger rates. This is possibly due to an overestimation of the stretch. It was also shown that for the largest rates considered that the MFR mechanism was triggered in transient due to sufficient stretching. The equilibrium value of the friction was, however, recovered at steady-state since the steady state stretch was not sufficiently large.

We also confronted stress relaxation data after cessation of flow on a PS

melt [138] and predictions are reasonable though the relaxation of the data was observed to be faster than predicted at long times. We showed that the triggering of stretch during start-up of flow precedes the triggering of the monomer friction reduction, as expected from the observed dependence of the friction with the order parameter. We also showed that the relaxation of the monomer friction to its equilibrium value is faster than the relaxation of stretch in the calculations.

Finally, we examined transient and steady-state extensional data on PS solutions using the same approach. We find that for solutions the inclusion of CCR in the model is crucial in obtaining the correct steady-state and transient behavior shown by experimental data. This is reasonable since there is significantly more stretching in solutions, than in melts, due to the suppression of stretch by MFR for the latter. For the former, the inclusion of CCR is important since it is a mechanism not just for orientational relaxation but also for stretch relaxation.

The main result here is the development of a simple tube-based constitutive equation that is able to simultaneously describe the data on melts and solutions, as shown in fig. 4.22, using the same parameters. In this case, the only parameter that does not depend on the molecular structure of the melt is the CCR parameter β, the choice of value for which was observed to be more important for solutions and less important in melts.

So far, our model has been applied for monodisperse systems in both shear and extension. However, more stringent tests of the model and the monomer friction reduction mechanism are present in literature, in the form of bidisperse and polydisperse PS melts whose extensional data have been reported in literature [33, 130]. The application of the model presented here would require some modification to account for the varied molecular weight distribution and would constitute future work. However, we anticipate that the same physics of monomer friction reduction should be operative in the case of bidisperse and polydisperse melts though this remains to be shown.

Chapter 5

Conclusions

5.1 Summary

In this work, three problems concerning entangled polymers have been confronted from the perspective of molecular models (tube models or slip-link simulations).

First, the effect of entanglements on rubber elasticity was investigated using slip-link simulations. This was based on previous work by Oberdisse and co-workers [41, 42] who considered end-linked networks which have a monodisperse distribution of elastic strand length between crosslinks. They found that the stress-strain curves for those systems do not compare well with predictions from the replica theory of Edwards and Vilgis [101]. The latter theory gives rise to a constitutive equation that is known to describe experiments well.

Here, we considered randomly-crosslinked networks using the Primitive Chain Network (PCN) model of Masubuchi and co-workers [22, 104]. The method of preparation for these networks is different and gives rise to a broad distribution of elastic strand lengths between crosslinks. We observed that the stress-strain curves obtained from the simulations can be fitted reasonably by the theory of Edwards and Vilgis. Hence, it becomes puzzling why there is disagreement of the simulation results with this theory only for the end-linked case.

To eliminate the discrepancy, we considered two possibilities on modifying the PCN model:

- Entanglement stripping at large deformations
- Strain-dependence of the tube potential, as proposed by Rubinstein

and Panyukov [105]

These modifications were found to be effective in capturing the predicted stress-strain behavior for the system though they suffer either from being unphysical (as in the case of entanglement stripping) or not immediately applicable (as in the case of the strain-dependent tube potential).

We also confronted the thermodynamic inconsistency of the model based on ideas from Schieber [106, 107] and Greco [117]. We present a more thermodynamically-consistent dynamic equation for the monomer exchange across slip-links which we implemented the PCN simulations for randomly-crosslinked networks. We found that it gives rise to slightly different strain-softening behavior for the networks. However, as this only a small difference, it is unlikely that introducing this correct sliding equation in the simulations for end-linked systems will remove the previous discrepancy observed.

Second, data on parallel superposition flows of monodisperse solutions by Wang and co-workers [43, 44] were confronted using a tube-based constitutive equation. The approach followed the previous work of Somma and co-workers [121] which was applied to polydisperse melts and verified that the superposition storage modulus is more drastically affected by shear flow than the superposition loss modulus. The effect of flow on the loss modulus was observed to be only near the terminal region.

In confronting the monodisperse systems, a new feature that was absent in polydisperse systems arose in the form of the dynamic crossover of the superposition storage and loss moduli. This crossover would have a frequency that is related to the effective relaxation time of the system. Wang and co-workers observed that the reciprocal of this effective relaxation time scales universally with $5\dot{\gamma}$ as shown by the data. They interpreted this scaling using the idea of convective constraint release (CCR) proposed previously by Marrucci [45] and incorporated in current tube models.

We found that confronting the data by Wang and co-workers using a simple tube-based constitutive equation could allow validation or rejection of this assertion. By doing a linear expansion on the constitutive equation, expressions for the superposition moduli are obtained and compared directly with experiments. Model agreement is satisfactory for low to intermediate rates while some deviations are observed at larger rates possibly because the model does not account for stretch. More importantly, we found that model predictions on the dynamic crossover are invariant of the choice for the CCR parameter in the model and non-inclusion of CCR could still reasonably describe the measured data. Hence, we show that the assertion by Wang

and co-workers is not valid and that shifting of the effective relaxation time in superposition spectra is due simply to orientation and not CCR.

Finally, data on the nonlinear rheology of entangled PS melts and solutions were confronted using a simple tube-based constitutive equation modified to account for monomer friction reduction (MFR). The latter idea has been proposed and developed recently [47, 99, 85] to rationalize the different behavior exhibited by melts and solutions in extensional flows. The said difference was striking, with respect to classical tube models, since the two systems were expected to behave similarly.

By incorporating the MFR effect in multimode tube-based constitutive equations [71, 72] with CCR and chain stretch, we showed that the available data for the PS melts and solutions could be described reasonably using the same equation. The key is the reduction of the monomer friction induced by significant changes in its molecular environment. In melts, this occurs when the other chains are oriented and highly stretched such that other monomers start to align. In solutions, this seldom occurs even at large stretching since the environment consists mostly of solvent molecules which relax quickly.

Data agreement with the modified model is quite successful in the variety of situations considered here: transient and steady-state extension, transient and steady-state shear and stress relaxation after cessation of flow for melts and transient and steady-state extension for solutions. For melts, the choice for the CCR parameter seems less crucial since there is no significant stretching that CCR can relax. This lack of stretching is due to the presence of the MFR mechanism. For solutions, however, the stretching is significant and unsuppressed and, hence, CCR plays a more important role.

5.2 Outlook

The molecular rheology of entangled polymers has a number of open problems in various directions. In this work, some progress has been made in answering or settling some issues in the three problems confronted. In general, there is further work to be done in different directions for each problem to further validate the conclusions presented here and to further the understanding of these systems.

For slip-link simulations, significant progress has been made in developing the PCN model for entangled melts [22, 91, 98, 99] including branched polymers [89] and heterogeneous polymers [92]. However, the simulation of entangled networks is still somewhat problematic as shown here. We demonstrated that simulation results for the case of randomly-crosslinked

systems are consistent with predictions from replica theory [101] though the same level of agreement is absent in end-linked networks [41, 42] which are supposed to be simpler. In this work, we proposed a new sliding equation for monomer exchange in slip-links based on the chemical potential balance. This dynamical equation is more thermodynamically consistent and gives rise to a slightly different stress-strain behavior when applied to randomly-crosslinked systems. However, the difference is minimal in comparison with the large discrepancy observed for end-linked systems. Hence, it is important to explore other possible issues why this discrepancy is present.

One such important issue to address is the issue of equilibration and whether the method of network preparation used in the previous work gives rise to equilibriated networks, which are important in simulations [110]. Methods for preparing equilibrated networks in other simulations, such as molecular dynamics simulations [103, 87], could be considered and applied in the PCN model. Another alternative would be to use a pre-equilibriated network structure from molecular dynamics and convert the structure into a network of primitive paths using known methods [17, 115] and use this network as starting point or input in the slip-link simulations.

For superposition flows, the approach presented here provides a simple constitutive approach to modeling the data on polydisperse and monodisperse melts and solutions. However, the agreement of the model with data is satisfactory only for intermediate rates and not for rates where chain stretching might be significant. Chain stretching was ignored in the model formulation due to two complications it might induce: the necessity of specifying a stretch relaxation time for each mode and the drawback of having a non-analytic solution for the superposition spectra. The latter can be circumvented simply by solving the equations numerically. The former issue is less straightforward and would deserve further investigation.

For the nonlinear rheology of entangled melts and solutions, the view that the monomeric friction reduction is important in nonlinear rheology, particularly in discriminating the behavior of melts from solutions has been investigated in this work by proposing a simple constitutive equation that accounts for this effect and that simultaneously describes solution and melt rheology data. However, this constitutive equation has only been validated with data on monodisperse systems. Data on bidisperse and polydisperse systems using the technique of filament stretching rheometry [129, 130] have also been presented in literature and they provide more rigorous validation of the modeling framework. As mentioned, the application of the model to these systems would require further work in accounting for different molec-

ular weight distributions possibly through the form of mixing rules, some versions of which were used in previous approaches [134, 135].

It should also be mentioned that the tube-based constitutive equation considered here is a simple model which involves a number of approximations such as the decoupling of stretch and orientation and the application of CCR only at the chain level. A more detailed constitutive equation based on the tube model have also been proposed previously where CCR is implemented on a finer scale [73]. Another more advanced nonlinear model which properly resolves the physics of stretch relaxation in bidisperse systems by considering nested tubes has also been proposed recently [149]. It would then be interesting to see how the modification of these models by MFR could alter their predictions in both extension and shear.

Finally, the impact of MFR in the nonlinear rheology of branched polymers should also be appraised. To date, there has only been one data set reported on the elongational rheology of well-defined branched polymers [150] though this situation should improve due recent interest on complex architecture polymers [29]. Beyond the physics proposed by McLeish and Larson in the successful pom-pom model [82], new ideas on the nonlinear behavior of branched polymers have also been emerging [142]. An improved model for the transient and steady-state response of these systems is also under development and monomer friction reduction could be important in this model.

Appendix A

Linear Viscoelastic Spectra

Fitting of the linear viscoelastic spectra was done using the open-source software Reptate, developed by Ramirez and Likhtman and available online at http://reptate.com/. The obtained spectra for the melts and solutions considered in the work are reported in the succeeding tables.

Table A.1: LVE Spectra for PBD Solutions Considered in Chapter III

Sample Name	Source	Fitting Method	No. of Modes (i)	τ_i [s]	g_i [Pa]
3% 2.6M PB	[44]	Reptate	7	1.46E2	5.48E1
				1.12E1	9.53E1
				8.59E-1	9.50E1
				6.57E-2	1.68E2
				5.04E-3	4.23E2
				3.86E-4	9.12E3
				2.95E-5	8.70E4
5% 0.7M PB	[43]	Reptate	7	4.93E1	3.90E2
				7.50E0	4.63E2
				1.14E0	4.21E2
				1.73E-1	7.39E2
				2.63E-2	1.95E3
				4.00E-3	6.22E3
				6.07E-4	2.16E5
10% 0.7M PB	[43]	Reptate	8	8.22E2	1.05E1
				1.50E2	3.39E1
				2.74E1	1.90E3
				4.99E0	1.84E3
				9.10E-1	1.33E3
				1.66E-1	1.38E3
				3.03E-2	6.22E2
				5.52E-3	7.89E3

Table A.2: LVE Spectra for PS Melts Considered in Chapter IV - Part I

Sample Name	Source	Fitting Method	No. of Modes (i)	τ_i [s]	g_i [Pa]
50k	[130]	Wagner [133]	4	6.33E0	1.05E5
				9.85E-1	1.40E5
				9.61E-2	3.71E5
				2.91E-3	9.15E6
100k	[130]	Wagner [133]	7	1.35E3	1.11E2
				8.51E1	7.39E4
				1.93E1	6.77E4
				3.40E0	7.73E4
				4.77E-1	1.47E5
				3.06E-2	1.02E7
				6.73E-3	4.10E5
200k	[129]	Wagner [133]	6	1.26E3	4.33E4
				4.43E2	4.96E4
				9.20E1	5.46E4
				1.96E1	2.71E4
				5.29E0	3.71E4
				4.75E-1	2.38E5
390k	[129]	Wagner [133]	8	1.71E4	2.28E4
				5.97E3	5.15E4
				1.14E3	4.31E4
				2.35E2	3.33E4
				5.16E1	2.55E4
				9.70E0	3.00E4
				1.07E0	7.79E4
				1.04E-1	4.63E5

Table A.3: LVE Spectra for PS Melts Considered in Chapter IV - Part II

Sample Name	Source	Fitting Method	No. of Modes (i)	τ_i [s]	g_i [Pa]
200k	[139]	Wagner [143]	8	2.65E1	8.05E1
				1.49E0	3.06E4
				5.48E-1	6.69E4
				7.11E-2	6.66E4
				7.13E-3	6.67E4
				5.09E-4	1.84E5
				2.92E-7	1.38E7
				2.08E-5	1.58E6
182k	[51]	Reptate	7	3.39E-1	6.96E4
				4.58E-2	7.61E4
				6.18E-3	5.93E4
				8.34E-4	7.67E4
				1.13E-4	2.13E5
				1.52E-5	3.4E5
				2.05E-6	6.38E6
145k	[138]	Reptate	7	9.47E4	2.56E2
				9.16E3	9.22E4
				8.85E2	7.66E4
				8.55E1	7.81E4
				8.26E0	2.79E5
				7.99E-1	5.47E5
				7.72E-2	1.37E7

Table A.4: LVE Spectra for PS Solutions Considered in Chapter IV

Sample Name	Source	Fitting Method	No. of Modes (i)	τ_i [s]	g_i [Pa]
7.35% 3.9M	[127]	Reptate	6	2.29E1	5.75E-2
				3.93E0	1.34E2
				6.74E-1	1.73E2
				1.16E-1	1.49E2
				1.98E-2	1.13E2
				3.40E-3	3.98E2
10% 3.9M	[127]	Reptate	5	1.16E1	3.46E2
				1.91E0	4.74E2
				3.14E-1	3.73E2
				5.16E-2	2.75E2
				8.47E-3	5.51E2

Appendix B

Dynamical Equations for Slip-link Simulations

B.1 Nondimensionalization of the Node Motion Equation

The Langevin equation for the position of each node or slip-link $\mathbf{R}_i$ is written as follows.

$$\zeta(\dot{\mathbf{R}}_i - \boldsymbol{\kappa} \cdot R_i) = \sum_{i=1}^{f} \mathbf{F}_i + \mathbf{F}_o + \mathbf{F}_r \tag{B.1}$$

Neglecting the contribution of $\mathbf{F}_o$, setting $\boldsymbol{\kappa} = 0$ and introducing the definition of $\mathbf{F}_i$ for a Gaussian subchain in section 2.2.1 to (B.1), the following equation is obtained.

$$\zeta\dot{\mathbf{R}}_i = \frac{3kT}{b^2} \sum_{i=1}^{f} \frac{\mathbf{r}_i}{n_i} + \mathbf{F}_r \tag{B.2}$$

Recall that the amplitude for the random force is given by the correlation function

$$\langle F_r(t) F_r(t') \rangle = 6kT\zeta\delta(t - t') \approx \frac{6kT\zeta}{(t - t')} \tag{B.3}$$

where the Dirac delta function $\delta(t - t')$ can approximated by $1/(t - t')$. The random force $\mathbf{F}_r$ is then given by

$$\mathbf{F}_r = \sqrt{\frac{6kT\zeta}{t-t'}}\,\mathbf{W} \tag{B.4}$$

where $\mathbf{W}$ is a unit random vector – i.e. vector of length unity pointing in a random direction obtained by randomly sampling points along a unit sphere.

Equation (B.2) can then be written in discretized form by writing the derivative $\dot{\mathbf{R}}_i = d\mathbf{R}_i/dt$ as $\Delta\mathbf{R}_i/\Delta t$ resulting in

$$\frac{\zeta\Delta\mathbf{R}_i}{\Delta t} = \frac{3kT}{b^2}\sum_{i=1}^{f}\frac{\mathbf{r}_i}{n_i} + \sqrt{\frac{6kT\zeta}{\Delta t}}\,\mathbf{W} \tag{B.5}$$

where the difference $t - t'$ was replaced by Δt in the amplitude of the random force.

Re-arranging terms, (B.5) becomes

$$\Delta\mathbf{R}_i = \frac{3kT}{\zeta b^2}\Delta t\sum_{i=1}^{f}\frac{\mathbf{r}_i}{n_i} + \sqrt{\frac{6kT\Delta t}{\zeta}}\,\mathbf{W} \tag{B.6}$$

Introducting the nondimensional variables $\tilde{\mathbf{r}} = \mathbf{r}/r_0$, $\tilde{n} = n/n_0$ and $\Delta\tilde{t} = \Delta t/\tau_0$, (B.6) can then be written as

$$r_0\Delta\tilde{\mathbf{R}}_i = \frac{3kT}{\zeta b^2}\frac{r_0}{n_0}\Delta t\sum_{i=1}^{f}\frac{\tilde{\mathbf{r}}_i}{\tilde{n}_i} + \sqrt{\frac{6kT\Delta\tilde{t}\tau_0}{\zeta}}\,\mathbf{W} \tag{B.7}$$

where $\tau_0 = n_0 b^2\zeta/6kT$.

Dividing both sides of (B.7) by r_0 and using the relationship $r_0^2 = n_0 b^2$, we obtain

$$\Delta\tilde{\mathbf{R}}_i = \frac{\Delta\tilde{t}}{2}\sum_{i=1}^{f}\frac{\tilde{\mathbf{r}}_i}{\tilde{n}_i} + \sqrt{\Delta\tilde{t}}\,\mathbf{W} \tag{B.8}$$

which is the non-dimensional discretized equation of motion for the node i assuming Gaussian elastic forces.

For non-Gaussian chains, as discussed in 2.2.1, the factor $f(r)$ for finite extensibility must be included. Since $f(r)$ is nondimensional, it can be introduced without difficulty to equation (B.8).

$$\Delta\tilde{\mathbf{R}}_i = \frac{\Delta\tilde{t}}{2}\sum_{i=1}^{f}f(\tilde{r}_i)\frac{\tilde{\mathbf{r}}_i}{\tilde{n}_i} + \sqrt{\Delta\tilde{t}}\,\mathbf{W} \tag{B.9}$$

B.2 Nondimensionalization of the Monomer Sliding Equation

The Langevin equation for the sliding or monomer exchange across two subchains in a slip-link is written as follows.

$$\zeta_m v = F_m + F_m^r \tag{B.10}$$

where v, F_m and F_m^r have been defined in section 2.2.1.

Introducing these definitions and recalling that $\zeta_m = \zeta/2$, we obtain

$$\zeta_m \left(\dot{n} \frac{r_0}{n_0} \right) = \frac{\zeta}{2} \left(\dot{n} \frac{1}{\rho_m} \right) = \frac{3kT}{b^2} \left(\frac{r_1}{n_1} - \frac{r_2}{n_2} \right) \pm \sqrt{\frac{kT\zeta}{t - t'}} \tag{B.11}$$

where the linear monomer density $\rho_m = n_0/r_0$ is introduced and the Dirac delta function $\delta(t - t')$ was again approximated by $1/(t - t')$.

Equation (B.11) can then be discretized by writing $\dot{n} = \Delta n/\Delta t$.

$$\frac{\zeta}{2} \left(\frac{\Delta n}{\Delta t} \frac{1}{\rho_m} \right) = \frac{3kT}{b^2} \left(\frac{r_1}{n_1} - \frac{r_2}{n_2} \right) \pm \sqrt{\frac{kT\zeta}{\Delta t}} \tag{B.12}$$

Re-arranging terms and introducing the non-dimensional variables defined in the previous section, one then obtains

$$\Delta \tilde{n} = \rho_m \left[\Delta \tilde{t} \left(\frac{\tilde{r}_1}{\tilde{n}_1} - \frac{\tilde{r}_2}{\tilde{n}_2} \right) \pm \sqrt{\frac{\Delta \tilde{t}}{6}} \right] \tag{B.13}$$

which is the non-dimensional discretized equation of motion for monomer sliding. Note that in the later versions of the PCN model [91, 97], ρ_m is taken determined by the monomer density $\tilde{n}/\tilde{r}$ of the subchain winning in the force balance and not the values at equilibrium.

B.3 Nondimensionalization of the μ-based Monomer Sliding Equation

The alternative sliding equation proposed in section 2.3.4 is based on the sliding equation proposed by Schieber [107] recalled here as follows

$$\Delta n = \frac{1}{kT\tau_K} \left(\mu_{i+1} - \mu_i \right) \Delta t \pm \sqrt{\frac{2\Delta t}{\tau_K}} \tag{B.14}$$

and the chemical potential μ_i is defined as

$$\mu_i = \frac{3}{2}kT\left(\frac{1}{n_i} - \frac{r_i^2}{n_i^2 b^2}\right) \tag{B.15}$$

based on the free energy reported by Schieber [106, 107].

Equation (B.14) is already discretized so the remaining task is to present it in non-dimensional form. The following non-dimensional variables can then be introduced $\tilde{n} = n/n_0$ and $\tilde{r} = r/r_0$ to rewrite (B.14) as

$$n_0\Delta\tilde{n} = \frac{3}{2n_0\tau_K}\left(\frac{1}{\tilde{n}_{i+1}} - \frac{1}{\tilde{n}_i} - \frac{\tilde{r}_{i+1}^2}{\tilde{n}_{i+1}^2 b^2} + \frac{\tilde{r}_i^2}{\tilde{n}_i^2 b^2}\right)\Delta t \pm \sqrt{\frac{2\Delta t}{\tau_K}} \tag{B.16}$$

where some simplification was made using $r_0^2 = n_0 b^2$.

Dividing both sides of (B.16) by n_0 would lead to a form where the obvious choice in non-dimensionalizing the time is to define $\Delta\tilde{t} = \Delta t/\tau_0$ with $\tau_0 = \tau_K n_0^2/2$.

The non-dimensional equation of motion for the sliding process is then as follows.

$$\Delta\tilde{n} = \frac{3}{4}\Delta\tilde{t}\left[\left(\frac{\tilde{r}_i^2}{\tilde{n}_i^2} - \frac{\tilde{r}_{i+1}^2}{\tilde{n}_{i+1}^2}\right) + \left(\frac{1}{\tilde{n}_{i+1}} - \frac{1}{\tilde{n}_i}\right)\right] \pm \sqrt{\Delta\tilde{t}} \tag{B.17}$$

Appendix C

Analytic Expressions for Parallel Superposition Flows

The following analytic expressions are the results of the linear expansion approach discussed in 3.2.2 and are used to generate the results for Chapter 3.

The superposition storage modulus G'_{sup} for each mode is given by the expression

$$G'_{\text{sup}}(\omega, \tau, \dot{\gamma}, \beta) = \frac{C'_1 + C'_2 + C'_3}{C'_4 + C'_5} \tag{C.1}$$

where the quantities C'_1, C'_2, C'_3, C'_4 and C'_5 are defined as

$$C'_1 = -3\tau^2(6\beta A_{xy}^2 - 3A_{yy} + 4\dot{\gamma}A_{xy}(1 + \beta(-1 + 6\beta A_{xy}^2))\tau \tag{C.2}$$

$$C'_2 = 2\dot{\gamma}^2(A_{yy} + \beta(12\beta^2 A_{xy}^4 + A_{yy}(-1 + 3A_{yy}) \tag{C.3}$$

$$C'_3 = A_{xy}^2(4 + \beta(-4 + 6A_{yy}))))\tau^2)\omega^2 + 9(-2\beta A_{xy}^2 + A_{yy})\tau^4\omega^4 \tag{C.4}$$

$$C'_4 = (3 + 2\dot{\gamma}\tau(9\beta A_{xy} + \dot{\gamma}(1 + \beta(-1 + 12\beta A_{xy}^2 + 3A_{yy}))\tau))^2 \tag{C.5}$$

$$C'_5 = 6\tau^2(3+2\dot{\gamma}\tau(9\beta A_{xy}+\dot{\gamma}(-1+\beta+15\beta^2 A_{xy}^2-3\beta A_{yy})\tau))\omega^2+9\tau^4\omega^4 \tag{C.6}$$

On the other hand, the superposition loss modulus G''_{sup} is given by the following expression

$$G''_{\text{sup}}(\omega, \tau, \dot{\gamma}, \beta) = \frac{C''_1}{C''_8 + C''_9} \tag{C.7}$$

$$C''_1 = \tau\omega(-288\beta^4\dot{\gamma}^3 A_{xy}^5\tau^3 + C''_2 + C''_3 + C''_4 + C''_6) \tag{C.8}$$

$$C''_2 = -72\beta^3\dot{\gamma}^2 A_{xy}^3\tau^2(5A_{xy} + \dot{\gamma}(-1 + A_{yy})\tau) \tag{C.9}$$

$$C''_3 = (3A_{yy} - 2\dot{\gamma}A_{xy}\tau)(3 + 2\dot{\gamma}^2\tau^2) + 3\tau^2(3A_{yy} + 2\dot{\gamma}A_{xy}\tau)\omega^2 \tag{C.10}$$

$$C''_4 = -4\beta^2\dot{\gamma}A_{xy}\tau(-3\dot{\gamma}A_{xy}(4 + 3A_{yy})\tau + \dot{\gamma}^2(1 - 3A_{yy})\tau^2 + C''_5) \tag{C.11}$$

$$C''_5 = 18A_{xy}^2(2 + \tau^2(\dot{\gamma}^2 + \omega^2)) \tag{C.12}$$

$$C''_6 = 2\beta(3\dot{\gamma}^2 A_{yy}(-1 + 3A_{yy})\tau^2 - 3A_{xy}^2(3 + \tau^2(8\dot{\gamma}^2 + 3\omega^2)) + C''_7) \tag{C.13}$$

$$C''_7 = \dot{\gamma}A_{xy}\tau(3 + 27A_{yy} + 4\dot{\gamma}^2\tau^2 - 6\dot{\gamma}^2 A_{yy}\tau^2 + 3(-1 + 9A_{yy})\tau^2\omega^2) \tag{C.14}$$

$$C''_8 = (3 + 2\dot{\gamma}\tau(9\beta A_{xy} + \dot{\gamma}(1 + \beta(-1 + 12\beta A_{xy}^2 + 3A_{yy}))\tau))^2 \tag{C.15}$$

$$C''_9 = 6\tau^2(3+2\dot{\gamma}\tau(9\beta A_{xy}+\dot{\gamma}(-1+\beta+15\beta^2 A_{xy}^2-3\beta A_{yy})\tau))\omega^2+9\tau^4\omega^4 \tag{C.16}$$

In both expressions, A_{xy} and A_{yy} are the steady values of the xy and yy components of $\mathbf{A}$ due to the background flow, which could be obtained by building the transient response up to the steady-state.

Bibliography

[1] M Doi and SF Edwards. *The Theory of Polymer Dynamics*. Oxford University Press, USA, 1986.

[2] SF Edwards. The statistical mechanics of polymerized material. *Proceedings of the Physical Society*, 92:9–16, 1967.

[3] PG de Gennes. Reptation of a polymer chain in the presence of fixed obstacles. *Journal of Chemical Physics*, 55:572–579, 1971.

[4] M Doi and SF Edwards. Dynamics of concentrated polymer systems, part 1 - brownian motion in the equilibrium state. *Journal of the Chemical Society, Faraday Transactions 2: Molecular and Chemical Physics*, 74:1789–1801, 1978.

[5] M Doi and SF Edwards. Dynamics of concentrated polymer systems, part 2 - molecular motion under flow. *Journal of the Chemical Society, Faraday Transactions 2: Molecular and Chemical Physics*, 74:1802–1817, 1978.

[6] M Doi and SF Edwards. Dynamics of concentrated polymer systems, part 3 - the constitutive equation. *Journal of the Chemical Society, Faraday Transactions 2: Molecular and Chemical Physics*, 74:1818–1832, 1978.

[7] M Doi and SF. Edwards. Dynamics of concentrated polymer systems, part 4 - rheological properties. *Journal of the Chemical Society, Faraday Transactions 2: Molecular and Chemical Physics*, 38-54:DE4, 1979.

[8] G Marrucci. Polymers go with the flow. *Science*, 301:1681–1682, 2003.

[9] TCB McLeish. Tube theory of entangled polymer dynamics. *Advances in Physics*, 51:1379–1527, 2002.

[10] N Hadjichristidis, H Iatrou, S Pispas, and Pitsikalis M. Anionic polymerization: high vacuum techniques. *Journal of Polymer Science, Part A: Polymer Chemistry*, 38:3211–3234, 2000.

[11] GH McKinley and T Sridhar. Filament-stretching rheometry of complex fluids. *Annual Review of Fluid Mechanics*, 34:375–415, 2002.

[12] ML Sentmanat. Miniature universal testing platform: from extensional melt rheology to solid-state deformation behavior. *Rheologica Acta*, 43:657–669, 2004.

[13] H Watanabe. Viscoelasticity and dynamics of entangled polymers. *Progress in Polymer Science*, 24:1253–1403, 1999.

[14] H Watanabe, Y Matsumiya, and T Inoue. Dielectric and viscoelastic study of entanglement dynamics: A review of recent findings. *Macromolecular Symposia*, 228:51–70, 2005.

[15] J Bent, LR Hutchings, RW Richards, T Gough, R Spares, PD Coates, I Grillo, OG Harlen, DJ Read, RS Graham, AE Likhtman, DJ Groves, TM Nicholson, and TCB McLeish. Neutron-mapping polymer flow: scattering, flow visualization and molecular theory. *Science*, 301:1691–1695, 2003.

[16] K Kremer and GS Grest. Dynamics of entangled linear polymer melts: A molecular-dynamics simulation. *Journal of Chemical Physics*, 92:5057–5086, 1990.

[17] R Everaers, SK Sukumaran, G. Grest, C Svaneborg, A Sivasubramanian, and K Kremer. Rheology and microscopic topology of entangled polymeric liquids. *Science*, 303:823–826, 2004.

[18] DJ Read, K Jagannathan, and AE Likhtman. Entangled polymers: constraint release, mean paths and tube bending energy. *Macromolecules*, 41:6843–6853, 2008.

[19] RG Larson. Looking inside the entanglement "tube" using molecular dynamics simulations. *Journal of Polymer Science, Part B: Polymer Physics*, 45:3240–3248, 2007.

[20] J Padding and W Briels. Uncrossability constraints in mesoscopic polymer melt simulations: Non-rouse behavior of c120h242. *Journal of Chemical Physics*, 115:2846–2859, 2001.

[21] CC Hua and JD Schieber. Segment connectivity, chain-length breathing, segmental stretch and constraint release in reptation models. i. theory and single-step strain predictions. *Journal of Chemical Physics*, 109:10018–10027, 1998.

[22] Y Masubuchi, JI Takimoto, K Koyama, G Ianniruberto, G Marrucci, and F Greco. Brownian simulations of a network of reptating primitive chains. *Journal of Chemical Physics*, 115:4387–4394, 2001.

[23] S Shanbhag, RG Larson, JI Takimoto, and M Doi. Deviations from dynamic dilution in the terminal relaxation of star polymers. *Physical Review Letters*, 87:195502, 2001.

[24] M Doi and JI Takimoto. Molecular modeling of entanglement. *Philosophical Transactions of the Royal Society of London A*, 361:641–652, 2003.

[25] JD Schieber, J Neergard, and S Gupta. A full-chain, temporary network model with slip-links, chain-length fluctuations, chain connectivity and chain stretching. *Journal of Rheology*, 47:213, 2003.

[26] S Shanbhag and RG Larson. A slip-link model of branch point motion in entangled polymers. *Macromolecules*, 37:8160–8166, 2004.

[27] AE Likhtman. Single-chain slip-link model of entangled polymers: Simultaneous description of neutron spin-echo, rheology and diffusion. *Macromolecules*, 38:6128–6139, 2005.

[28] C Tzoumanekas and DN Theodorou. From atomistic simulations to slip-link models of entangled polymer melts: Hierarchical strategies for the prediction of rheological properties. *Current Opinion in Solid State and Materials Science*, 10:61–72, 2006.

[29] DJ Read, D Auhl, C Das, J den Doelder, M Kapnistos, I Vittorias, and TCB McLeish. Linking models of polymerization and dynamics to predict branched polymer structure and flow. *Science*, 333:1871–1874, 2011.

[30] Y Masubuchi, T Uneyama, and K Saito. A multiscale simulation of polymer processing using parameter-based bridging in melt rheology. *Journal of Applied Polymer Science*, 125:2740–2747, 2012.

[31] AE Likhtman. Whither tube theory: From believing to measuring. *Journal of Non-Newtonian Fluid Mechanics*, 157:158–161, 2009.

[32] MV Acharya, PK Bhattacharjee, DA Nguyen, and T Sridhar. Are entangled polymer solutions different from melts? In *Proceedings of the XVth International Congress on Rheology*, 2008.

[33] Q Huang, O Mednova, HK Rasmussen, AL Skov, K Almdal, and O Hassager. Are entangled polymer melts different from solutions? In *Proceedings of the XVIth International Congress on Rheology*, 2012.

[34] HK Rasmussen, JK Nielsen, A Bach, and O Hassager. Viscosity overshoot in the start-up of uniaxial elongation of low density polyethylene melts. *Journal of Rheology*, 49:369–381, 2005.

[35] P Tapadia and SQ Wang. Direct visualization of continuous simple shear in non-newtonian polymeric fluids. *Physical Review Letters*, 96:016001, 2006.

[36] SQ Wang, S Ravindranath, P. Boukany, M Olechnowicz, R Quirk, A Halasa, and J Mays. Nonquiescent relaxation in entangled polymeric liquids after step shear. *Physical Review Letters*, 97:187801, 2006.

[37] PE Boukany and SQ Wang. A correlation between velocity profile and molecular weight distribution in sheared entangled polymer solutions. *Journal of Rheology*, 51:217–233, 2007.

[38] SQ Wang, S Ravindranath, Y Wang, and PE Boukany. New theoretical considerations in polymer rheology: Elastic breakdown of chain entanglement network. *Journal of Chemical Physics*, 127:064903, 2007.

[39] RG Larson. *Structure and Rheology of Complex Fluids*. Oxford University Press, USA, 1998.

[40] RG Larson and JM Dealy. *Structure and Rheology of Molten Polymers*. Hanser Publications, 2006.

[41] J Oberdisse, G Ianniruberto, F Greco, and G Marrucci. Primitive-chain brownian simulations of entangled rubbers. *Europhysics Letters*, 58:530–536, 2002.

[42] J Oberdisse, G Ianniruberto, F Greco, and G Marrucci. Mechanical properties of end-crosslinked entangled polymer networks using sliplink brownian dynamics simulations. *Rheologica Acta*, 46:95–109, 2006.

[43] PE Boukany and SQ Wang. Nature of steady flow in entangled fluids revealed by superimposed small amplitude oscillatory shear. *Journal of Rheology*, 53:1425–1435, 2009.

[44] X Li and SQ Wang. Studying steady shear flow characteristics of entangled polymer solutions with parallel mechanical superposition. *Macromolecules*, 43:5904–5908, 2010.

[45] G Marrucci. Dynamics of entanglements: A nonlinear model consistent with the cox-merz rule. *Journal of Non-Newtonian Fluid Mechanics*, 62:279–289, 1996.

[46] G Ianniruberto and G Marrucci. On compatibility of the cox-merz rule with the model of doi and edwards. *Journal of Non-Newtonian Fluid Mechanics*, 65:241–246, 1996.

[47] G Ianniruberto, A Brasiello, and G Marrucci. Friction coefficient does not stay constant in nonlinear viscoelasticity. In *Proceedings of the 7th Annual European Rheology Conference*, 2011.

[48] M Rubinstein. Dynamics of ring polymers in the presence of fixed obstacles. *Physical Review Letters*, 57:3023–3026, 1986.

[49] M Kapnistos, M Lang, D Vlassopoulos, W Pyckhout-Hintzen, D Richter, D Cho, T Chang, and M Rubinstein. Unexpected power-law stress relaxation of entangled ring polymers. *Nature Materials*, 7:997–1002, 2008.

[50] RG Larson. *Constitutive Equations for Polymer Melts and Solutions*. Butterworth-Heinemann, 1988.

[51] F Snijkers and D Vlassopoulos. Cone-partitioned-plate geometry for the ares rheometer with temperature control. *Journal of Rheology*, 55:1167–1186, 2011.

[52] PE Rouse. A theory of the linear viscoelastic properties of dilute solutions of coiling polymers. *Journal of Chemical Physics*, 21:1272, 1953.

[53] M Rubinstein and RH Colby. *Polymer Physics*. Oxford University Press, USA, 2003.

[54] GC Berry and TG Fox. The viscosity of polymers and their concentrated solutions. *Advances in Polymer Science*, 5:261–357, 1968.

[55] RH Colby, LJ Fetters, and W Graessley. Melt viscosity-molecular weight relationship for linear polymers. *Macromolecules*, 20:2226–2237, 1987.

[56] RG Larson, T Sridhar, LG Leal, GH McKinley, AE Likhtman, and TCB McLeish. Definitions of entanglement spacing and time constants in the tube model. *Journal of Rheology*, 47:809–818, 2003.

[57] K Osaki, K Nishizawa, and M Kurata. Material time constant characterizing the nonlinear viscoelasticity of entangled polymeric systems. *Macromolecules*, 15:1068, 1982.

[58] K Osaki. On the damping function of shear relaxation modulus for entangled polymers. *Rheologica Acta*, 32:429–437, 1993.

[59] AE Likhtman and TCB McLeish. Quantitative theory for linear dynamics of linear entangled polymers. *Macromolecules*, 35:6332–6343, 2002.

[60] ST Milner and TCB McLeish. Reptation and contour-length fluctuations in melts of linear polymers. *Physical Review Letters*, 81:725–728, 1998.

[61] J des Cloizeaux. Double reptation vs. simple reptation in polymer melts. *Europhysics Letters*, 5:437–442, 1988.

[62] W Graessley. Entangled linear, branched and network polymer systems - molecular theories. *Advances in Polymer Science*, 47:69–117, 1982.

[63] G Marrucci. Relaxation by reptation and tube enlargement: a model for polydisperse polymers. *Journal of Polymer Science: Polymer Physics Edition*, 23:159–177, 1985.

[64] JL Viovy, M Rubinstein, and RH Colby. Constraint release in polymer melts: tube reorganization versus tube dilation. *Macromolecules*, 24:3587–3596, 1991.

[65] M Doi. Explanation for the 3.4-power law for viscosity of polymeric liquids on the basis of the tube model. *Journal of Polymer Science: Polymer Physics Edition*, 21:667–684, 1983.

[66] G Marrucci and N Grizzuti. Fast flows of concentrated polymers: predictions of the tube model on chain stretching. *Gazzetta Chimica Italiana*, 118:179–185, 1988.

[67] D Pearson, E Herbolzheimer, N Grizzuti, and G Marrucci. Transient behavior of entangled polymers at high shear rates. *Journal of Polymer Science, Part B: Polymer Physics*, 29:1589–1597, 1991.

[68] D Pearson, AD Kiss, and LJ Fetters. Flow-induced birefringence of concentrated polyisoprene solutions. *Journal of Rheology*, 33:517–535, 1989.

[69] G Ianniruberto and G Marrucci. Convective orientational renewal in entangled polymers. *Journal of Non-Newtonian Fluid Mechanics*, 95:363–374, 2000.

[70] W Graessley. The entanglement concept in polymer rheology. *Advances in Polymer Science*, 16:1–179, 1974.

[71] DW Mead, RG Larson, and M Doi. A molecular theory for fast flows of entangled polymers. *Macromolecules*, 31:7895–7914, 1998.

[72] G Ianniruberto and G Marrucci. A simple constitutive equation for entangled polymers with chain stretch. *Journal of Rheology*, 45:1305–1318, 2001.

[73] RS Graham, AE Likhtman, TCB McLeish, and ST Milner. Microscopic theory of linear, entangled polymer chains under rapid deformation including chain stretch and convective constraint release. *Journal of Rheology*, 47:1171–1200, 2003.

[74] E van Ruymbeke, R Keunings, and C Bailly. Prediction of linear viscoelastic properties for polydisperse mixtures of entangled star and linear polymers: modified tube-based model and comparison with experimental results. *Journal of Non-Newtonian Fluid Mechanics*, 128:7–22, 2005.

[75] ST Milner and TCB McLeish. Parameter-free theory for stress relaxation in star polymer melts. *Macromolecules*, 30:2159–2166, 1997.

[76] TCB McLeish, J Allgaier, DK Bick, G Bishko, P Biswas, R Blackwell, B Blottiere, N Clarke, B Gibbs, DJ Groves, A Hakiki, RK Heenan, JM Johnson, R Kant, DJ Read, and RN Young. Dynamics of entangled h-polymers: theory, rheology and neutron-scattering. *Macromolecules*, 32:6734–6758, 1999.

[77] C Das, NJ Inkson, DJ Read, MA Kelmanson, and TCB McLeish. Computational linear rheology of general branch-on-branch polymers. *Journal of Rheology*, 50:207–234, 2006.

[78] RC Ball and TCB McLeish. Dynamic dilution and the viscosity of star polymer melts. *Macromolecules*, 22:1911–1913, 1989.

[79] G Ianniruberto and G Marrucci. A multi-mode ccr model for entangled polymers with chain stretch. *Journal of Non-Newtonian Fluid Mechanics*, 102:383–395, 2002.

[80] G Marrucci and G Ianniruberto. Flow-induced orientation and stretching of entangled polymers. *Philosophical Transactions of the Royal Society of London A*, 361:677–688, 2003.

[81] AE Likhtman and RS Graham. Simple constitutive equation for linear polymer melts derived from molecular theory: Rolie-poly equation. *Journal of Non-Newtonian Fluid Mechanics*, 114:1–12, 2003.

[82] TCB McLeish and RG Larson. Molecular constitutive equations for a class of branched polymers: The pom-pom polymer. *Journal of Rheology*, 42:81–110, 1998.

[83] JT Padding and WJ Briels. Systematic coarse-graining of the dynamics of entangled polymer melts: the road from chemistry to rheology. *Journal of Physics: Condensed Matter*, 23:233101, 2011.

[84] VA Harmandaris, VG Mavrantzas, DN Theodorou, M Kroger, J Ramirez, HC Ottinger, and D Vlassopoulos. Crossover from the rouse to the entangled polymer melt regime: signals from long, detailed atomistic molecular dynamics simulations, supported by rheological experiments. *Macromolecules*, 36:1376–1387, 2003.

[85] G Ianniruberto, A Brasiello, and G Marrucci. Simulations of fast shear flows of ps oligomers confirm monomeric friction reduction in fast elongational flows of monodisperse ps melts as indicated by rheooptical data. *Macromolecules*, 45:8058–8066, 2012.

[86] AE Likhtman, SK Sukumaran, and J Ramirez. Linear viscoelasticity from molecular dynamics simulation of entangled polymers. *Macromolecules*, 40:6748–6757, 2007.

[87] SD Anogiannakis, C Tzoumanekas, and DN Theodorou. Microscopic description of entanglements in polyethylene networks and melts: Strong, weak, pairwise and collective attributes. *Macromolecules*, 45:9475–9492, 2012.

[88] W Bisbee, J Qin, and ST Milner. Finding the tube with isoconfigurational averaging. *Macromolecules*, 44:8972–8980, 2011.

[89] Y Masubuchi, G Ianniruberto, F Greco, and G Marrucci. Primitive chain network simulations for branched polymers. *Rheologica Acta*, 46:297–303, 2006.

[90] Y Masubuchi, G Ianniruberto, F Greco, and G Marrucci. Quantitative comparison of primitive chain network simulations with literature data of linear viscoelasticity for polymer melts. *Journal of Non-Newtonian Fluid Mechanics*, 149:87–92, 2008.

[91] T Yaoita, T Isaki, Y Masubuchi, H Watanabe, G Ianniruberto, F Greco, and G Marrucci. Statics, linear and nonlinear dynamics of entangled polystyrene melts simulated through the primitive chain network model. *Journal of Chemical Physics*, 128:154901, 2008.

[92] Y Masubuchi, G Ianniruberto, F Greco, and G Marrucci. Primitive chain network model for block copolymers. *Journal of Non-Crystalline Solids*, 352:5001–5007, 2006.

[93] JD Schieber and K Horio. Fluctuation in entanglement positions via elastic slip-links. *Journal of Chemical Physics*, 132:074905, 2010.

[94] T Uneyama and Y Masubuchi. Multi-chain slip-spring model for entangled polymer dynamics. *Journal of Chemical Physics*, 137:154902, 2012.

[95] VC Chappa, DC Morse, A Zippelius, and M Muller. Translationally invariant slip-spring model for entangled polymer dynamics. *Physical Review Letters*, 109:148302, 2012.

[96] Y Masubuchi, G Ianniruberto, F Greco, and G Marrucci. Entanglement molecular weight and frequency response of sliplink networks. *Journal of Chemical Physics*, 119:6925–6930, 2003.

[97] Y Masubuchi, T Uneyama, H Watanabe, G Ianniruberto, F Greco, and G Marrucci. Structure of entangled polymer network from primitive

chain network simulations. *Journal of Chemical Physics*, 132:134902, 2010.

[98] T Yaoita, T Isaki, Y Masubuchi, H Watanabe, G Ianniruberto, and G Marrucci. Primitive chain network simulation of elongational flows of entangled linear chains: role of finite chain extensibility. *Macromolecules*, 44:9675–9682, 2011.

[99] T Yaoita, T Isaki, Y Masubuchi, H Watanabe, G Ianniruberto, and G Marrucci. Primitive chain network simulation of elongational flows of entangled linear chains: stretch/orientation-induced reduction of monomeric friction. *Macromolecules*, 45:2773–2782, 2012.

[100] RC Ball, M Doi, SF Edwards, and M Warner. Elasticity of entangled networks. *Polymer*, 22:1010–1018, 1981.

[101] SF Edwards and TA Vilgis. The effect of entanglements in rubber elasticity. *Polymer*, 27:483–492, 1986.

[102] K Urayama, T Kawamura, and S Kohjiya. Multiaxial deformations of end-linked poly(dimethylsiloxane) networks. 2. experimental tests of molecular entanglement models of rubber elasticity. *Macromolecules*, 34:8261–8269, 2001.

[103] GS Grest, M Putz, R Everaers, and K Kremer. Stress-strain relation of entangled polymer networks. *Journal of Non-Crystalline Solids*, 274:139–146, 2000.

[104] Y Masubuchi. Primitive chain network simulations for relaxation behaviors of polymeric materials. *Nippon Gomu Kyokaishi (Journal of the Society of Rubber Science and Technology, Japan)*, 82:459–463, 2009.

[105] M Rubinstein and S Panyukov. Non-affine deformation and elasticity of polymer networks. *Macromolecules*, 30:8036–8044, 1997.

[106] JD Schieber. Fluctuations in entanglements of polymeric liquids. *Journal of Chemical Physics*, 118:5162–5166, 2003.

[107] JD Schieber. On nonaffine motion in entangled polymeric liquids. pre-print, available online http://www.chee.iit.edu/ schieber/Nonaffine.pdf, 2005.

[108] A Cohen. A pad approximant to the inverse langevin function. *Rheologica Acta*, 30:270–273, 1991.

[109] G Marrucci, F Greco, and G Ianniruberto. Possible role of force balance on entanglements. *Macromolecular Symposia*, 158:57–64, 2000.

[110] R Auhl, R Everaers, GS Grest, K Kremer, and SJ Plimpton. Equilibration of long chain polymer melts in computer simulations. *Journal of Chemical Physics*, 119:12718–12728, 2003.

[111] HH Winter and F Chambon. Analysis of linear viscoelasticity of a crosslinking polymer at the gel point. *Journal of Rheology*, 30:367–382, 1986.

[112] MP Allen and Tildesley DJ. *Computer Simulations of Liquids*. Oxford University Press, USA, 1987.

[113] JD Ferry. *Viscoelastic Properties of Polymers*. John Wiley & Sons, 1980.

[114] LGD Hawke and DJ Read. Modification of the pom-pom model for extensional viscosity overshoots. In *Proceedings of the XVIth International Congress on Rheology*, 2012.

[115] C Tzoumanekas and DN Theodorou. Topological analysis of linear polymer melts: A statistical approach. *Macromolecules*, 39:4592–4604, 2006.

[116] M Rubinstein and S Panyukov. Elasticity of polymer networks. *Macromolecules*, 35:6670–6686, 2002.

[117] F Greco. Entangled polymeric liquids: Nonstandard statistical thermodynamics of a subchain between entanglement points and a new calculation of the strain measure tensor. *Macromolecules*, 37:10079–10088, 2004.

[118] MK Jensen, R Khaliullin, and JD Schieber. Self-consistent modeling of entangled network strands and linear dangling structures in a single-strand mean-field slip-link model. *Rheologica Acta*, 51:21–35, 2012.

[119] AI Isayev and CM Wong. Parallel superposition of small- and large-amplitude oscillations upon stead shear flow of polymer liquids. *Journal of Polymer Science, Part B: Polymer Physics*, 26:2303–2327, 1988.

[120] J Vermant, L Walker, P Moldenaers, and J Mewis. Orthogonal versus parallel superposition measurements. *Journal of Non-Newtonian Fluid Mechanics*, 79:173–189, 1998.

[121] E Somma, O Valentino, G Titomanlio, and G Ianniruberto. Parallel superposition in entangled polydisperse polymer melts: Experiments and theory. *Journal of Rheology*, 51:987–1005, 2007.

[122] DW Mead. Development of the binary interaction theory for entangled polydisperse linear polymers. *Rheologica Acta*, 46:369–395, 2007.

[123] T Uneyama, K Horio, and H Watanabe. Anisotropic mobility model for polymers under shear and its linear response functions. *Physical Review E*, 83:061802, 2011.

[124] DW Mead. Small amplitude oscillatory shear flow superposed on parallel or perpendicular (orthogonal) steady shear of polydisperse linear polymers: The mld model. *Journal of Non-Newtonian Fluid Mechanics*, 2013. [in press].

[125] JM Adams and PD Olmsted. Nonmonotonic models are not necessary to obtain shear banding phenomena in entangled polymer solutions. *Physical Review Letters*, 102:67801, 2009.

[126] OS Agimelen and PD Olmsted. Apparent fracture in polymeric fluids under step shear. pre-print, available online http://arxiv.org/abs/1204.4169, 2012.

[127] PK Bhattacharjee, JP Oberhauser, G. McKinley, LG Leal, and T Sridhar. Extensional rheometry of entangled polymer solutions. *Macromolecules*, 35:10131–10148, 2002.

[128] PK Bhattacharjee, DA Nguyen, G. McKinley, and T Sridhar. Extensional stress growth and stress relaxation in entangled polymer solutions. *Journal of Rheology*, 47:269–290, 2003.

[129] A Bach, K Almdal, HK Rasmussen, and O Hassager. Elongational viscosity of narrow molar mass distribution polystyrene. *Macromolecules*, 36:5174–5179, 2003.

[130] JK Nielsen, O Hassager, HK Rasmussen, and GH McKinley. Elongational viscosity of monodisperse and bidisperse polystyrene melts. *Journal of Rheology*, 50:453–476, 2006.

[131] C Luap, C Muller, T Schweizer, and DC Venerus. Simultaneous stress and birefringence measurements during uniaxial elongation of polystyrene melts with narrow molecular weight distribution. *Rheologica Acta*, 45:83–91, 2005.

[132] G Marrucci and G Ianniruberto. Interchain pressure effect in extensional flows of entangled polymer melts. *Macromolecules*, 37:3934–3942, 2004.

[133] MH Wagner, S Kheirandish, and O Hassager. Quantitative prediction of transient and steady-state elongational viscosity of nearly monodisperse polystyrene melts. *Journal of Rheology*, 49:1317–1327, 2005.

[134] MH Wagner, VH Rolon-Garrido, JK Nielsen, HK Rasmussen, and O Hassager. A constitutive analysis of transient and steady-state elongational viscosities of bidisperse polystyrene blends. *Journal of Rheology*, 52:67–86, 2008.

[135] E van Ruymbeke, J. Nielsen, and O Hassager. Linear and nonlinear viscoelastic properties of bidisperse linear polymers: Mixing law and tube pressure effect. *Journal of Rheology*, 54:1155–1172, 2010.

[136] H Giesekus. Constitutive equations for polymer fluids based on the concept of configuration-dependent molecular mobility: a generalized mean-configuration model. *Journal of Non-Newtonian Fluid Mechanics*, 17:349–372, 1985.

[137] JM Wiest. A differential constitutive equation for polymer melts. *Rheologica Acta*, 28:4–12, 1989.

[138] JK Nielsen, HK Rasmussen, and O Hassager. Stress relaxation of narrow molar mass distribution polystyrene following uniaxial extension. *Journal of Rheology*, 52:885–899, 2008.

[139] T Schweizer, J van Meerveld, and HC Ottinger. Nonlinear shear rheology of polystyrene melt with narrow molecular weight distribution-experiment and theory. *Journal of Rheology*, 48:1345–1363, 2004.

[140] G Marrucci and B de Cindio. The stress relaxation of molten pmma at large deformations and its theoretical interpretation. *Rheologica Acta*, 19:68–75, 1980.

[141] G Marrucci, F Greco, and G Ianniruberto. Integral and differential constitutive equations for entangled polymers with simple versions of ccr and force balance on entanglements. *Rheologica Acta*, 40:98–103, 2001.

[142] G Ianniruberto and G Marrucci. Entangled melts of branched ps behave like linear ps in the steady state of fast elongational flows. *Macromolecules*, 46:267–275, 2013.

[143] MH Wagner and VH Rolon-Garrido. The interchain pressure effect in shear rheology. *Rheologica Acta*, 49:459–471, 2010.

[144] S Dhole, A Leygue, C Bailly, and R Keunings. A single-segment differential tube model with interchain pressure effect. *Journal of Non-Newtonian Fluid Mechanics*, 161:10–18, 2009.

[145] K Osaki, T Inoue, Y Uematsu, and Y Yamashita. Evaluation methods of the longest rouse relaxation time of an entangled polymer in a semidilute solution. *Journal of Polymer Science, Part B: Polymer Physics*, 39:1704–1712, 2001.

[146] X Ye, RG Larson, C Pattamaprom, and T Sridhar. Extensional properties of monodisperse and bidisperse polystyrene solutions. *Journal of Rheology*, 47:443–468, 2003.

[147] A Kushwaha and ESG Shaqfeh. Slip-link simulations of entangled polymers in planar extensional flow: disentanglement modified extensional thinning. *Journal of Rheology*, 55:463–483, 2011.

[148] J Park, DW Mead, and MM Denn. Stochastic simulation of entangled polymeric liquids in fast flows: microstructure modification. *Journal of Rheology*, 56:1057–1081, 2012.

[149] DJ Read, K Jagannathan, SK Sukumaran, and D Auhl. A full-chain constitutive model for bidisperse blends of linear polymers. *Journal of Rheology*, 56:823–873, 2012.

[150] JK Nielsen, HK Rasmussen, M Denberg, K Almdal, and O Hassager. Nonlinear branch-point dynamics of multiarm polystyrene. *Macromolecules*, 39:8844–8853, 2006.